Electronic and Structural Properties of Metal Chalcogenides Quantum Dots. A Theoretical Study Based on First-Principles Calculations

Roger Nadler

Departamento de Química Física
Universidad de Sevilla

September 5, 2013

Contents

1

Introduction

The history of the discovery of climate change reveals interesting twists and turns. Initial contributions were made from scientists well known to chemists and physicists, even though their work is ultimately only indirectly related to anthropogenic global warming. Today it is one of the great challenges we are facing, and most agree that renewable energies and energy efficiency are the key to our future and that of forthcoming generations. Be it wind, sun, waves, biomass or the earth's heat, all of them need to be exploited in order to reduce the greenhouse gas output concentration in the atmosphere. Photovoltaic power has the potential to be applied in a wide range of areas, from small cells built into clothes up to large-scale light harvesting PV power plants.

1.1 A short overview of climate change

The history of the discovery of climate change and its consequences started about 150 years ago. Back then, scientists were not concerned about climate change as we experience it today. The discussion was about why ice ages come and go and about how it is possible that tons of ice build up and melt again. The first scientist to evidence the relation between greenhouse gases and the earth temperature was John Tyndall in the late 19th century [1–3]. He explained that 10'000 years ago Europe was covered by a thick layer of ice, which was heavily debated back then. Tyndall identified H_2O and CO_2 as important and effective greenhouse gases [2].

After Tyndall, several scientists tried to calculate the temperature change induced by a certain amount of CO_2 in order to explain the emergence and disappearing of ice ages. Svante Arrhenius highlighted the correlation between the CO_2 concentration and the amount of water vapor in the air [4]. If the atmosphere contains more CO_2, the hotter the atmosphere becomes and, consequently, the more H_2O will evaporate into the atmosphere where it acts as greenhouse gas. Arrhenius' hypothesis was heavily criticized, most notably because he modeled a too simple climate system.

Knut Ångström ordered an assistant to measure the passage of infrared radiation through a tube filled with CO_2. They found that the adsorption of the radiation changed by only 0.4% when the tube was saturated with CO_2 [5]. From Ångström's point of view, it was impossible that such a small change in adsorption should have the impact on the climate as Arrhenius proposed it. Today we know that Arrhenius was right.

In the following, the discussion about CO_2 and its influence on climate change came to a rest until the 1950s, when Guy Stewart Callendar picked up the old ideas of Tyndall and Arrhenius. However, he was also faced with heavy criticism of his ideas, first, because he oversimplified the physical processes like the influence of water vapor and clouds. Secondly, knowledge about radiation processes in the atmosphere was little and hardly anyone could prove or falsify consistently the suggestions made by Arrhenius and Callendar.

For a long time critics doubted that CO_2 emitted locally could have an effect on the global climate. This changed when during nuclear weapon tests in the 1950s, after which the radioactive isotope carbon-14, which evolved in the

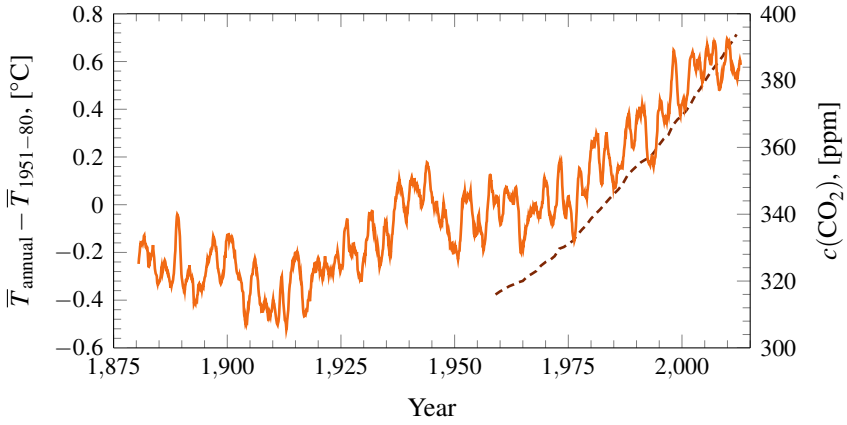

FIG. 1.1 The the annual averages of the CO_2 concentration between 1959 and 2012 are illustrated by the dashed line, collected at the Mauna Loa Observatory, Hawaii. The so called Keeling curve clearly shows a steady increase of the CO_2 concentration in the atmosphere since the beginning of the measurements in 1951. The orange line represents the annual global mean surface temperature vs. the mean surface temperature of the years 1951 until 1980. It strongly correlates with the increasing $c(CO_2)$Ḋata has been obtained from Reference [6].

blasts, was found to be distributed all over the world after a few years. This isotope is also constantly produced in the upper layers of the atmosphere by cosmic rays. Contrarily, the carbon contained in coal and fossil fuels is so old that all the carbon-14 already decayed. This argument allowed the chemist Hans Süss in 1955 to determine the concentration of fossil carbon in trees grown over the last decades. He found that the concentration is higher the newer the trees are. For the first time a consistent argumentation to explain the increase in the concentration of fossil carbon in the atmosphere was reported.

Eventually, Charles David Keeling developed sufficiently accurate instrumentation to measure the CO_2 concentration in the atmosphere. To his own surprise, he found that already within a few years after starting the measurements in 1957 the carbon dioxide concentration was rising (Fig. 1.1). Atmospheric scientists became alerted, also due to the increasing global mean surface temperatures. In Fig. 1.1 this increase is easily observed. From this moment on, the discussion about the anthropogenic, or human-induced, global warming gained weight. In addition, although still debated, the measurements of the CO_2 con-

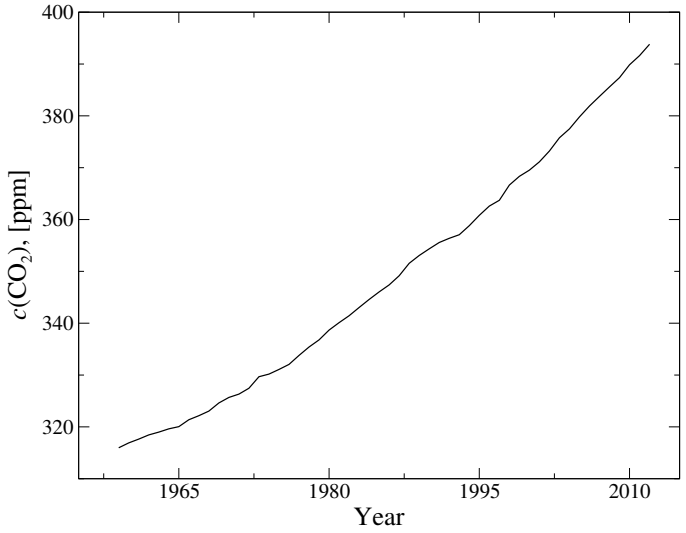

FIG. 1.2 Illustrated are the annual averages of the CO_2 concentration between 1959 and 2012, collected at the Mauna Loa Observatory, Hawaii. In this so called Keeling curve a clear increase of the concentration is observed.

centration and the global, averaged temperatures clearly support the thesis of an anthropogenic global warming.

1.2 Renewable energies

The ecological impact due to ever-increasing energy consumption is enormous if it is based upon fossil energy sources. The polar ice and glaciers are melting, with the effect that low-lying coasts and islands might sink below sea level. We observe already that the number of extreme weather phenomena increases. Long periods of drought and heavy rains and floods destroy infrastructure and carry away fertile soils. Species like ice bears and the coral reefs will disappear because the ecosystem they depend on will be destroyed.

Yet, the human history is characterized by the need for energy in one or another form, and it will continue to be for the next generations, too. Industrialized nations consume several 1000s of watts per capita. For instance, the United States of America consume 9538.8 W per capita, Switzerland 4458.5 W, and Spain 3691.5 W [7]. On the other side of the spectrum are developing nations

like Bangladesh that have an averaged energy consumption of about 278 W per capita. If these developing nations had similar energy needs than the industrialized nations today, the present energy portfolio, consisting mainly of highly unsustainable fossil and nuclear energy sources, will not be sufficient to fulfill all the energy needs in the long term. Therefore, it needs to be diversified in order to sustain future societies with energy.

One possible measure to reduce global warming is to reduce energy consumption. However, as obvious it sounds, as difficult it is to implement. A related example is that of paper usage. When in the 1980s personal computers (PC) became popular, one argument to promote them, amongst many, was that PCs would help to reduce paper usage. Today we know that the contrary is true, we print more than ever before.

Therefore, to complement the today's energy portfolio in a first step, followed by complete replacement, renewable energies are the only alternative. On the website of the International Energy Agency (IEA) it says:

> Renewable energy is energy that is derived from natural processes (e.g. sunlight and wind) that are replenished at a higher rate than they are consumed. Solar, wind, geothermal, hydro, and biomass are common sources of renewable energy.

In 2011, hydropower produced 13.7 % of the global electricity production (1357.7 TWh). In conformance with the BLUE scenario of the IEA, the production of around 6'000 TWh in 2050 is potentially feasible [8]. The drawback is that large areas of otherwise fertile or worth to be protected land will get lost and people have to leave their homes. Not surprisingly, dam projects are often confronted with massive opposition from the local population and environmental activists.

The remaining renewable energies wind, solar, geothermal, and others produced 421 TWh in 2011, a small share compared to hydropower. Although the total capacity is small, the growth rates are not. From January to November 2012, an increase of produced electricity of 20.9 % was determined compared to the same period in 2011. Within this group of renewable energies, wind energy produces most electricity: 345 TWh in 2010, where the globally installed capacity was equivalent to 238 GW at the end of 2011. Until 2016, market forecasts

predict a total installed capacity of around 493 GW. Advantages are mostly that it is a mature and efficient technology with quite a high return-on-investment and little maintenance requirements.

1.2.1 Photovoltaic solar cells

Recently, photovoltaic (PV) solar panels have dropped a lot in prices, therefore making it more and more competitive comparing to fossil and nuclear energy. Related to solar PV power there exist several projects that are being planned or already are under construction, which will increase the installed capacity of roughly 65 GW in 2011 to an estimated 230 GW in 2017. The IEA's roadmap for solar PV energy envisions that PV will contribute 11 % to the global energy production in the year 2050, which corresponds to 3'000 GW of installed capacity [9].

Crystalline Si (c-Si) modules take the main share with 85–90% of the global annual PV technologies market. Two main categories of c-Si modules exist: i) single crystalline (sc-Si) and ii) multi-crystalline (mc-Si). These first generation solar cells are very efficient, however, their production is energy intensive, emitting between 39 to 49 % CO_2-eq/kWh during production, depending on the study [10]. A further disadvantage is that it needs a relatively thick layer of silicon (> 200 μm) due to the low absorption coefficient of Si.

Second generation solar cells are typically multijunction cells and usually thin layers of light absorbing material are applied. Thin film PV panels are subdivided into three main families, which altogether account for roughly 10% to 15% of global solar panel sales. They are: i) amorphous (a-Si) and micromorph silicon (a-Si/μm-Si), ii) Cadmium–Telluride (CdTe), and iii) Copper-Indium-Diselenide (CIS) as well as Copper-Indium-Gallium-Diselenide (CIGS). As the name indicates thin film panels are only a few μm thick, therefore reducing the material expenses which makes thin film modules cheaper and more competitive in spite of the lower efficiencies compared to c-Si panels.

Related to Cd and Se there are important concerns related to environmental damage they might cause when released to the environment. Cd is carcinogenic, high levels of Se are toxic. CdTe is also toxic if dusts are inhaled or if ingested. However, Fthenakis pointed out that ultimately Cd is not as harmful when it is used in CdTe PV cells because it is encapsulated within glass substrate and,

therefore, protected [11]. Cd is produced as a byproduct during the production of Zn, if it were not used it would end up in wastes that are finally deposited on landfills, with its own risks of contamination. In addition, PV modules are more likely to be recycled than for instance Ni–Cd batteries. Despite such more pragmatic argumentation, governmental policies tend to ban PV materials based on toxic compounds if they do not pass rigorous tests.

Nowadays, 3rd generation solar cells are investigated. The most efficient example are dye sensitized solar cells (DSSCs). Here, ruthenium-based organic dyes sensitize mesoporous TiO_2 nanoparticles [12]. The dyes absorb the light instead of a thin film semiconductor and inject the excited electron into the TiO_2 conduction band (CB). They are flexible, some are printable, large area constructions are possible and they can be easily integrated almost everywhere. The potential for low cost production is substantial.

1.3 Alternative semiconductor materials

The commonly used semiconductor materials for recent thin film panels, like CdTe and CIGS, have a major flaw in that they employ scarce materials like Te, In and Ga [13–15]. This limits the midterm up scaling of the related thin film panels. Consequently, the search for alternative material gets more intense and important. In a recently published review, Hossain and Alharbi present several promising alternative semiconductor materials that could be used for solar cell production [16]. Their focus was on binary and environmentally friendly compounds used in thin film devices. Similar screenings were performed earlier by Wadia *et al.* [17] and Alharbi *et al.* [18]. Both studies incorporated abundance and toxicity in their respective models. Wadia *et al.* also implemented the material extraction costs in order to evaluate a certain material.

The three studies indentified several sulfides (FeS_2, CuS, Cu_2S, SnS, WS_2, MoS_2), oxides (CuO, Cu_2O), silicides (β-$FeSi_2$, β-$BaSi_2$) and Zn_3P_2 as potential alternative materials. All these compounds possess high absorption coefficients; they would need less than 1 μm to absorb most of the light. However, the PV cell efficiency is not only about maximizing the absorption, but also about to have a long as possible diffusion length of the charge carriers. Crystalline Si for instance has a diffusion length L_{diff} of 244 μm [19], which is the reason why Si

based solar cells work so well despite their low absorption capabilities. WS_2 has a very promising L_{diff} = 200 μm [20] and there is indeed recent work that reports high performances above 25 % [21, 22].

Next to WS_2, iron pyrite or fool's gold, FeS_2, has in principle the perfect properties for its application in solar cells. High abundance and non-toxicity together with very strong optical absorption properties makes it a very interesting alternative to today's thin film materials. Film thicknesses of as little as 250 nm are possible to absorb most of the light but unfortunately, the short L_{diff} of 1.0 μm [23] hamper the perfect picture.

1.4 Quantum dot sensitized solar cells

There exist a few types of photovoltaic device structures: p-n or homojunction device, Schottky devices, and heterojunction device structures. All of them make use of the photovoltaic effect, discovered in 1839 by Alexandre Edmond Becquerel. It consists in the build up of a potential difference at the junction of two materials, driven by radiation. Photons whose energy matches the band gap of the light absorbing material excite an electron from the valence band (VB) into the conduction band, thus creating an electron–hole ($e^- - h^+$) pair, often called exciton.

The basic functioning of quantum dot sensitized solar cells (QDSSCs) is illustrated in Fig. 1.3. It is similar to that of DSSCs, however, instead of a dye, a nanometer-sized cluster of a semiconductor, the quantum dot (QD), absorbs the photon and then injects it into wide band gap semiconductors like TiO_2 or ZnO. The positive charge is quenched by the electrolyte. What is most interesting about QDs is that they can generate more than one excited electron from a single photon, therefore, the Shockley–Queisser limit [24] of 33.7 %, inherit to p-n junction solar cells, is not valid anymore and the theoretical limit to the solar conversion increases to 42 % [25].

Quantum dots are not only used in solar cells. Different applications may be fluorescent labeling in biological systems [26], quantum computing [27, 28], lasing [29], and light-emitting diodes [30, 31]. In QDSSCs, however, there are certain semiconductor materials that are mainly used as sensitizer, these materials with the corresponding band gap energies are listed in Table 1.1. They

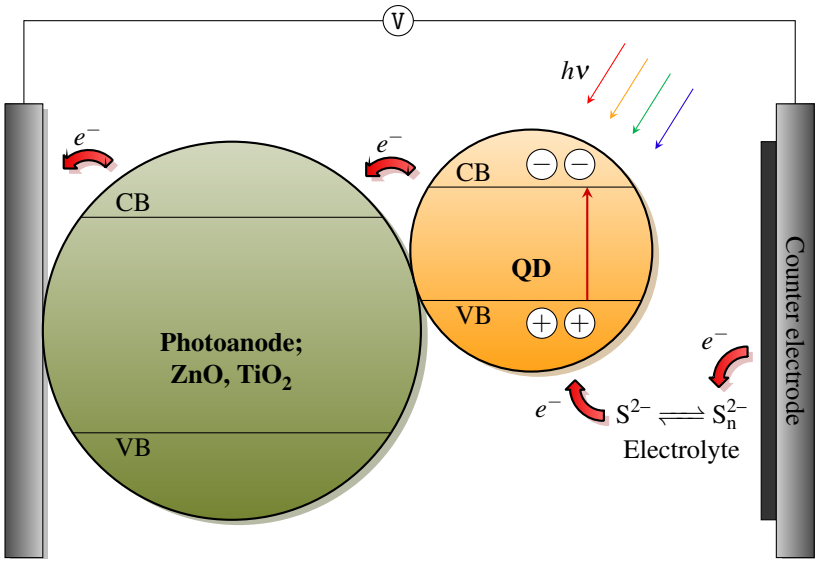

FIG. 1.3 Schematic of a QDSSC. Light with the energy $h\nu$ excites an electron from the QD valence band into the CB, leaving a positive charge in the VB. The electron is then transferred from the CB into TiO_2's CB, from where it will enter the external circuit. The counter electrode on the right-hand side injects an electron into the polysulfide electrolyte, which itself scavenges the hole in the QD's CB. In the case of MEG two or more $e^- - h^+$ pairs would be generated.

typically sensitize mesoporous, wide gap semiconductors like TiO_2, ZnO, or SnO_2.

Because of the 3–dimensional confinement of the quantum-mechanical wavefunction and its localization in a very small space, they are also called "artificial atoms". Hence, an excited electron will not translocate freely in the CB as it would do in a bulk semiconductor, but rather it will be bound to its corresponding hole due to coulombic interactions.

Spanhel *et al.* belong to the first ones to sensitize TiO_2 with colloidal CdS nanoclusters [59]. In this early work, they found that fluorescence of the colloidal suspension was effectively quenched through rapid electron injection from the illuminated CdS into the conduction band of TiO_2 occurs. Subsequent to this work conducted in the late 1980s, Henglein reported a size dependency of the absorption spectrum [60, 61]. The energy levels of smaller sized nanoclusters become quantized and the effective mass of the excited electron is smaller

than in bulk systems. The dependency was related to the size of the cluster: the smaller the diameter the more the absorption maximum shifts to higher energies.

It was found relatively soon by Henglein that nanocrystals with a given diameter are exceptionally stable [60]. He created the expression "magic" agglomeration numbers. Later, there were more researchers that dedicated time to investigate these so called magic sized clusters (MSCs). They mostly did fine-tune the experimental conditions necessary to obtain a desired cluster size [62–65]. There were also theoretical attempts to characterize systematically the shape of the most stable clusters [66–70].

QD synthesis is readily performed under mild conditions in solution and at temperatures below 100° C. Also, the choice of solvent and ligand used to stabilize the cluster define the QD diameter. The diameter, in turn, changes the band gap of the cluster, which itself determines the absorption wavelength. For CdTe, CdSe and CdS, Yu *et al.* propose empirical fitting functions to calculate the diameter depending on the absorption maximum [71]. The dependence of the absorption wavelength on the QD diameter can be used to exploit a wider range of the solar light spectrum by combining QDs with different diameters.

Quantum dots attract so much attention also due to the phenomenon of multiple exciton generation (MEG). The basic principle of MEG is that upon absorption of a photon with energy at least two times higher than the band gap of the cluster, it is possible that a second electron will be excited when the first one emits its excess energy when it falls to the conduction band edge.

Recombination processes occurring upon MEG, so called Auger processes, hobble the usage of multiple excitons and potentially limit the efficiency gains. They occur on very small timescales and it is crucial to avoid them for to har-

TABLE 1.1 Typical semiconductor materials employed for quantum dots and their respective band gap.

Material	E_g, [eV]
CdS [32–36]	2.5
CdSe [37–46]	1.7
InAs [47]	0.36
PbS [33, 48]	0.41
Ag_2S [49]	1.0
FeS_2 [23, 50–52]	0.95
Cu_2S [53–58]	1.21

vest the largest possible number of excitons generated by one photon. For a more complete overview about MEG in relation to solar energy conversion, we refer the interested reader to the summary by Klimov and references within [72]. From a computational point of view, we recommend the review article of Prezhdo where he summarizes the work on multiple excitons realized in his group [73].

Of course, exciton recombination also occurs when only one exciton has been generated. In terms of solar cells, recombination is the competing process to electron injection into the semiconductor. Ultimately, they influence the efficiency of the solar cell. To avoid exciton recombination, the holes generated in the QD need to be quenched as fast as possible by the electrolyte. In QDSSCs a popular redox pair is, for instance, the sulfide/polysulfide redox couple S^{2-}/S_n^{2-} [74–78]. Just recently, polysaccharide Konjac glucomannan was used as the electrolyte in a QDSSC [79].

Besides, the morphology of the wide band gap semiconductor influences the electron injection rate. Kongkanand *et al.* investigated how the morphology of the TiO_2 nanostructures affects electron transport and injection [80]. They found that the TiO_2 nanoparticles and nanotubes have the same electron injection rate from CdSe into TiO_2 nanostructure. However, TiO_2 nanotubes have enhanced electron transport properties over nanoclusters, which is reflected in higher incident photon to current conversion efficiency (IPCE) values. Similarly, Shen *et al.* did also observe that the photoelectrochemical current (PECC) depends on the microstructure and the electron diffusion coefficient in the TiO_2 electrodes [81]. Apart from different TiO_2 morphologies exist attempts to use DNA molecules as a photonic wire [82]. Boeneman *et al.* use CdSe–ZnS core–shell QDs as the light harvesting species. From there, the excited electron will be transferred via a dye-labeled DNA wire.

The injection rate of the photoexcited electron into the conduction band of the semiconductor can be evaluated in terms of Marcus theory for a nonadiabatic reaction in the classical limit [83, 84]. The electron transfer rate depends on the driving force, $-\Delta G$, and has been used to describe charge recombination kinetics in DSSC systems [85–87]. $-\Delta G$ of TiO_2 sensitized with CdSe is dominated by the difference between the two conduction band energies. The band gap increases with a decreasing cluster size, also, the CB lies closer to the TiO_2

CB because it shifts stronger than the VB does. It results that the electron injection occurs faster for smaller QDs [80]. The fastest rate of 1.2×10^{10} s^{-1} was reported for 2.4 nm CdSe dots by Robel *et al.* [37].

A different problem that most negatively influences the overall solar cell efficiency is that of surface trap states. On the brink of the 1980s, Henglein pointed out the effect of surface modification [61]. Trapped charge carriers were found to recombine radiatively and emit light in the infrared region. CdS QDs with unmodified surface possess fluorescence that is 0.4 eV below the absorption threshold. However, it is localized right at the absorption threshold when a $S^{2-}Cd^{2+}OH^{-}$ structure formed on the cluster surface. This passivates the CdS cluster surface and, consequently, avoids the formation of trap states.

Such trapped charges are highly unwanted as this decreases the electron injection rate into the semiconductor [88] and, furthermore, increases the probability of a reverse electron transfer reaction. Obviously, the rates of electron injection and quenching of the hole by the electrolyte must be equal or at least similar in order to allow rapid electron transport. If this is not the case then the QD becomes saturated and exciton generation is not possible anymore [89].

There are two techniques to avoid surface trap states. One is to grow a protective "shell" made from a second semiconductor around the photoactive cluster [90–96]. The combination of the shell and the core material should be as such that their band gaps clearly differ, for example a low-band-gap core combined with a high-band-gap shell, and vice versa.

The second approach is to saturate potential surface traps with organic or inorganic ligand molecules. In his review, Green identifies a few different types of ligands commonly used in QD synthesis: trioctylphosphines (TOP), amines, thiols, carboxylic acids, as well as some non-standard ligands [97]. Typically, ligands with long, aliphatic chains are employed during the synthesis of colloidal nanoclusters. This way the QDs can be stabilized at the desired diameter, which can be tuned by changing, for instance, the composition of the solvent/ligand mixture. The drawback of large chains is that they reduce the electron injection rate into the semiconductor to be sensitized due to the spatial separation of QD and semiconductor. As a consequence, electronic coupling between them is diminished. However, as soon as the QDs are synthesized and separated, the ligands can easily be exchanged by standard surfactant exchange procedures

[98].

In order to enhance the wavefunction overlap between QD and semiconductor, organic molecules are used to link them. A typical linker is mercaptopropionic acid (MPA). Its two functional groups on either side of the molecule are used to link a QD to TiO_2 nanoparticles [99]. The thiol group binds to the QD surface while the carboxylic acid group binds to TiO_2. This linker was reported to enhance the efficiency of CdSe sensitized TiO_2 solar cells in comparison to directly attached CdSe quantum dots [100]. Mora-Seró *et al.* and Margraf *et al.* reported that the use of cysteine as a linker instead of MPA increases the cell performance even more [101, 102].

Dopamine is a different molecule used to link QDs with the TiO_2 surface. Structurally, it belongs to the catecholamine and phenethylamine classes. It is mainly used in biosensing applications. Medintz *et al.* use dopamine as quencher of the QD photoluminescence via transport of the photoexcited electron from the CB into the LUMO of the dopamine molecule [26]. Organic conjugated molecules like alizarin and catechol are also employed for biosensing with QD. Besides, they successfully sensitize TiO_2 nanoparticles; the underlying processes are thoroughly investigated both experimentally and theoretically [103–108]. The structural similarity of dopamine and catechol, the amine group on the one side of dopamine, and the fact that it quenches the QD photoluminescence, make it an interesting candidate as a linker molecule between QDs and TiO_2.

1.4.1 Iron pyrite as an alternative QD sensitizer

As indicated in Table 1.1 on page 16, also iron pyrite can be prepared as quantum dot [50, 52, 109, 110]. The crystallites were found cubic in shape, and the absorption band maximum has the same dependence on the cluster size as other nanosized clusters. The cubic pyrite structure in bulk phase leads to a splitting of the iron $3d$ states into orbitals of t_{2g} and e_g symmetry. The t_{2g} orbitals form a completely filled, highly localized band. It is non-bonding in character. Three S sp^3 orbitals hybridize with the Fe e_g orbital. They form, together with the Fe $4s$ and $4p$ orbitals, the conduction band, a band with σ^* symmetry. Pursuant to Wilcoxon *et al.* the band gap for FeS_2 nanocluster in the quantum confinement regime remains of indirect character [50].

Especially the optical properties of this material make pyrite such an interesting light absorber, despite the difficult shape control. The absorption coefficient $\alpha > 10^5$ cm^{-1} for photon energies larger than 1.3 eV and high quantum efficiencies above 90 % [23, 110, 111] render pyrite an ideal solar cell material. It is a p-type semiconductor with a direct band gap of 0.95 eV and an indirect band gap at 1.3 eV. Very thin films are possible with it ($<$ 250 nm). Unfortunately, the open voltage current, V_{oc}, is very low leading to small photovoltages below 200 mV and short diffusion lengths. Consequently, there are opinions that doubt that pyrite can successfully be used in solar cells [112].

The low photovoltages are generally attributed to sulfur vacancies [113]. Birkholz *et al.* pointed out that the S vacancy concentration should be reduced and that the actual pyrite PV material needs S:Fe ratios of as close to 2 as possible to get higher photovoltages and, consequently, more efficient PV panels based on FeS_2 [113].

Yet, Yu *et al.* reported that S deficiencies are formed because of the coexistence of the pyrite FeS_2 phase with a S deficient FeS phase [114]. They further observed crystalline FeS_2 grains coated with sulfur-deficient phases. Such S vacancies and surface defects occur mostly during the production process of thin films and it is very difficult to suppress them. Yu *et al.* calculated that a (001)-FeS_2 surface without S deficiencies has a 0.3 eV smaller band gap with respect to bulk, but it becomes metallic when there are vacancies present on the surface [114].

However, Kirkeminde *et al.* managed to synthesize FeS_2 nanoplates that have a V_{oc} of 0.78 V [115] but they only get efficiencies of 0.03 %. Still, such a high V_{oc} is intriguing since the authors attribute the low efficiency to the sample quality, which leaves room for improvements. Actually, they work on doping of the pyrite samples with Zn or Li, replacing parts of the Fe atoms.

Yu *et al.* followed a different approach to prevent S defects formation. They searched for ternary, Fe containing compounds that maintain the octahedric coordination of Fe with six S atoms, which ensures that the ligand-field splitting is sufficiently large to obtain a band gap well suited for solar light absorption [114]. They found Fe_2MS_4, where M = Si or Ge, compounds that adopt an olivine structure where Fe indeed is six-fold coordinated. These ternary compounds could avoid the coexistence of S deficient FeS phases with FeS_2, consequently

avoiding the problems otherwise characteristic of binary pyrite systems.

Synthesis of phase-pure iron pyrite crystals is difficult to achieve; it is even more difficult to control the shape of these nanoclusters. Only little work has been conducted on this subject [109, 115–118]. From a theoretical point of view, FeS_2 is a difficult system to model. While it is relatively easy task to cut a spherical cluster out of bulk CdSe, it is not so trivial in the case of FeS_2. Cube shaped crystals of pyrite expose the (001) facets, which is the most stable facet under S-lean conditions [119]. It is quite straight forward to model a 2-dimensional slab, but when a cube should be modeled then a high number of unsaturated bonds will form owing to the high surface:core ratio. Without doubt, the surface undergoes strong restructuring when it is optimized, which in turn will affect the electronic structure and the absorption spectrum of the cluster.

Despite of these obstacles on the way to employ pyrite as sensitizer in QDSSCs, it does remain an interesting material as an economic, non-toxic alternative to today's PV materials due to its advantages mentioned earlier.

1.5 Purpose and motivation

The main motivation of this thesis is founded in the strong interest in renewable energies, more precisely the photovoltaic energy production. There is no way around renewable energies; by and large they are more environmental friendly than carbon based forms of energy, even if the whole production cycle is included to get the balance. Moreover, and most importantly, they represent the only form of energy, either as electricity or as fuel, which can be produced in a sustainable fashion that does not depend on any finite resources.

The subject of quantum dot sensitized solar cells is subsequent to the work performed earlier in our group about dye-sensitized solar cells. The methodology is similar, besides TiO_2 nanoparticles we sensitize also periodic nanotubes based on TiO_2 anatase. At first, the chosen sensitizing material is CdSe,a well known semiconductor material with a wide range of applications. Its QD properties was investigated to quite some degree and, therefore, serves well as test and benchmark system. On it, different basis sets and functionals were tested. Once the methodology is specified, we apply it on differently sized CdSe clusters. Also the influence of different aliphatic and aromatic ligands is investigated.

The main focus lies on the electronic structure of the QDs and on the analysis of the optical absorption spectra that we calculate for the main part of the systems employed throughout the thesis.

In a next step, the properties of TiO_2 nanoparticles and nanotubes are analyzed. Then, these systems are sensitized with CdSe quantum dots, thereby simulating the QDSSC. A variety of different QD-TiO_2 models are employed, CdSe is added to TiO_2 as bare or ligated clusters, furthermore, two different sizes of CdSe clusters are used as sensitizer. Since the adsorption mode of the QD on TiO_2 is an important parameter for the electron transport from the QD to the semiconductor, we adsorb CdSe clusters directly on the TiO_2 nanotubes or via an organic linker molecule. In this work, these linkers are mercaptopropionic acid and dopamine. While the former is a molecule typically employed as linker, dopamine is chosen mainly because of its aromatic structure that might facilitate electron transfer.

For iron pyrite, FeS_2, we first have to change slightly the theoretical level of computation. The problem with the PBE functional is that it is not suited for the investigation of systems with small band gaps like pyrite because PBE underestimates it substantially. Therefore, we determined the effective parameter U for to apply it within the framework of DFT+U. With it, the band gap is reproduced much better. Electronic and optical properties of the bulk system and the S terminated (001) surface of FeS_2 are preliminary obtained. Finally, three different FeS_2 clusters are employed, which are passivated with an aromatic ligand in order to observe the impact it might have on the spectrum of FeS_2 clusters.

1.6 Bibliography

[1] Tyndall, J., *Philos. Mag. ser. 4* **1861**, *22*, 169.

[2] Tyndall, J., *Philos. Mag. ser. 4* **1863**, *25*, 200.

[3] Tyndall, J., *Philos. Mag. ser. 4* **1863**, *26*, 30.

[4] Arrhenius, S., *Philos. Mag. ser. 5* **1896**, *41*, 237.

[5] Ångström, K., *Ann. Phys.* **1900**, *308*, 720.

[6] NASA, *GISS Surface Temperature Analysis* **2013**. `http://data.giss.nasa.gov/gistemp/`.

[7] World Bank, *Energy use per capita* **2012**. `http://data.worldbank.org/`

indicator/EG.USE.PCAP.KG.OE.

[8] International Energy Agency, *Renewable Energy Essentials: Hydropower* **2010**. http://www.iea.org/publications/freepublications/publication/Hydropower_Essentials-1.pdf.

[9] International Energy Agency, *Technology Roadmap Solar photovoltaic energy* **2010**. http://www.iea.org/publications/freepublications/publication/pv_roadmap.pdf.

[10] Hsu, D. D.; O'Donoughue, P.; Fthenakis, V.; Heath, G. A.; Kim, H. C.; Sawyer, P.; Choi, J.-K.; Turney, D. E., *J. Ind. Ecol.* **2012**, *16*, 122.

[11] Fthenakis, V. M., *Renew. Sust. Energ. Rev.* **2004**, *8*, 303.

[12] O'Regan, B.; Grätzel, M., *Nature* **1991**, *353*, 737.

[13] Andersson, B. A., *Prog. Photovolt: Res. Appl.* **2000**, *8*, 61.

[14] Fthenakis, V., *Renew. Sust. Energ. Rev.* **2009**, *13*, 2746.

[15] Candelise, C.; Winskel, M.; Gross, R., *Prog. Photovolt: Res. Appl.* **2012**, *20*, 816.

[16] Hossain, M. I.; Alharbi, F. H., *Mater. Technol.* **2013**, *28*, 88.

[17] Wadia, C.; Alivisatos, A. P.; Kammen, D. M., *Environ. Sci. Technol.* **2009**, *43*, 2072.

[18] Alharbi, F.; Bass, J. D.; Salhi, A.; Alyamani, A.; Kim, H.-C.; Miller, R. D., *Renew. Energ.* **2011**, *36*, 2753.

[19] Stutenbaeumer, U.; Lewetegn, E., *Renew. Energ.* **2000**, *20*, 65.

[20] Baglio, J. A.; Calabrese, G. S.; Kamieniecki, E.; Kershaw, R.; Kubiak, C. P.; Ricco, A. J.; Wold, A.; Wrighton, M. S.; Zoski, G. D., *J. Electrochem. Soc.* **1982**, *129*, 1461.

[21] Liu, L.; Kumar, S.; Ouyang, Y.; Guo, J., *Electron Devices, IEEE Transactions on* **2011**, *58*, 3042.

[22] Hwang, W. S.; Remskar, M.; Yan, R.; Protasenko, V.; Tahy, K.; Chae, S. D.; Zhao, P.; Konar, A.; Xing, H. G.; Seabaugh, A.; Jena, D., *Appl. Phys. Lett.* **2012**, *101*, 013107.

[23] Altermatt, P. P.; Kiesewetter, T.; Ellmer, K.; Tributsch, H., *Sol. Energy Mater. Sol. Cells* **2002**, *71*, 181.

[24] Shockley, W.; Queisser, H. J., *J. Appl. Phys.* **1961**, *32*, 510.

[25] Brendel, R.; Werner, J. H.; Queisser, H. J., *Sol. Energy Mater. Sol. Cells* **1996**, *41–42*, 419.

[26] Medintz, I. L.; Stewart, M. H.; Trammell, S. A.; Susumu, K.; Delehanty, J. B.; Mei, B. C.; Melinger, J. S.; Blanco-Canosa, J. B.; Dawson, P. E.; Mattoussi, H., *Nat. Mater.* **2010**, *9*, 676.

[27] Loss, D.; DiVincenzo, D. P., *Phys. Rev. A* **1998**, *57*, 120.

[28] Medintz, I. L.; Farrell, D.; Susumu, K.; Trammell, S. A.; Deschamps, J. R.; Brunel, F. M.; Dawson, P. E.; Mattoussi, H., *Anal. Chem.* **2009**, *81*, 4831.

[29] Coleman, J.; Young, J.; Garg, A., *J. Lightwave Technol.* **2011**, *29*, 499.

[30] Jang, E.; Jun, S.; Jang, H.; Lim, J.; Kim, B.; Kim, Y., *Adv. Mater.* **2010**, *22*, 3076.

[31] Sun, L.; Choi, J. J.; Stachnik, D.; Bartnik, A. C.; Hyun, B.-R.; Malliaras, G. G.; Hanrath, T.; Wise, F. W., *Nat. Nano* **2012**, *7*, 369.

[32] Chang, C.-H.; Lee, Y.-L., *Appl. Phys. Lett.* **2007**, *91*, 053503.

[33] Lee, H. J.; Chen, P.; Moon, S.-J.; Sauvage, F.; Sivula, K.; Bessho, T.; Gamelin, D. R.; Comte, P.; Zakeeruddin, S. M.; Seok, S. I.; Grätzel, M.; Nazeeruddin, M. K., *Langmuir* **2009**, *25*, 7602.

[34] Lee, W.; Min, S. K.; Dhas, V.; Ogale, S. B.; Han, S.-H., *Electrochem. Commun.* **2009**, *11*, 103.

[35] Zhang, Q.; Zhang, Y.; Huang, S.; Huang, X.; Luo, Y.; Meng, Q.; Li, D., *Electrochem. Commun.* **2010**, *12*, 327.

[36] Zhang, Q.; Guo, X.; Huang, X.; Huang, S.; Li, D.; Luo, Y.; Shen, Q.; Toyoda, T.; Meng, Q., *Phys. Chem. Chem. Phys.* **2011**, *13*, 4659.

[37] Robel, I.; Kuno, M.; Kamat, P. V., *J. Am. Chem. Soc.* **2007**, *129*, 4136.

[38] Leschkies, K. S.; Divakar, R.; Basu, J.; Enache-Pommer, E.; Boercker, J. E.; Carter, C. B.; Kortshagen, U. R.; Norris, D. J.; Aydil, E. S., *Nano Lett.* **2007**, *7*, 1793.

[39] Lopez-Luke, T.; Wolcott, A.; Xu, L.-p.; Chen, S.; Wen, Z.; Li, J.; De La Rosa, E.; Zhang, J. Z., *J. Phys. Chem. C* **2008**, *112*, 1282.

[40] Bang, J. H.; Kamat, P. V., *ACS Nano* **2009**, *3*, 1467.

[41] Chen, J.; Song, J. L.; Sun, X. W.; Deng, W. Q.; Jiang, C. Y.; Lei, W.; Huang, J. H.; Liu, R. S., *Appl. Phys. Lett.* **2009**, *94*, 153115.

[42] Fuke, N.; Hoch, L. B.; Koposov, A. Y.; Manner, V. W.; Werder, D. J.; Fukui, A.; Koide, N.; Katayama, H.; Sykora, M., *ACS Nano* **2010**, *4*, 6377.

[43] Gao, X.-F.; Sun, W.-T.; Ai, G.; Peng, L.-M., *Appl. Phys. Lett.* **2010**, *96*, 153104.

[44] Guijarro, N.; Lana-Villarreal, T.; Shen, Q.; Toyoda, T.; Gómez, R., *J. Phys. Chem. C* **2010**, *114*, 21928.

[45] Hensel, J.; Wang, G.; Li, Y.; Zhang, J. Z., *Nano Lett.* **2010**, *10*, 478.

[46] Martinez-Ferrero, E.; Sero, I. M.; Albero, J.; Gimenez, S.; Bisquert, J.; Palomares, E., *Phys. Chem. Chem. Phys.* **2010**, *12*, 2819.

[47] Yu, P.; Zhu, K.; Norman, A. G.; Ferrere, S.; Frank, A. J.; Nozik, A. J., *J. Phys. Chem. B* **2006**, *110*, 25451.

[48] Vogel, R.; Hoyer, P.; Weller, H., *J. Phys. Chem.* **1994**, *98*, 3183.

[49] Tubtimtae, A.; Wu, K.-L.; Tung, H.-Y.; Lee, M.-W.; Wang, G. J., *Electrochem. Commun.* **2010**, *12*, 1158.

[50] Wilcoxon, J. P.; Newcomer, P. P.; Samara, G. A., *Solid State Commun.* **1996**, *98*, 581.

[51] Fang, J. H.; Wu, J. W.; Su, L. Y.; Zhang, X. Y.; Lu, Z. H., *Chem. Lett.* **1997**, *26*, 149.

[52] Bedja, I., *Mater. Sci.-Poland* **2011**, *29*, 171.

[53] Pakeva, S.; Germanova, K., *J. Phys. D: Appl. Phys.* **1985**, *18*, 1371.

[54] Chen, S.; Huang, Y.; Liu, Y.; Xia, Q.; Liao, H.; Long, C., *Mater. Lett.* **2008**, *62*, 2503.

[55] Li, S.; Wang, H.; Xu, W.; Si, H.; Tao, X.; Lou, S.; Du, Z.; Li, L. S., *J. Colloid Interface Sci.* **2009**, *330*, 483.

[56] Tang, A.; Qu, S.; Li, K.; Hou, Y.; Teng, F.; Cao, J.; Wang, Y.; Wang, Z., *Nanotechnology* **2010**, *21*, 285602.

[57] Kriegel, I.; Jiang, C.; Rodríguez-Fernández, J.; Schaller, R. D.; Talapin, D. V.; da Como, E.; Feldmann, J., *J. Am. Chem. Soc.* **2011**, *134*, 1583.

[58] Lotfipour, M.; Machani, T.; Rossi, D. P.; Plass, K. E., *Chem. Mater.* **2011**, *23*, 3032.

[59] Spanhel, L.; Weller, H.; Henglein, A., *J. Am. Chem. Soc.* **1987**, *109*, 6632.

[60] Henglein, A., *Top. Curr. Chem.* **1988**, *143*, 113.

[61] Henglein, A., *Chem. Rev.* **1989**, *89*, 1861.

[62] Kudera, S.; Zanella, M.; Giannini, C.; Rizzo, A.; Li, Y.; Gigli, G.; Cingolani, R.; Ciccarella, G.; Spahl, W.; Parak, W.; Manna, L., *Adv. Mater.* **2007**, *19*, 548.

[63] Sun, M.; Yang, X., *J. Phys. Chem. C* **2009**, *113*, 8701.

[64] Dukes, A. D.; McBride, J. R.; Rosenthal, S. J., *Chem. Mater.* **2010**, *22*, 6402.

[65] Yu, K.; Hu, M. Z.; Wang, R.; Piolet, M. L.; Frotey, M.; Zaman, M. B.; Wu, X.; Leek, D. M.; Tao, Y.; Wilkinson, D.; Li, C., *J. Phys. Chem. C* **2010**, *114*, 3329.

[66] Kasuya, A.; Sivamohan, R.; Barnakov, Y. A.; Dmitruk, I. M.; Nirasawa, T.; Romanyuk, V. R.; Kumar, V.; Mamykin, S. V.; Tohji, K.; Jeyadevan, B.; Shinoda, K.; Kudo, T.; Terasaki, O.; Liu, Z.; Belosludov, R. V.; Sundararajan, V.; Kawazoe, Y., *Nat. Mater.* **2004**, *3*, 99.

[67] Puzder, A.; Williamson, A. J.; Zaitseva, N.; Galli, G.; Manna, L.; Alivisatos, A. P., *Nano Lett.* **2004**, *4*, 2361.

[68] Puzder, A.; Williamson, A. J.; Gygi, F.; Galli, G., *Phys. Rev. Lett.* **2004**, *92*, 217401.

[69] He, J.; Liu, C.; Li, F.; Sa, R.; Wu, K., *Chem. Phys. Lett.* **2008**, *457*, 163.

[70] Nguyen, K. A.; Day, P. N.; Pachter, R., *J. Phys. Chem. C* **2010**, *114*, 16197.

[71] Yu, W. W.; Qu, L.; Guo, W.; Peng, X., *Chem. Mater.* **2003**, *15*, 2854.

[72] Klimov, V. I., *J. Phys. Chem. B* **2006**, *110*, 16827.

[73] Prezhdo, O. V., *Chem. Phys. Lett.* **2008**, *460*, 1.

[74] Ellis, A. B.; Kaiser, S. W.; Wrighton, M. S., *J. Am. Chem. Soc.* **1976**, *98*, 1635.

[75] Ellis, A. B.; Kaiser, S. W.; Wrighton, M. S., *J. Am. Chem. Soc.* **1976**, *98*, 6855.

[76] Vainas, B.; Hodes, G.; Dubow, J., *J. Electroanal. Chem. Interfacial Electrochem.* **1981**, *130*, 391.

[77] Tenne, R.; Lando, D.; Mirovsky, Y.; Müller, N.; Manassen, J.; Cahen, D.; Hodes, G., *J. Electroanal. Chem. Interfacial Electrochem.* **1983**, *143*, 103.

[78] Chakrapani, V.; Baker, D.; Kamat, P. V., *J. Am. Chem. Soc.* **2011**, *133*, 9607.

[79] Wang, S.; Zhang, Q.-X.; Xu, Y.-Z.; Li, D.-M.; Luo, Y.-H.; Meng, Q.-B., *J. Power Sources* **2013**, *224*, 152.

[80] Kongkanand, A.; Tvrdy, K.; Takechi, K.; Kuno, M.; Kamat, P. V., *J. Am. Chem. Soc.* **2008**, *130*, 4007.

[81] Shen, Q.; Arae, D.; Toyoda, T., *J. Photochem. Photobiol., A* **2004**, *164*, 75.

[82] Boeneman, K.; Prasuhn, D. E.; Blanco-Canosa, J. B.; Dawson, P. E.; Melinger, J. S.; Ancona, M.; Stewart, M. H.; Susumu, K.; Huston, A.; Medintz, I. L., *J. Am. Chem. Soc.* **2010**, *132*, 18177.

[83] Marcus, R. A., *J. Chem. Phys.* **1965**, *43*, 679.

[84] Marcus, R.; Sutin, N., *BBA-Bioenergetics* **1985**, *811*, 265.

[85] Gaal, D. A.; Hupp, J. T., *J. Am. Chem. Soc.* **2000**, *122*, 10956.

[86] Kuciauskas, D.; Freund, M. S.; Gray, H. B.; Winkler, J. R.; Lewis, N. S., *J. Phys. Chem. B* **2000**, *105*, 392.

[87] Clifford, J. N.; Palomares, E.; Nazeeruddin, M. K.; Grätzel, M.; Nelson, J.; Li, X.; Long, N. J.; Durrant, J. R., *J. Am. Chem. Soc.* **2004**, *126*, 5225.

[88] Nozik, A. J., *Physica E* **2002**, *14*, 115.

[89] Gregg, B. A., *J. Phys. Chem. B* **2003**, *107*, 4688.

[90] Kilin, D. S.; Tsemekhman, K.; Prezhdo, O. V.; Zenkevich, E. I.; von Borczyskowski, C., *J. Photochem. Photobiol., A* **2007**, *190*, 342.

[91] Chon, B.; Lim, S. J.; Kim, W.; Seo, J.; Kang, H.; Joo, T.; Hwang, J.; Shin, S. K., *Phys. Chem. Chem. Phys.* **2010**, *12*, 9312.

[92] Jing, P.; Yuan, X.; Ji, W.; Ikezawa, M.; Wang, Y. A.; Liu, X.; Zhang, L.; Zhao, J.; Masumoto, Y., *J. Phys. Chem. C* **2010**, *114*, 19256.

[93] Ning, Z.; Tian, H.; Qin, H.; Zhang, Q.; Ågren, H.; Sun, L.; Fu, Y., *J. Phys. Chem. C* **2010**, *114*, 15184.

[94] Frenzel, J.; Thieme, S.; Seifert, G.; Joswig, J.-O., *J. Phys. Chem. C* **2011**, *115*, 10338.

[95] Jiang, Z.-J.; Kelley, D. F., *J. Phys. Chem. C* **2011**, *115*, 4594.

[96] Dworak, L.; Matylitsky, V. V.; Breus, V. V.; Braun, M.; Basché, T.; Wachtveitl, J., *J. Phys. Chem. C* **2011**, *115*, 3949.

[97] Green, M., *J. Mater. Chem.* **2010**, *20*, 5797.

[98] Smith, A. M.; Duan, H.; Rhyner, M. N.; Ruan, G.; Nie, S., *Phys. Chem. Chem. Phys.* **2006**, *8*, 3895.

[99] Robel, I.; Subramanian, V.; Kuno, M.; Kamat, P. V., *J. Am. Chem. Soc.* **2006**, *128*, 2385.

[100] Guijarro, N.; Lana-Villarreal, T.; Mora-Seró, I.; Bisquert, J.; Gómez, R., *J. Phys. Chem. C* **2009**, *113*, 4208.

[101] Mora-Seró, I.; Giménez, S.; Moehl, T.; Fabregat-Santiago, F.; Lana-Villareal, T.; Gómez, R.; Bisquert, J., *Nanotechnology* **2008**, *19*, 424007.

[102] Margraf, J. T.; Ruland, A.; Sgobba, V.; Guldi, D. M.; Clark, T., *Langmuir* **2013**, *29*, 2434.

[103] Huber, R.; Spörlein, S.; Moser, J. E.; Grätzel, M.; Wachtveitl, J., *J. Phys. Chem. B* **2000**, *104*, 8995.

[104] Huber, R.; Moser, J.-E.; Grätzel, M.; Wachtveitl, J., *J. Phys. Chem. B* **2002**, *106*, 6494.

[105] Matylitsky, V. V.; Lenz, M. O.; Wachtveitl, J., *J. Phys. Chem. B* **2006**, *110*, 8372.

[106] Prezhdo, O. V.; Duncan, W. R.; Prezhdo, V. V., *Prog. Surf. Sci.* **2009**, *84*, 30.

[107] Sánchez-de Armas, R.; Oviedo López, J.; A. San-Miguel, M.; Sanz, J. F.; Ordejón, P.; Pruneda, M., *J. Chem. Theory Comput.* **2010**, *6*, 2856.

[108] Sánchez-de Armas, R.; San-Miguel, M. A.; Oviedo, J.; Marquez, A.; Sanz, J. F., *Phys. Chem. Chem. Phys.* **2011**, *13*, 1506.

[109] Li, W.; Doblinger, M.; Vaneski, A.; Rogach, A. L.; Jackel, F.; Feldmann, J., *J. Mater. Chem.* **2011**, *21*, 17946.

[110] Puthussery, J.; Seefeld, S.; Berry, N.; Gibbs, M.; Law, M., *J. Am. Chem. Soc.* **2011**, *133*, 716.

[111] Ennaoui, A.; Fiechter, S.; Jaegermann, W.; Tributsch, H., *J. Electrochem. Soc.* **1986**, *133*, 97.

[112] Steinhagen, C.; Harvey, T. B.; Stolle, C. J.; Harris, J.; Korgel, B. A., *J. Phys. Chem. Lett.* **2012**, *3*, 2352.

[113] Birkholz, M.; Fiechter, S.; Hartmann, A.; Tributsch, H., *Phys. Rev. B* **1991**, *43*, 11926.

[114] Yu, L.; Lany, S.; Kykyneshi, R.; Jieratum, V.; Ravichandran, R.; Pelatt, B.; Altschul, E.; Platt, H. A. S.; Wager, J. F.; Keszler, D. A.; Zunger, A., *Adv. Energy Mater.* **2011**, *1*, 748.

[115] Kirkeminde, A.; Ruzicka, B. A.; Wang, R.; Puna, S.; Zhao, H.; Ren, S., *ACS Appl. Mater. Interfaces* **2012**, *4*, 1174.

[116] Wang, D.; Wang, Q.; Wang, T., *CrystEngComm* **2010**, *12*, 3797.

[117] Wang, D.-W.; Wang, Q.-H.; Wang, T.-M., *CrystEngComm* **2010**, *12*, 755.

[118] Zhu, L.; Richardson, B.; Tanumihardja, J.; Yu, Q., *CrystEngComm* **2012**, *14*, 4188.

[119] Alfonso, D. R., *J. Phys. Chem. C* **2010**, *114*, 8971.

2

Methodology

Density functional theory is the workinghorse of most of today's available quantum chemistry codes. The first attempts to use electron density to calculate electronic properties of molecules were made in the 1920s, but it took several decades until Hohenberg and Kohn laid the foundations for modern density functional theory. Based on this theory, extensions were introduced, one of them being the time-dependent density functional theory that enables the calculation of excited states, a domain that was reserved for much costlier methods like configurational interaction, coupled cluster, and the like.

2.1 Introduction

The mathematical machinery of quantum mechanics enables computational chemists and physicists to investigate matter on a microscopic level, provinding insights that are inaccessible to experimentalists. Many problems have been resolved thanks to quantum mechanics. Over the years, two approaches have enjoyed high popularity amongst the community of computational scientists, these are the wave function (WF) based methods, and density functional theory (DFT). There exist several well-written textbooks about this subject, for instance, by Koch and Holthausen [1] or Szabo and Ostlund [2]. Part of what follows is based on these excellent books.

Around these methodologies, tools were and are developed to obtain information about systems and models in order to get an ever more detailed oversight of their properties. As we are interested in optical properties, we need access to the electronic structure of a model, which we can readily calculate using standard DFT techniques. Then, the principle to distort the electron density and observe the dynamics of the relaxation of the excited electron cloud yields optical information about the system of interest. Such real time methodologies offer a relatively cheap procedure to obtain these optical properties, however, at the cost of losing some information that other methods can give to the researcher.

Both WF and DFT are based on the Schrödinger equation, whose solution, at least in an approximate form, is the ultimate goal. In this approximate form it reduces to the time-independent and non-relativistic Schrödinger equations

$$\hat{\mathrm{H}}\Psi = E\Psi \tag{2.1}$$

where $\hat{\mathrm{H}}$ is the Hamiltonian operator for a molecular system that consists of M nuclei and N electrons. No magnetic or electric fields are applied. The Hamiltonian operator represents the total energy of a given molecular system:

$$\begin{aligned}\hat{\mathrm{H}} &= \hat{\mathrm{T}}_\mathrm{e} + \hat{\mathrm{T}}_\mathrm{N} + \hat{\mathrm{V}}_\mathrm{Ne} + \hat{\mathrm{V}}_\mathrm{ee} + \hat{\mathrm{V}}_\mathrm{NN} \\ &= -\frac{1}{2}\sum_{\mathrm{i}=1}^{\mathrm{N}} \nabla_\mathrm{i}^2 - \frac{1}{2}\sum_{\mathrm{A}=1}^{\mathrm{M}} \frac{1}{M_\mathrm{A}} \nabla_\mathrm{A}^2 - \sum_{\mathrm{i}=1}^{\mathrm{N}}\sum_{\mathrm{A}=1}^{\mathrm{M}} \frac{Z_\mathrm{A}}{\mathbf{r}_\mathrm{iA}} \\ &\quad + \sum_{\mathrm{i}=1}^{\mathrm{N}}\sum_{\mathrm{j}>\mathrm{i}}^{\mathrm{N}} \frac{1}{\mathbf{r}_\mathrm{ij}} + \sum_{\mathrm{A}=1}^{\mathrm{M}}\sum_{\mathrm{B}>\mathrm{A}}^{\mathrm{M}} \frac{Z_\mathrm{A} Z_\mathrm{B}}{\mathbf{R}_\mathrm{AB}}\,. \end{aligned} \tag{2.2}$$

A and B run over the nuclei M, i and j over the electrons N. $\hat{T}_e$ and $\hat{T}_n$ refer to the kinetic energy of the electrons and the nuclei, respectively. The Laplacian operator ∇_q^2 in these terms is defined as a sum of differential operators in Cartesian coordinates;

$$\nabla_q^2 = \frac{\partial^2}{\partial x_q^2} + \frac{\partial^2}{\partial y_q^2} + \frac{\partial^2}{\partial z_q^2} \tag{2.3}$$

and M_A is the mass of nucleus A.

This form of the Schrödinger equation can still be simplified by fixing the nuclear positions. The reasoning behind this approximation is that the electron's weight is just a few of a ten thousand's of a part of the weight of a nucleus. As a consequence, they move much faster than the nucleus, and the latter can be assumed to be static. Consequently, the kinetic energy of the nuclei is zero, and the potential energy becomes a constant. The electronic part is described by the electronic Hamiltonian:

$$\hat{H}_{elec} = \hat{T} + \hat{V}_{Ne} + \hat{V}_{ee}\,. \tag{2.4}$$

This results in the total energy being the sum of E_{elec} and the potential energy of the nuclei

$$\hat{H}_{elec}\Psi_{elec} = E_{elec}\Psi_{elec} \tag{2.5}$$

$$E_{tot} = E_{elec} + E_{nuc}\,. \tag{2.6}$$

This approximation is called the Born-Oppenheimer approximation, and what follows will be based on it. To simplify the notation, the subscript "elec" and the nuclear component are dropped.

The wave function Ψ itself is not observable. However, the square of the wave function can be associated with a physical interpretation in that

$$|\Psi(\mathbf{x}_1, \mathbf{x}_2, \ldots, \mathbf{x}_N)|^2 d\mathbf{x}_1 d\mathbf{x}_2 \ldots d\mathbf{x}_N \tag{2.7}$$

represents the probability that electrons 1, 2, ..., N are found at the same time in volume elements $d\mathbf{x}_1 d\mathbf{x}_2 ... d\mathbf{x}_N$. It must be the same if any two electrons are exchanged, since electrons are indistinguishable. However, because electrons have spin = $\frac{1}{2}$ the exchange of two electrons leads to the antisymmetric principle where

$$\Psi(\mathbf{x}_1, \mathbf{x}_2, \ldots, \mathbf{x}_i, \mathbf{x}_j, \ldots, \mathbf{x}_N) = -\Psi(\mathbf{x}_1, \mathbf{x}_2, \ldots, \mathbf{x}_j, \mathbf{x}_i, \ldots, \mathbf{x}_N)\,. \tag{2.8}$$

Finally, the integral of Equation (2.7) over the full range of variables must be one, i.e., the probability of finding an electron N at any given point in space is unity,

$$\int \dots \int |\Psi(\mathbf{x}_1, \mathbf{x}_2, \dots, \mathbf{x}_N)|^2 \, d\mathbf{x}_1 d\mathbf{x}_2 \dots d\mathbf{x}_N = 1 \,, \tag{2.9}$$

therefore, such a wave function is normalized.

2.2 Density functional theory

The foundations of density functional theory lie in the 1920s, when Thomas and Fermi founded the first basic principles of DFT by approximately calculating the total electronic energy using the electron density only, which is called the Thomas-Fermi model [3, 4]. The real breakthrough came 40 years later when Hohenberg and Kohn developed several basic theorems [5]. They realized that the electron density uniquely defines the ground-state energy of a system and, hence, this formalism is orbital-free. It is a variational approach; the density that minimizes the total energy is the ground-state density. A functional form for the energy was introduced where it depends on the electron density function as it is shown as follows:

$$E\left[\rho(\mathbf{r})\right] = \int V_{\text{ext}}(\mathbf{r})\rho(\mathbf{r})d\mathbf{r} + F\left[\rho(\mathbf{r})\right] . \tag{2.10}$$

The first term describes the Coulomb interactions of the electrons with the nucleus and is assigned as the external potential. $F\left[\rho(\mathbf{r})\right]$ is an unknown but universal functional of the electron density and is composed by the kinetic energy $\mathrm{T}\left[\rho(\mathbf{r})\right]$ and the inter-electronic potential $V_{\text{ee}}\left[\rho(\mathbf{r})\right]$. Kohn and Sham suggested using the expression for the exact kinetic energy of a non-interacting system

$$T_{\text{S}} = -\frac{1}{2}\sum_{\text{i}}^{\text{N}} \langle \varphi_{\text{i}} | \nabla^2 | \varphi_{\text{i}} \rangle . \tag{2.11}$$

Indeed, the kinetic energies of interacting and non-interacting systems are not the same. Therefore, Kohn and Sham introduced the following separation of $F\left[\rho(\mathbf{r})\right]$:

$$F\left[\rho(\mathbf{r})\right] = T_{\text{S}}\left[\rho(\mathbf{r})\right] + J\left[\rho(\mathbf{r})\right] + E_{\text{xc}}\left[\rho(\mathbf{r})\right] , \tag{2.12}$$

where E_{xc} is the exchange-correlation energy, which is defined as

$$\begin{aligned} E_{xc}[\rho] &\equiv (T[\rho] - T_S[\rho]) + (E_{ee}[\rho] - J[\rho]) \\ &= T_c[\rho] + E_{nucl}[\rho]\,. \end{aligned} \tag{2.13}$$

The exchange-correlation functional E_{xc} can be imagined as some kind of scrap yard; it contains everything that is unknown. The remaining question is how V_S be defined in order to provide the Slater determinant whose density resembles the real system? It helps to write down the energy of the real, interacting system:

$$\begin{aligned} E[\rho(\mathbf{r})] &= T_S[\rho] + J[\rho] + E_{xc}[\rho] + E_{Ne}[\rho] \\ &= T_S[\rho] + \frac{1}{2}\int\int \frac{\rho(\mathbf{r}_1)\rho(\mathbf{r}_2)}{\mathbf{r}_{12}} d\mathbf{r}_1 d\mathbf{r}_2 \\ &\quad + E_{xc}[\rho] + \int V_{Ne}\rho(\mathbf{r}) d\mathbf{r} \\ &= -\frac{1}{2}\sum_i^N \langle\varphi_i|\nabla^2|\varphi_i\rangle \\ &\quad + \frac{1}{2}\sum_i^N\sum_j^N \int\int |\varphi_i(\mathbf{r}_1)|^2 \frac{1}{\mathbf{r}_{12}} |\varphi_j(\mathbf{r}_2)|^2 d\mathbf{r}_1 d\mathbf{r}_2 \\ &\quad + E_{xc}[\rho(\mathbf{r})] - \sum_i^N \int \sum_A^M \frac{Z_A}{\mathbf{r}_{1A}} |\varphi_i(\mathbf{r}_1)|^2 d\mathbf{r}_1\,. \end{aligned} \tag{2.14}$$

In Equation (2.14), E_{xc} is not known. Finally, it is necessary to find out the conditions under which the orbitals φ_i minimize the energy expression under the constraint $\langle\varphi_i|\varphi_j\rangle = \delta_{ij}$. This leads to the equation as derived in Reference [6]

$$\left[-\frac{1}{2}\nabla^2 + V_{eff}\mathbf{r}_1\right]\varphi_j = \varepsilon_i\varphi_i\,. \tag{2.15}$$

The Kohn-Sham effective potential is obtained by

$$V_{eff}(\mathbf{r}) = \int \frac{\rho(\mathbf{r}_2)}{\mathbf{r}_{12}} d\mathbf{r}_2 + V_{xc}\mathbf{r}_1 - \sum_A^M \frac{Z_A}{\mathbf{r}_{1A}}\,. \tag{2.16}$$

The V_{eff} term already depends on the density, and, thus, on the orbitals, through the Coulomb term J[ρ] in Equation (2.14). It remains to state that the Kohn-Sham one-electron Equation (2.15) need to be solved by iteration.

2.2.1 Exchange-correlation functionals

Nowadays there are several functionals that derive $E_{xc}[\rho(\mathbf{r})]$ in an effective way. The simplest functional is the local density approximation (LDA) which Hohenberg and Kohn proposed in their original paper [5]. It is based upon the assumption that the electron density is constant at each point in space, which is designated by the term "homogeneous electron gas". Within this approximation the total exchange-correlation energy is

$$E_{xc}^{LDA}[\rho(\mathbf{r})] = \int \rho(\mathbf{r})\varepsilon_{xc}^{LDA}(\rho(\mathbf{r}))\,d\mathbf{r}, \tag{2.17}$$

where $\varepsilon_{XC}(\rho(\mathbf{r}))$ is the exchange-correlation energy per electron in the homogeneous electron gas. The LDA is a fairly popular functional because it gives relatively good structural and vibrational properties, even for systems with large density gradients. The popularity of DFT is related to the LDA. Only the strong tendency of the LDA to give strongly energetic over-binding in molecules makes this approximation unfavorable in certain cases.

Because of this limitation, gradient corrected functionals were introduced, which not only depend on the value of the density but also on the density gradient at each point in space. The generalized gradient correction approximation (GGA) introduces the density gradient as the only new variable [7–10]. The exchange-correlation energy for an electron is now given by

$$E_{xc}^{GGA}[\rho(\mathbf{r})] = \int \varepsilon_{xc}^{GGA}(\rho(\mathbf{r}), \nabla\rho(\mathbf{r}))d\mathbf{r}. \tag{2.18}$$

Such functionals consist of an exchange and a correlation part, for which the expression for the energy can be written as

$$E_{xc}^{GGA} = E_{x}^{GGA} + E_{c}^{GGA}. \tag{2.19}$$

One of the most popular functionals using the GGA form is the PBE functional [11]. Here, the parameters are fundamental constants and the functional has a relatively simple form and derivation. Another GGA functional that enjoys widespread application is the BLYP exchange-correlation functional [12, 13].

The main drawback of the GGA functionals is that they cannot reproduce correctly the exchange effects. This flaw can be circumvented by introducing the exact exchange energy as it is calculated with Hartree-Fock theory, where

the exact exchange energy can be obtained by computing the Slater determinant. We obtain, thereby, the so-called hybrid functionals. With this exact energy we now get for the exchange-correlation energy

$$E_{\mathrm{xc}} = E_{\mathrm{x}}^{\mathrm{exact}} + E_{\mathrm{c}}^{\mathrm{KS}}\,. \tag{2.20}$$

where $E_{\mathrm{c}}^{\mathrm{KS}}$ is the Kohn-Sham correlation energy. A very popular hybrid functional is the B3LYP [13, 14] functional. The correlation part is the same as in the BLYP, and the exchange functional, as proposed by Becke, introduces three semiempirical parameters. They were chosen as such that atomization and ionization energies, and proton affinities included in the G2 data base, were well reproduced. The parametrization leads to very good results for mostly organic molecules, but this hybrid functional fails when it comes to solid state chemistry.

Perdew, Ernzerhof, and Burke proposed a hybrid functional that is completely parameter-free. The resulting PBE0, or sometimes called PBE1PBE, functional [15–18] contains 25 % of the exact exchange, which has been obtained from a theoretical point of view:

$$E_{\mathrm{xc}}^{\mathrm{hybrid}} = E_{\mathrm{xc}}^{\mathrm{GGA}} + 0.25(E_{\mathrm{x}}^{\mathrm{HF}} - E_{\mathrm{x}}^{\mathrm{GGA}})\,. \tag{2.21}$$

Although parameter-free, this hybrid functional does come with flaws. For instance, it is well-known that it overestimates the band gap of semiconducting materials consistently.

So far, we assumed closed-shell systems. Consequently, it is not necessary to consider the spin of the electrons. However, in cases where the system has electrons with different spins α and β, it is necessary to consider the different electron spins. The exchange-correlation energy in this so-called local-spin density approximation (LSD) differs in that now two densities are considered, one for spin α and one for spin β:

$$E_{\mathrm{xc}}^{\mathrm{LSD}}\left[\rho_\alpha, \rho_\beta\right] = \int \rho(\mathbf{r})\varepsilon_{\mathrm{xc}}(\rho_\alpha(\mathbf{r}), \rho_\beta(\mathbf{r}))\mathrm{d}\mathbf{r}\,. \tag{2.22}$$

2.3 DFT+U

A problem of standard LDA functionals is that the localization of electrons is not well described. Electrons such as d- and f-electrons are delocalized over

the whole system when, for instance, only an LDA functional only is applied. However, the nature of these electrons is localized, and it might be that, with LDA, a semiconductor or even insulator would be described as conductor.

To circumvent such wrong descriptions, localized d- and f-electrons are separately treated from delocalized s- and p-electrons. An on-site Hubbard-like interaction E_{Hub} corrects the standard functional [19–21]:

$$E_{\mathrm{LSDA+U}}\left[\rho(\mathbf{r})\right] = E_{\mathrm{LSDA}}\left[\rho(\mathbf{r})\right] + E_{\mathrm{Hub}}\left[\left\{n_{\mathrm{i}}^{\sigma}\right\}\right] - E_{\mathrm{DC}}\left[\left\{n_{\mathrm{i}}^{\sigma}\right\}\right], \tag{2.23}$$

where $\rho(\mathbf{r})$ is the electronic density, and n_{i}^{σ} are the atomic-orbital occupations for atom i with spin σ that experiences the Hubbard term. The last term is added to avoid double counting of interactions contained in E_{Hub} and in E_{LSDA}. It can be described as

$$E_{\mathrm{DC}}\left[\{n_{\mathrm{i}}\}\right] = \sum_{\mathrm{i}} \frac{U}{2} n_{\mathrm{i}}\left(n_{\mathrm{i}} - 1\right) - \sum_{\mathrm{i}} \frac{J}{2}\left[n_{\mathrm{i}}^{\alpha}\left(n_{\mathrm{i}}^{\alpha} - 1\right) + n_{\mathrm{i}}^{\beta}\left(n_{\mathrm{i}}^{\beta} - 1\right)\right], \tag{2.24}$$

where $n_{\mathrm{i}} = n_{\mathrm{i}}^{\alpha} + n_{\mathrm{i}}^{\beta}$, and $n_{\mathrm{i}}^{\sigma} = \mathrm{Tr}\left[\mathbf{n}_{\mathrm{i}}^{\sigma}\left(1 - \mathbf{n}_{\mathrm{i}}^{\sigma}\right)\right]$, and U and J are the screened on-site Coulomb and exchange parameters, respectively. For the case, where exchange and non-sphericity are neglected, $E_{\mathrm{LSDA+U}}$ becomes

$$E_{\mathrm{LSDA+U}} = E_{\mathrm{LSDA}} + \frac{U}{2}\sum_{\mathrm{i}\neq\mathrm{j}} n_{\mathrm{i}} n_{\mathrm{j}} - \frac{U}{2} n_{\mathrm{i}}\left(n_{\mathrm{i}} - 1\right). \tag{2.25}$$

Within the present work, the rotationally invariant formalism introduced by Dudarev *et al.* as it was implemented in CP2K has been applied [22, 23]. In this methodology, the parameters U and J are combined into an effective U parameter, which is defined as $U_{\mathrm{eff}} = U - J$. Orbitals are shifted by $\frac{U_{\mathrm{eff}}}{2}$, depending on their occupancy.

2.4 Time-dependent density functional theory

Time-dependent density functional theory (TDDFT) [24–26] has made its way into almost every major computational chemistry code available. It enables one to calculate excitation energies with good accuracy for relatively low computational costs.

2.4.1 Linear-response time-dependent DFT

The frequency dependent linear response of a finite system with respect to a time-dependent perturbation yields the frequency dependent mean polarizability $\alpha(\omega)$. The mean polarizability describes how the dipole moment responds to an external time-dependent electric field with frequency $\omega(t)$:

$$\alpha(\omega) = \sum_{\mathrm{i}} \frac{f_{\mathrm{i}}}{\omega_{\mathrm{i}}^2 - \omega^2}\,, \tag{2.26}$$

where ω_{i} is the excitation energy $E_{\mathrm{i}} - E_0$, and i refers to all excited states of the system. Obviously, if the difference $\omega_{\mathrm{i}}^2 - \omega^2$ is very small then the mean polarizability shows a response to the given excitation energy. $\mathrm{f_i}$ are the oscillator strengths [27–31].

2.4.2 Real-time time-dependent DFT

Apart from the frequency-dependent TDDFT, there exists also a methodology to calculate optical properties of a system via a time-dependent method, the so-called real-time TDDFT (RT-TDDFT). The basic idea of RT-TDDFT is to apply an external, time-dependent electric field to a system in its ground state. This electric field is applied along axis i, and the perturbation will induce a dipole moment μ along axis j [32]:

$$\mu_{\mathrm{j}} = \mu_{\mathrm{j0}} + \alpha_{\mathrm{ij}} E_{\mathrm{i}}\,, \tag{2.27}$$

where μ_{j0} is the permanent dipole moment and α_{ij} is the linear polarizability tensor. The equation (2.27) can be written in the time domain as

$$\mu_{\mathrm{j}} = \mu_{\mathrm{j0}} + \int \mathrm{d}t_1\, \alpha_{\mathrm{ij}}(t - t_1) E_{\mathrm{i}}(t_1)\,. \tag{2.28}$$

In order to relate $\alpha_{\mathrm{ij}}(t - t_1)$ to the frequency domain polarizability the following is applied:

$$\alpha_{\mathrm{ij}}(t - t_1) = \int \frac{\mathrm{d}\omega}{2\pi} \mathrm{e}^{-i\omega(t-t_1)} \alpha_{\mathrm{ij}}(\omega)\,. \tag{2.29}$$

The next step is to combine Equations (2.28) and (2.29)

$$\begin{aligned} \mu_{\mathrm{j}} &= \mu_{\mathrm{j0}} + \int \mathrm{d}t_1 \int \frac{\mathrm{d}\omega}{2\pi} \mathrm{e}^{-i\omega(t-t_1)} \alpha_{\mathrm{ij}}(\omega) E_{\mathrm{i}}(t_1) \\ &= \mu_{\mathrm{j0}} + \int \frac{\mathrm{d}\omega}{2\pi} \mathrm{e}^{-i\omega t} \alpha_{\mathrm{ij}}(\omega) E_{\mathrm{i}}(\omega)\,. \end{aligned} \tag{2.30}$$

Now, as the induced dipole is defined as

$$\mu_{\mathrm{j}}^{1}(t) = \mu_{\mathrm{j}} - \mu_{\mathrm{j0}} \tag{2.31}$$

the formulation of it in the frequency domain is

$$\mu_{\mathrm{j}}^{1}(\omega) = \alpha_{\mathrm{ij}}(\omega) E_{\mathrm{i}}(\omega)\,. \tag{2.32}$$

Solving Equation (2.32) for $\alpha_{\mathrm{ij}}(\omega)$ yields

$$\alpha_{\mathrm{ij}}(\omega) = \frac{\mu_{\mathrm{j}}^{1}(\omega)}{E_{\mathrm{i}}(\omega)} = \frac{\int \mathrm{d}t \mathrm{e}^{i\omega t} \mu_{\mathrm{j}}^{1}(t)}{\int \mathrm{d}t \mathrm{e}^{i\omega t} E_{\mathrm{i}}(t)}\,. \tag{2.33}$$

This equation relates the frequency-dependent polarizability tensor, $\alpha_{\mathrm{ij}}(\omega)$, to the evolution of the induced dipole, $\mu_{\mathrm{j}}^{1}(t)$, and the external electric field, $E_{\mathrm{i}}(t)$. The theoretical framework to calculate $\alpha_{\mathrm{ij}}(\omega)$ has been setup, but it needs to be plugged-in to DFT.

When a system is perturbed by an external field, $\mathbf{E}_0(t)$, then $\mu(t)$ is calculated from the perturbed electron density by using the time-dependent Schrödinger equation (TDSE) [33]:

$$i\frac{\partial}{\partial t}\varphi(\mathbf{r},t) = \left[-\frac{1}{2}\nabla^2 + \int \mathrm{d}\mathbf{r}_2 \frac{\rho(\mathbf{r}_2,t)}{\mathbf{r}_{12}} + \frac{\partial E_{\mathrm{xc}}(\rho(\mathbf{r},t))}{\partial \rho(\mathbf{r},t)} - \mathbf{E}_0 \cdot \mathbf{r}\right] \varphi(\mathbf{r},t)\,. \tag{2.34}$$

The terms on the right side of Equation (2.34) correspond to the kinetic energy, T_{S}, the Coulomb energy, J, the exchange-correlation energy, E_{xc}, and the external electric field, $\mathbf{E}_0$. The Hamiltonian that couples the electric field and the dipole moment is given by

$$-\int \varphi^*(\mathbf{r})\,\mathbf{E}_0 \cdot \mathbf{r}\,\varphi(\mathbf{r})\mathrm{d}\mathbf{r} = -\mathbf{E}_0 \cdot \int \varphi^*(\mathbf{r})\,\mathbf{r}\,\varphi(\mathbf{r}) = -\mathbf{E}_0 \cdot \mathbf{P}\,, \tag{2.35}$$

where φ^* is the complex conjugate.

Based on this derivation the absorption cross section $\sigma(\omega)$ is obtained [34]

$$\sigma(\omega) = \frac{4\pi\omega}{c}\left\langle \frac{1}{3}\Big(\alpha_{\mathrm{ii}}(\omega) + \alpha_{\mathrm{jj}}(\omega) + \alpha_{\mathrm{kk}}(\omega)\Big)\right\rangle_{\mathrm{imag}}\,. \tag{2.36}$$

Here, c is the speed of light, and the imaginary part is needed to calculate the cross section, indicated by $\langle\,\rangle_{\mathrm{imag}}$. Chen *et al.* further develop the method to get

the Raman differential cross section for a given vibration normal mode [32, 35], which is not described here as we make no use of it.

Unfortunately, the time-dependent Schrödinger equation cannot be solved analytically. There are, however, methods available that can circumvent this flaw by propagation. Several methodologies exist that propagate the TDSE, one of them being the Crank–Nicholson (CN) approximation [36], also known as the implicit midpoint rule:

$$i\frac{\varphi_{n+1}-\varphi_n}{\Delta t} = \hat{H}(t_{n+1/2})\frac{1}{2}(\varphi_{n+1}-\varphi_n), \tag{2.37}$$

where $t_{n+1/2} = \frac{1}{2}(t_{n+1}+t_n)$ and $t_n = n\Delta t$. The implicit midpoint rule possesses the useful property that it is time-reversible. The problem of the CN method is that it depends on, inter alia, the maximum of the norm of the third time derivative of the solution φ on the time interval under consideration [37]. As a consequence, the initial data needs to be, spatially, very smooth, otherwise the wave function $\varphi(t)$ is highly oscillatory in time, and, because of that, higher derivatives can become large. If accuracy is crucial, then very small time steps are needed. This is why, in studies of optical absorption spectra where the CN method has been applied, time steps in the attosecond range are employed.

If the wave function is propagated backwards by $\Delta t/2$ starting from $\varphi(t+\Delta t)$ or if it is propagated forwards by $\Delta t/2$ but starting from $\varphi(t)$ then the result should be the same for a time-reversible method. This statement leads to the enforced time reversible symmetry (ETRS) algorithm published by Castro *et al.* [38]. The propagator in the ETRS scheme becomes

$$\hat{U}_{ETRS}(t+\Delta t, t) = \exp\left\{-i\frac{\Delta t}{2}\hat{H}(t+\Delta t)\right\} \times \exp\left\{-i\frac{\Delta t}{2}\hat{H}(t)\right\}. \tag{2.38}$$

This kind of propagator allows for time steps in the femtosecond range, while offering good accuracy.

2.4.2.1 RT-TDDFT for periodic systems

The RT-TDDFT method, as it is described in the preceding section, can only be used for non-periodic systems. Bulk systems, slab surfaces, or nanotubes, for example, cannot be investigated by that method. In a periodic system, the excited electron density will propagate into the neighboring cell and the calculation of the dipole moment is not trivial anymore.

In 1956, Pancharatnam published a work where he determined the phase change of polarized light after it passes through a sequence of polarizers. After passing through these polarizers, the final polarization of the light is, again, the same as the initial polarization. To do so he defined phase differences between two different polarization states. Therefore, he considered discrete phases, rather than continuous phases, as they are usually addressed [40]. The interested reader may have a look at the review by Resta [41] and the therein cited references for more detailed information and derivation of the methodology on which periodic RT-TDDFT is based upon.

2.5 Density derived atomic point charges

A different property that we will present in this work is the charge localized on an atom. There exist several methods to calculate the point charge of a given atom from the quantum mechanical charge distribution using charge density partition schemes [42–45]. A more recent method introduced by Blöchl takes a different approach. He expanded the density into atom-centered Gaussians, whose superposition should reproduce the density near the origin of reciprocal space and its multipole moments [46]. Then, the Gaussians can be replaced by point charges. This procedure avoids the usage of multipoles. This is beneficial since the number of multipoles increases with the system size. Furthermore, the choice of origin for a multipole expansion is non-trivial in periodic systems. Thus, the method is called density derived atomic point charges (DDAPC).

The difficulty of the DDAPC lies in that the charges need to be decoupled, which is resolved by choosing a suitable model density in terms of superimposed Gaussians. Further, this density needs to be obtained. Also, the potential that acts on the electrons and the forces that act on the nuclei need to be corrected. The details about how the DDAP charges are calculated are given in Reference [46]; here we give just a short overview.

A general model density $\hat{n}_\mathrm{V}$ can be represented as

$$\hat{n}_\mathrm{V}(\mathbf{r}) = \sum_\mathrm{i} q_\mathrm{i} g_\mathrm{i}(\mathbf{r}) \,, \tag{2.39}$$

where $g_\mathrm{i}(\mathbf{r})$ are atom-centered Gaussians, which themselves are normalized as

such that they have a charge of one:

$$g_{\mathrm{i}}(\mathbf{r}) = \frac{1}{\left(\sqrt{\pi} r_{\mathrm{c,i}}\right)^3} \exp\left\{-\left(\frac{\mathbf{r}-\mathbf{R}_{\mathrm{i}}}{r_{\mathrm{c,i}}}\right)^2\right\}, \tag{2.40}$$

where $\mathbf{R}$ denotes a particular atomic site. i refers to the atomic sites which can be the center of several Gaussians. Finally, r_{c} are the decay lengths of the Gaussians. The number of Gaussians and the decay lengths are those variables that will determine the results of the calculation. In this work, we will use 4 Gaussians on each atomic site and the default plane wave cutoff of $G_{\mathrm{c}}^2/2 = 3$ Ry was chosen. The decay lengths for the Gaussians differ to the next by a factor of 1.65. The smallest radius for a Gaussian is at least 0.265 Å.

2.6 CP2K

The CP2K/QUICKSTEP program is a general purpose and highly efficient quantum chemistry code. It uses a hybrid Gaussian and plane wave basis set based on DFT [47, 48]. The interactions between the atomic core and the valence electrons are described using dual-space Goedecker–Teter–Hutter (GTH) pseudopotentials [49–51]. Molecularly optimized double-ζ single-polarized basis sets (m-DZVP) are used [52] for all elements included in the calculations. For semiconductors, the short-range form of these basis sets are employed (m-DZVP-SR). This applies also to O and S atoms that form part of these semiconductors. The plane wave cutoff for the expansion of the density is set to at least 600 Ry. CP2K has no $\mathbf{k}$-points implemented, therefore, the Brillouin zone is sampled only at the $\mathbf{\Gamma}$-point. The atomic cores of the elements Ti and Fe are described by small-size core pseudopotentials. Therefore, for Ti a potential with 12 explicit valence electrons is used, while for Fe the number of explicit valence electrons increases to 16. For O and S, 6 valence electrons are included, for N and P, 5 valence electrons are assumed, and for C and H, 5 and 1, respectively. For geometry optimizations, the forces are converged until they are smaller than 0.1 eV/Å. The epsilon down to which the wave function is converged was set to $\epsilon = 10^{-7}$.

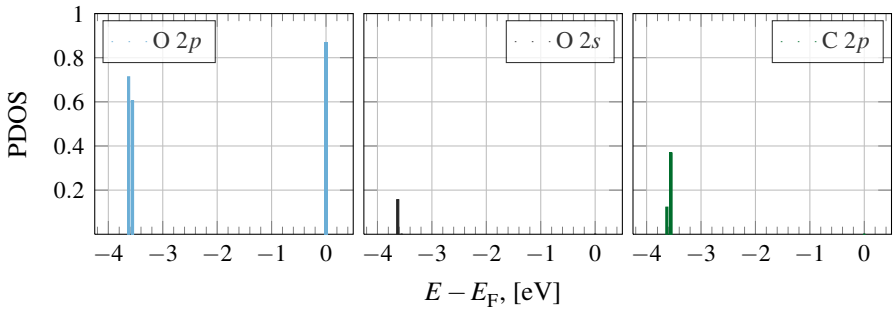

FIG. 2.1 Partial density of states for the HOMO-2, HOMO-1, and the HOMO. Shown are the O $2s$ and $2p$, and the C $2p$ atomic orbitals. C $2s$ orbitals are not included because they do not contribute to these MOs.

2.6.1 Partial density of states

The density of states as we use them in this thesis need some explanation in order to correctly interpret the graphs that will be included throughout the thesis. In CP2K, the density of states (DOS) is calculated at discrete levels of energy, they are not described as continuous bands as other codes do. Each level corresponds to a molecular orbital (MO) that is formed by the atomic orbitals of the atom species contained in the model system. This is illustrated in Fig. 2.1 with the CO_2 molecule. Shown is an energy range within which the HOMO-2, the HOMO-1, and the HOMO are included. The HOMO is formed by two-fold degenerate MOs to which almost exclusively the oxygen's $2p$ orbitals contribute. Its height is about 0.87. The remaining 0.13 that are needed to reach 1 are contributed by the carbon's $3d$ orbitals. The situation is similar for the HOMO-1, which is also two-fold degenerated. It is formed to the largest parts by the C $2p$ and the O $2p$ orbitals, which contribute 0.38 and 0.6, respectively, to the MOs. Finally, the HOMO-2 is formed by three atomic orbitals: O $2s$ and $2p$, as well as the C $2p$. Therefore, this kind of representation of MOs is a partial density of states (PDOS). This MO-type representation of the DOS is closer to the representation of the DOS of molecules, and since the QDs that are investigated in this work are not periodic systems, the PDOS does represent well these cluster systems.

One consequence is that the contribution to the PDOS from a given set of atomic orbitals, for example the Se $4p$ orbitals of the bare $(CdSe)_{13}$ cluster, is

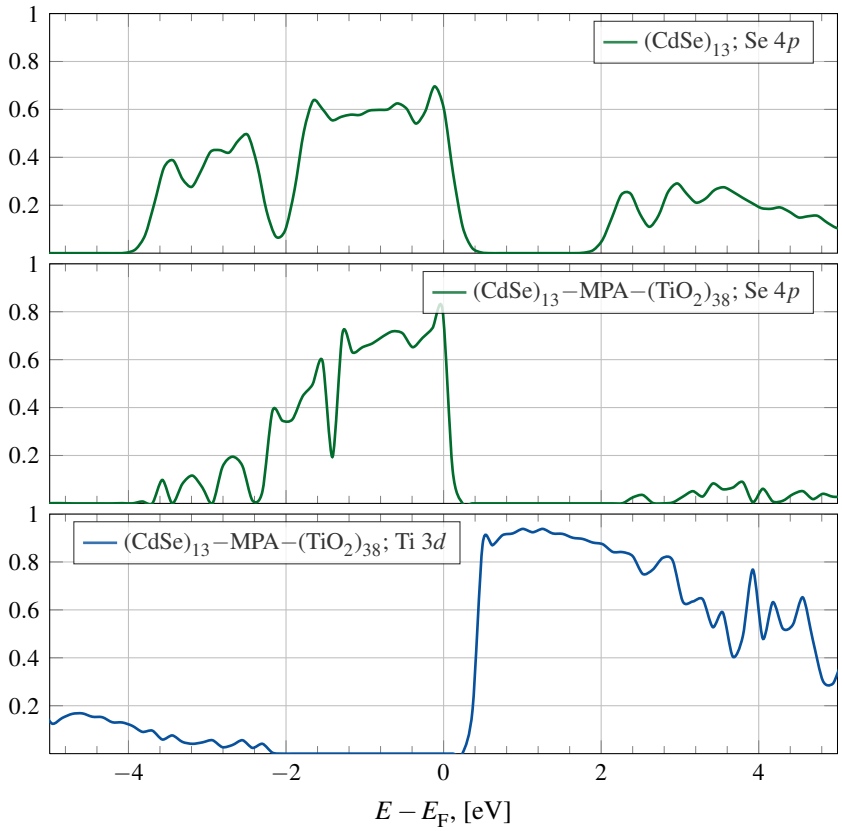

FIG. 2.2 What it means is given in the text.

different when the PDOS is calculated for the isolated cluster, or if it is linked to a TiO_2 nanoparticle. However, this is only the case in the energy ranges where TiO_2 does not contribute to the MOs. Fig. 2.2 does illustrate this effect. The Se $4p$ PDOS of bare $(CdSe)_{13}$ is shown in the top panel, and in the second panel is the equivalent PDOS but for the $(CdSe)_{13}$−MPA−$(TiO_2)_{38}$ system. One can easily observe that above 2eV the height of the PDOS in the middle panel is obviously lower than in the top panel, although the number of Se atoms is the same. At these energies, the Ti $3d$ orbitals do also contribute to the MOs, consequently, the relative weight of the Se $4p$ orbitals within these MOs becomes smaller. Between -2 and 0 eV they are similar in height because there TiO_2 does not contribute any significant part to the MO.

The PDOS in Fig. 2.2 are fitted with Gaussian functions with a σ of 0.1 eV in order to obtain nice plots of the PDOS. This leads to band edges that do overlap into energy regions that actually are empty. Therefore, the graphically observed band gaps will always be smaller than those that are calculated as the difference between HOMO and LUMO. These band gaps are the correct ones and will be tabulated throughout the thesis.

2.7 Bibliography

[1] Koch, W.; Holthausen, M. C., *A Chemist's Guide to Density Functional Theory*, Wiley-VCH, Weinheim **2001**.

[2] Szabo, A.; Ostlund, N. S., *Modern Quantum Chemistry*, Dover Publications, Inc., Mineola, New York **1996**.

[3] Fermi, E., *Rend. Accad. Lincei* **1927**, *6*, 602.

[4] Thomas, L. H., *Math. Proc. Cambridge Philos. Soc.* **1927**, *23*, 542.

[5] Hohenberg, P.; Kohn, W., *Physical Review* **1964**, *136*.

[6] Parr, R. G.; Yang, W., *Density-Functional Theory of Atoms and Molecules*, Oxford University Press, New York **1989**.

[7] Langreth, D.; Perdew, J., *Phys. Rev. B* **1980**, *21*, 5469.

[8] Langreth, D.; Mehl, M., *Phys. Rev. B* **1983**, *28*, 1809.

[9] Perdew, J. P.; Yue, W., *Phys. Rev. B* **1986**, *33*, 8800.

[10] Perdew, J. P., *Phys. Rev. B* **1986**, *33*, 8822.

[11] Perdew, J.; Burke, K.; Ernzerhof, M., *Phys. Rev. Lett.* **1996**, *77*, 3865.

[12] Becke, A. D., *Phys. Rev. A* **1988**, *38*, 3098.

[13] Lee, C.; Yang, W.; Parr, R. G., *Phys. Rev. B* **1988**, *37*, 785.

[14] Becke, A. D., *J. Chem. Phys.* **1993**, *98*, 5648.

[15] Perdew, J. P.; Ernzerhof, M.; Burke, K., *J. Chem. Phys.* **1996**, *105*, 9982.

[16] Ernzerhof, M.; Perdew, J. P.; Burke, K., *Int. J. Quantum Chem.* **1997**, *64*, 285.

[17] Ernzerhof, M.; Scuseria, G. E., *J. Chem. Phys.* **1999**, *110*, 5029.

[18] Adamo, C.; Barone, V., *J. Chem. Phys.* **1999**, *110*, 6158.

[19] Anisimov, V. I.; Zaanen, J.; Andersen, O. K., *Phys. Rev. B* **1991**, *44*, 943.

[20] Anisimov, V. I.; Solovyev, I. V.; Korotin, M. A.; Czyżyk, M. T.; Sawatzky, G. A., *Phys. Rev. B* **1993**, *48*, 16929.

[21] Solovyev, I. V.; Dederichs, P. H.; Anisimov, V. I., *Phys. Rev. B* **1994**, *50*, 16861.

[22] Dudarev, S. L.; Manh, D. N.; Sutton, A. P., *Philos. Mag. B* **1997**, *75*, 613.

[23] Dudarev, S. L.; Botton, G. A.; Savrasov, S. Y.; Humphreys, C. J.; Sutton, A. P., *Phys. Rev. B* **1998**, *57*, 1505.

[24] Runge, E.; Gross, E. K. U., *Phys. Rev. Lett.* **1984**, *52*, 997.

[25] Gross, E. K. U.; Kohn, W., *Phys. Rev. Lett.* **1985**, *55*, 2850.

[26] Casida, M. E., in *Recent Advances in Computational Chemistry*, vol. Volume 1, pages 155–192, World Scientific **1995**.

[27] Gross, E. K. U.; Kohn, W., *Adv. Quantum Chem.* **1990**, *21*, 255.

[28] Bauernschmitt, R.; Ahlrichs, R., *Chemical Physics Letters* **1996**, *256*, 454.

[29] Casida, M. E.; Jamorski, C.; Casida, K. C.; Salahub, D. R., *J. Chem. Phys.* **1998**, *108*, 4439.

[30] Stratmann, R. E.; Scuseria, G. E.; Frisch, M. J., *J. Chem. Phys.* **1998**, *109*, 8218.

[31] Furche, F.; Ahlrichs, R., *J. Chem. Phys.* **2002**, *117*, 7433.

[32] Chen, H.; McMahon, J. M.; Ratner, M. A.; Schatz, G. C., *J. Phys. Chem. C* **2010**, *114*, 14384.

[33] Schrödinger, E., *Phys. Rev.* **1926**, *28*, 1049.

[34] Castro, A.; Appel, H.; Oliveira, M.; Rozzi, C. A.; Andrade, X.; Lorenzen, F.; Marques, M. A. L.; Gross, E. K. U.; Rubio, A., *Phys. Status Solidi B* **2006**, *243*, 2465.

[35] Neugebauer, J.; Reiher, M.; Kind, C.; Hess, B. A., *J. Comput. Chem.* **2002**, *23*, 895.

[36] Crank, J.; Nicolson, P., *Adv. Comput. Math.* **1996**, *6*, 207.

[37] Lubich, C., in J. Grotendorst; D. Marx; A. Muramatsu, editors, *Quantum Simulations of Complex Many-Body Systems: From Theory to Algorithms*, vol. 10, page 459, John von Neumann Institute for Computing, Jülich **2002**.

[38] Castro, A.; Marques, M. A. L.; Rubio, A., *J. Chem. Phys.* **2004**, *121*, 3425.

[39] Pancharatnam, S., *Proc. Indian Acad. Sci. A* **1956**, *44*, 247.

[40] Berry, M. V., *Proc. R. Soc. A* **1984**, *392*, 45.

[41] Resta, R., *J. Phys. Condens. Matter* **2000**, *12*, R107.

[42] Politzer, P.; Harris, R. R., *J. Am. Chem. Soc.* **1970**, *92*, 6451.

[43] Bader, R. F. W.; Beddall, P. M.; Cade, P. E., *J. Am. Chem. Soc.* **1971**, *93*, 3095.

[44] Hirshfeld, F. **1977**, *44*, 129.

[45] Mulliken, R. S., *J. Chem. Phys.* **1955**, *23*, 1833.

[46] Blöchl, P. E., *J. Chem. Phys.* **1995**, *103*, 7422.

[47] The CP2K Developers Group, http://www.cp2k.org **2000–2013**.

[48] VandeVondele, J.; Krack, M.; Mohamed, F.; Parrinello, M.; Chassaing, T.; Hutter, J., *Comput. Phys. Commun.* **2005**, *167*, 103.

[49] Goedecker, S.; Teter, M.; Hutter, J., *Phys. Rev. B* **1996**, *54*, 1703.

[50] Hartwigsen, C.; Goedecker, S.; Hutter, J., *Phys. Rev. B* **1998**, *58*, 3641.

[51] Krack, M., *Theor. Chem. Acc.* **2005**, *114*, 145.

[52] VandeVondele, J.; Hutter, J., *J. Chem. Phys.* **2007**, *127*, 114105.

3

CdSe

CdSe is a semiconductor material often used in quantum dot synthesis, which found its way into many applications like lasing, biosensing, photovoltaics, and LEDs. Since it is already a mature and well-known system, it may be used as a benchmark and test bed system for testing new methodologies, basis sets and functionals, or other technical issues. Questions like how the optical spectrum changes when an electron-withdrawing ligand is exchanged with one that donates electrons, and how the band gap changes with the size of the cluster, are readily answered. Indeed, the answers to these questions in particular are investigated already, but there are still uncertainties related to the optical and electronic properties of CdSe QDs which computational chemistry can help to resolve. Due to the broad source of experimental and theoretical literature available, it also serves well as a system with which a new methodology can be tested. First, we benchmark technical parameters like basis sets, functionals, and what the minimal distance between two QDs must be to get an artifact-free optical spectrum. Apart from that, we investigate the influence that different aliphatic and aromatic ligands have on the optical spectrum of $(CdSe)_{13}$.

3.1 Introduction

CdSe exists in two different lattice structures: the zinc-blende lattice, which has a rock-salt type structure, and the hexagonal wurtzite lattice. CdSe nanoclusters with wurtzite structure are well-known, while fewer reports about quantum dots (QDs) with zinc blende structure exist; see, for example, References [1, 2]. An important difference between them is that the wurtzite cell structure possesses a unique and polar *c*-axis [3], which can induce anisotropic growth along that axis [4]. Consequently, elongated or spherical shapes of the nanocrystals are expected, depending on the growing conditions that are set. To control the growth it is often sufficient to choose a certain ligand mixture. Contrary to the wurtzite structure, the zinc-blende crystal structure has an isotropic unit cell; therefore, isotropic structures like cubes and tetrahedrons can be expected. Furthermore, it is not the ligand mixture that determines the crystal shape but rather the reaction temperature [1].

There exist very interesting studies about different shapes of nanoclusters. Synthesis of nanorods, for instance, is easily controlled via the surfactant ligands. Scher *et al.* found that nanorods could form liquid-crystalline phases, which is very useful to incorporate them into photovoltaic applications or LEDs [5]. The formation of tetrapods has been reported, too [3, 6]. Tetrapods have the advantage that they will always align in the same way on a surface: three legs will touch the surface and the forth leg points away from it. In addition, hourglass structures made of *hcp* ruthenium were prepared [7].

As just mentioned, the wurtzite lattice facilitates the preparation of spherical nanocrystals, or quantum dots. Experimentally there were several attempts to identify the size of CdSe nanoclusters [8–11]. Jose *et al.* reported that the smallest clusters that they could assign to the UV/Vis correspond to $(CdSe)_3$ and $(CdSe)_6$ clusters [8], where $(CdSe)_6$ is the smallest possible cluster that maintains the wurtzite structure.

Cage-core clusters containing 13, 33 and 34 CdSe units were found to be exceptionally stable CdSe clusters by time-of-flight mass spectroscopy [9]. In the $(CdSe)_{13}$cage-core cluster the core is formed by one Se atom. Del Ben *et al.* were able to assign the excitonic transition between 350–360 nm (3.44–3.54 eV) to the $(CdSe)_{13}$ cluster by comparing the experimental spectrum obtained by Kudera *et al.* [10] with that simulated for this specific cluster, effectively

confirming the cage-core structure.

Just recently, an experimental paper was published where the authors selectively synthesized [$(CdSe)_{13}$(n−octylamine)$_{13}$] and [$(CdSe)_{13}$(oleylamine)$_{13}$] nanoclusters [11]. In that study, the correctness of the assignation was justified by presenting elemental analysis and mass spectroscopy. Additionally, they used the corresponding spectrum that Del Ben *et al.* reported for the $(CdSe)_{13}$ QD capped with formate/hydrogen ligand pairs [12]. Both spectra coincide nearly perfectly, although the two authors used different ligands to obtain their respective spectrum. This is somewhat surprising since Del Ben *et al.* presented a spectrum for the $(CdSe)_{33}$ cluster that has the dangling bonds saturated with methylamine that shows the first absorption peak 0.5 eV lower in energy than the QD saturated with the formate/hydrogen ligand pair.

Another cage-core structure that was discussed in literature is that of the $(CdSe)_{33}$ and $(CdSe)_{34}$ clusters. They are formed by a $(CdSe)_{28}$-cage, where a small core of a cluster that contains 5 or 6 CdSe units is placed. Within the $(CdSe)_{34}$ QD fits a 6 unit cluster. For it the binding energy per CdSe unit is more stable than for the $(CdSe)_{33}$ cage-core cluster [13], where a 5 unit cluster fills the cage. The first absorption peak of 415 nm (2.98 eV) was attributed to these larger clusters [9]. Based upon these results, we modeled a series of three differently sized clusters with 6, 13, and 34 CdSe units.

It must be said that Nguyen *et al.* found in their calculations that the experimentally observed $(CdSe)_{34}$ cluster is actually the least stable one out of a series of $(CdSe)_{34}$ clusters [14]. The most stable isomer is a two-layer wurtzite structure. Other work used the cluster model consisting of 33 CdSe units [12, 15–19]. Nguyen *et al.* explained their result with the fact that the clusters observed by Kasuya *et al.* by laser ablation experiments might not follow the thermodynamics of $(CdSe)_n$ as they investigated it.

When we talk about quantum dots, then we cannot omit to discuss the influence of the capping ligands. Compared to the bulk geometry the surface of a QD undergoes heavy reconstruction. It was found theoretically that the degree of the reconstruction is the same independently if the cluster was optimized in vacuum or with ligands added to the Cd surface atoms [12, 15, 20–22]. Upon reconstruction of the surface, some of the unsaturated bonds become saturated, but not all of them. These unsaturated bonds are a source of free charge

carriers, which have a negative impact on the efficiency of QDSSCs because they introduce exciton relaxation pathways. Due to the strong spatial confinement in nanosized clusters, carrier–carrier, or Coulomb, interactions are much stronger as they would be in a bulk system [23]. Because of the high surface-to-volume ratio, the number of free charge carrier, which typically are localized on the surface, becomes higher as the QD gets smaller. Also, the number of two-coordinated surface Cd atoms is another critical parameter that defines the optical absorption properties [22].

Generally, most syntheses use a mixture of trioctylphosphine (TOP), trioctylphosphine oxide (TOPO), and oleic acid (OA) within which the formation of CdSe nanoclusters finally takes place. The thus synthesized QDs are usually capped with TOPO or OA. In a next step, the ligands may be exchanged with ligands that are more interesting to the researcher. Typical ligand molecules are carboxylic acids, phosphine oxides, amines, thiols, and phosphines. Some computational efforts have been made to elucidate the interactions between ligand and quantum dot.

An extensive report about CdSe cluster/ligand interactions based on DFT calculations was published by Yang *et al.* using a minimal $(CdSe)_2$ cluster [24]. A follow-up of this work was presented a few years later, but now, rather than a minimal system setup, they employed larger CdSe cluster models having 6 and 13 units of CdSe. In both studies these authors found that the order in binding strength between Cd surface atoms and the ligand is Cd-O > Cd-N > Cd-P [24, 25]. Yang *et al.* further reported that 2-coordinated Cd atoms are not being doubly capped, even though their coordination number is not filled [25]. This is easily understood considering that steric interactions between neighboring ligands would weaken the QD-ligand bond. Furthermore, they also found that the ligands that they have considered in their work do not bind to Se surface atoms.

Just recently, de la Fuente *et al.* published a study where they investigated the impact of several organic and inorganic passivation agents [26]. They found that the overall efficiency of the QDSSC was best when alkylamines like DMA and ETDA, or alkylthiols like EDT are used, whereas the efficiency worsens considerably when ligands that bear carboxylic groups are adsorbed on the QD's surface. Inorganic ligands like I or Cl have the potential to enhance the cell

efficiency but this depends on the underlying materials. TOPO is not a good ligand if the QD should be used in a photovoltaic application because the long aliphatic chains act like an insulator and inhibit the interaction between QD and the sensitized semiconductor.

Another way to control exciton relaxation has been reported by Tan *et al.* They found that 4-dimethylaminothiophenol (DMATP) successfully stabilizes the photogenerated hole, while thiophenol, oleic acid, or 1-dodecanethiol do not, or only to a smaller extent [27]. Liu *et al.* reported that thiophenol and *p*-hydroxythiophenol do scavenge successfully the photogenerated holes in CdSe through the aromatic π-electrons [28]. In their study, they further stated that direct linkage of the ligands enhances the photoluminescence quenching. However, if ligands are used to passivate the QD surface that strongly couple to electrons, as it is the case, for example, when a Si cluster is passivated with H atoms, the electrons relax on several timescales faster than photogenerated holes [29].

When the ligand facilitates the stabilization of the hole by delocalizing it within the ligand sphere, the injection into the TiO_2 semiconductor will be facilitated, too, thus increasing the overall efficiency of the solar cell. Tan *et al.* and Liu *et al.* explain the increased stabilization of positive charges by the type of substituents of the aromatic thiol and the location of the residual charge [27, 28]. This is in contrast to an earlier report about the relative stability between aliphatic and aromatic thiols reported by Aldana *et al.* where they state that aromatic thiols are less stable than aliphatic ones [30].

The explanation to this contradiction is found in the nature of the substituent at the *para* position to the thiol group of thiophenol. Aldana *et al.* used 4-mercaptobenzoic acid (MBA), while Tan *et al.* employed DMATP. MBA has a carboxylic group at the *para* position to the thiol group, DMATP a dimethylamino group. With DMATP absorbed on the CdSe surface, fluorescence decreases by a factor of > 3000, proving its suitability as an effective stabilizer of the photogenerated charge. The main difference between the two substituents is their ability to donate electrons. The carboxylate group is a strong electron-*withdrawing* group (EWG), whereas the dimethylamino group is an electron-*donating* group (EDG). Therefore, the probability of a photogenerated electron to be trapped on an EDG ligand is small, whereas the photogenerated hole will

be delocalized on the ligands. This way the exciton lifetime will be increased because the electron and the hole are spatially separated. In a next step, an electron from the electrolyte can more easily quench the hole. The excited electron itself will be transferred to the semiconductor with higher probability as well, effectively utilized as electric charge in an electrical circuit.

Frederick *et al.* also reported about the effect that EDGs and EWGs placed on an aromatic ligand have on the electronic properties of a ligand-QD system [31, 32]. In lieu of thiophenol type ligands, they employed phenyldithiocarbamates (PTC), on which they exchanged the substituent located at the *para* position to the dithiocarbamate group. They chose PTC as a delocalizing ligand for their studies because its effectiveness is based upon spatial and energetic resonance with the orbitals of the QD. Also, dithiocarbamates are π-donors, therefore, mixing them with the QD's valence band (VB), which is mainly composed of Se $4p$ orbitals [33–35], is symmetry allowed. The most electron-donating substituent they employed was $N(CH_3)_2$, while the most electron-withdrawing substituent was CF_3. Electron withdrawing substituents stabilize the HOMO of the ligand, and as such, the HOMO moves from the VB edge down to the middle of the band. It results an augmented mixing of the VB states with the ligand's HOMO. Hole delocalization is not only observed on dithiocarbamates, but also on thiols. 4-mercaptophenol, for instance, has a high redox energy level and quenches the exciton emission efficiently [36].

Although the ligand types differ, Frederick *et al.* and Tan *et al.* coincide in that these types of ligands can alter the optical properties of a given ligand-QD system in a beneficial way. Strong coupling between ligands and QD makes the ligand shell a part of the QD system, and a hybrid system results where the ligand shell acts as hole recipient [27, 31]. Therefore, a change in the chemistry of the ligands alters the strength of the nonadiabatic coupling and, consequently, control is gained over the rates of energy losses in QDs [29]. The mechanism by which the photogenerated hole of the QD delocalizes over the ligand is by donation of electron density from the π orbitals into the Se $4p$ orbitals of CdSe. As a result, electron density is added to the interfacial region, which in turn lowers the energy barrier for tunneling of the hole into the interface QD-ligand [31, 37].

The effect of the electron delocalization can be estimated using the Hammett

constant σ_{para}. σ_{para} reflects the substituent-induced change in electron donation in absence of resonance stabilization. For instance, σ_{para} for the dimethylamino group is equal to -0.83. The more negative the value, the more effectively the substituent will quench fluorescence [27].

The group around Talapin investigated a different kind of ligand. Instead of using organic ligand molecules, they used inorganic ligands, which may contain metal atoms. Examples for such ligands are $In_2Se_4^{2-}$ $Cu_7S_4^-$, $Sn_2S_6^{4-}$, $In_2Cu_2Se_4S_3^{3-}$, or SnS_2 [38–41]. They introduced completely metal-free ligands, too. Therefore, ligands like S_2^-, HS^-, Se_2^-, HSe^-, Te_2^-, HTe^-, TeS_3^{2-}, OH^-, or NH^- could be employed [37, 42, 43]. Such inorganic capping ligands offer an interesting alternative to the traditional organic ligands as they do not generate surface traps at the QD surface, and they provide further a very smooth energy landscape [37].

3.2 Basis sets and functionals

Here we test two GGA and two hybrid functionals for their performance related to the simulation of absorption spectra. These are the PBE and the BLYP functionals as representatives of the GGA functionals; for the hybrids the PBE0 and the B3LYP functionals are employed. The results presented in this section

Table 3.1 Bond lengths, bond angles, and optical band gaps for the bare $(CdSe)_6$ cluster. The distances d_1 and d_2 and the angles α_1 and α_2 are defined in Fig. 3.1(a) and 3.1(b).

	d_1, [Å]	d_2, [Å]	α_1, [°]	α_2, [°]	E_{abs}, [eV]
PBE, LANL2DZ	2.71	2.87	141.0	100.8	2.68
PBE0, LANL2DZ	2.66	2.82	140.7	100.7	3.03
BLYP, LANL2DZ	2.75	2.91	139.9	100.5	2.08
B3LYP, LANL2DZ	2.70	2.86	139.9	100.4	2.63
PBE, cc-pVDZ	2.60	2.83	145.7	100.7	2.03
PBE0, cc-pVDZ	2.58	2.79	144.6	100.6	-
PBE, def2-SVP	2.61	2.83	145.3	100.4	2.12
PBE, def2-TZVP	2.60	2.83	145.4	100.5	2.11
PBE, m-SR-DZVP	2.61	2.83	145.3	100.3	2.38
PBE0, m-SR-DZVP	2.56	2.80	145.9	100.2	3.41

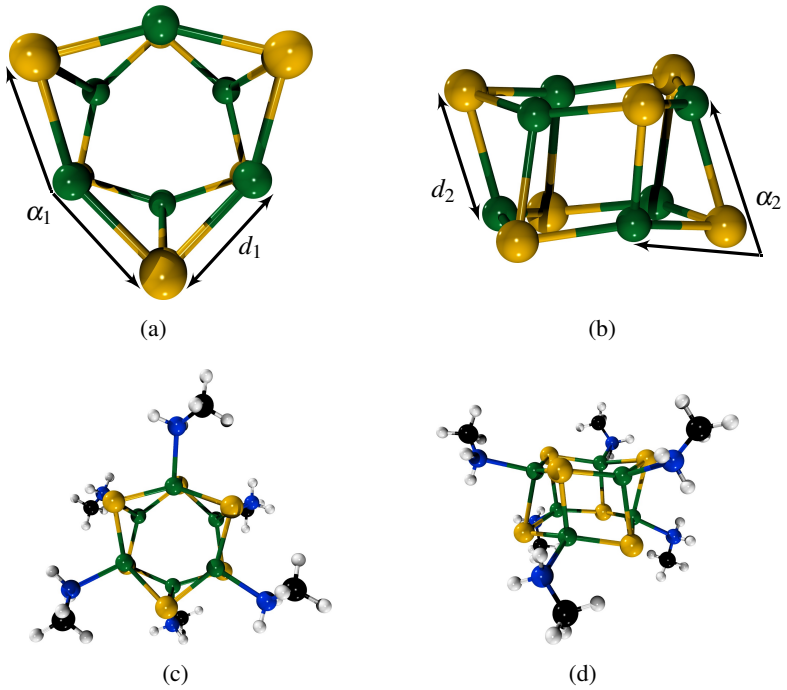

FIG. 3.1 Top (a) and side view (b) of the bare $(CdSe)_6$ cluster. The bond distance d_1 and the bond angle α_1 are indicated in (a), while d_2 and α_2 are shown in (b). In (c) and (d) are the top and the side view, respectively, of the saturated $(CdSe)_6$ QD. Cd atoms are represented in *green*, Se atoms in *yellow*, N atoms in *blue*, C atoms in *black*, and H atoms in *white*.

partially reproduce that reported in Ref. [44].

First, we look at the geometrical properties of the bare cluster obtained with the different basis sets that are tabulated in Table 3.1. The top and side view of the $(CdSe)_6$ cluster are illustrated in Fig. 3.1(a) and 3.1(b). The performance of the different basis sets is as such that larger basis sets give better geometries than the smaller ones [18]. At the B3LYP/LANL2DZ level of theory, the same geometry was reported earlier in literature [8, 14]. The bond lengths obtained with the PBE functional and the m-SR-DZVP basis set almost exactly reproduced the bond lengths obtained with the def2-TZVP basis set, indicating a very nice performance of these basis sets in terms of geometrical properties. Again, going along with the findings of Albert *et al.* [18], we observe that the geometry is quite basis set dependent.

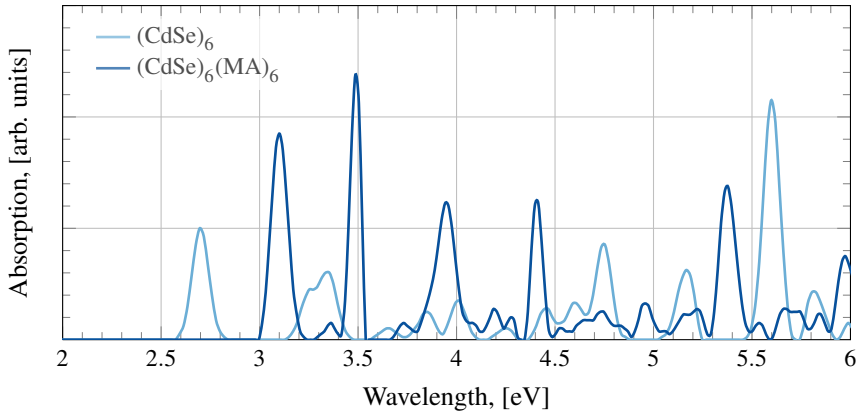

Fig. 3.2 Spectra of the $(CdSe)_6$ and the $(CdSe)_6(MA)_6$ clusters obtained with the LR-TDDFT methodology. The applied functional and basis set was the PBE functional, and the LANL2DZ basis set, respectively.

Now, we turn our attention to the optical absorption spectra. In a first step, we quantify the blue-shift induced by saturating the dangling bonds on the Cd atoms by comparing the absorption spectra of $(CdSe)_6$ and the ligated cluster, whose geometry is represented in Fig. 3.1(a) and 3.1(b). The shift is calculated as the difference between the two first absorption peak maxima, which are defined as the energy at which the first absorption peak of a given spectrum reaches its maximum. In Fig. 3.2 this difference is easily observed: upon saturation of the 6 Cd atoms with methylamine (MA), the spectrum shifts from 2.68 eV, which corresponds to the first absorption peak maximum, E_{abs}, of the bare $(CdSe)_6$ cluster, to 3.08 eV, the E_{abs} of $(CdSe)_6(MA)_6$. These spectra are computed with the LANL2DZ basis set and the PBE functional. The LR-TDDFT approach was applied to obtain the spectra. The excitation takes place between the HOMO-2, which is composed by a large part of Se $4p$ orbitals, and the LUMO, which mainly consists of the $5s$ orbitals on the Cd atoms.

The fact that the transition does not take place between the HOMO and the LUMO is rationalized by taking into account the symmetry of the involved MOs. The $(CdSe)_6$ cluster belongs to the D_{3d} point group, its HOMO-2 has A_{2u} symmetry and the LUMO A_{1g} symmetry. The HOMO-1 and the HOMO have E_g symmetry. Obviously, the transition between these twofold degenerated MOs and the LUMO is symmetry-forbidden.

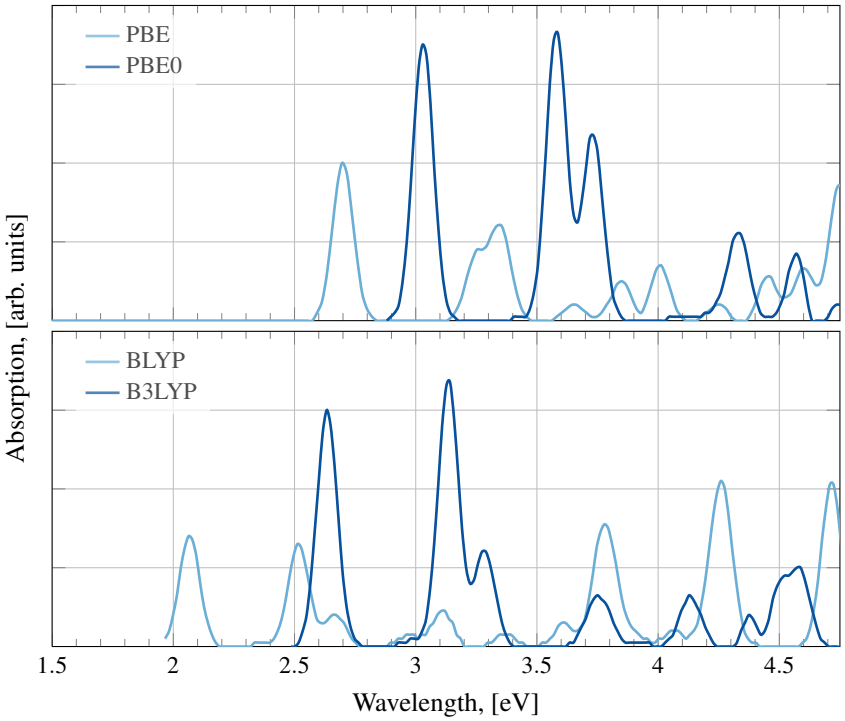

FIG. 3.3 Comparison of the GGA xc-functionals PBE and BLYP, as well as the hybrid xc-functionals PBE0 and B3LYP. All spectra are obtained using the LR-TDDFT methodology.

The first absorption peak maximum for $(CdSe)_6(MA)_6$ is found at 3.08 eV, in very good agreement with the experimental value of 3.14 eV obtained in a TOP/TOPO solvent mixture [8]. This excitonic transition includes the HOMO-2, HOMO-1 and HOMO orbitals and excites an electron into the LUMO. In contrast with the naked cluster, the presence of the ligand molecules lowers the symmetry of the system. As a consequence, transitions from the HOMO-1 and HOMO are now allowed.

We also calculated the spectra for bare cluster where the cc-pVDZ, def2-SVP and the def2-TZVP basis sets were applied in combination with the PBE functional. The corresponding E_{abs} are also tabulated in Table 3.1, which is found on page 57. We find that these larger basis sets shift the spectrum to the red, which is not desirable in this context since the tendency is as such that

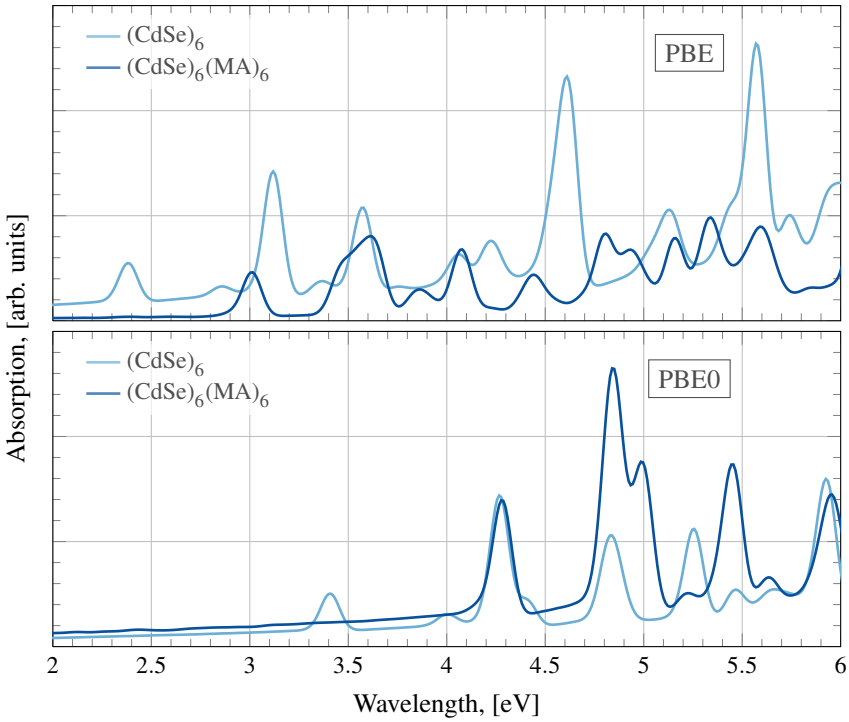

Fig. 3.4 Comparison of the spectra of the bare and ligated $(CdSe)_6$ cluster. In the upper panel the spectra obtained with the PBE functional are illustrated, while in the lower panel those obtained with the PBE0 functional are shown.

LANL2DZ/PBE spectra are already red-shifted with respect to experimental data.

We now compare the spectra obtained with the different xc-functionals, which are represented in Fig. 3.3. All spectra are computed using the LANL2DZ basis set for both Cd and Se. Clearly, the BLYP functional does not account satisfactorily for the position of the first absorption maximum; it underestimates it by roughly 0.6 eV. On the other extreme, the PBE0 hybrid functional does suffer from its well-known limitations: it overestimates the first absorption peak by almost 0.4 eV. The B3LYP functional performs much better as it gives a value that is only slightly below the PBE/LANL2DZ result, the difference being as small as 0.06 eV.

In order to see how the RT-TDDFT methodology performs in comparison

to the LR-TDDFT methodology, we examine the spectra for the bare and passivated $(CdSe)_6$ clusters in Fig. 3.4 for the PBE and the PBE0 functionals. Firstly, the first absorption peak maximum of the bare cluster experiences a red-shift of 0.3 eV compared to the LANL2DZ/PBE result. This wavelength is equivalent to a difference of 0.6 eV compared to literature values [13, 45]. When the dangling bonds on Cd are saturated, the performance is better but the energy of the first peak is still underestimated by 0.14 eV compared to the experimental value [8], and 0.08 eV below the LANL2DZ/PBE value. Again, when the PBE0 functional is applied, the shift to higher energies is considerable. For both the bare and the ligated $(CdSe)_6$ cluster the blue-shift is about 1 eV, severely overestimating the experimental value of 3.14 eV [8].

Overall, we can safely conclude that the combination m-SR-DZVP/PBE yields satisfactory results in terms of both geometry as well as optical absorption. Therefore, for what remains of the thesis we will employ this basis set/functional combination as it further offers a good ratio between accuracy and computational cost. Furthermore, if one considers the low efficiency of the LR-TDDFT methodology to simulate larger systems, RT-TDDFT is a valuable alternative to calculate large-scale systems efficiently. However, the disadvantage of the RT-TDDFT methodology is that it is very difficult to assign the absorption features in the spectrum and compare them to other experimental and theoretical work because no information about the MOs involved in the excitation is directly available.

3.3 Size matters: $E_{\mathbf{abs}}$ shifts with the cluster size

Fig. 3.5 shows nicely how the size of the QD determines the wavelength of E_{abs}: the smaller the cluster is, the higher is the energy at which the first optical transition occurs due to the opening of the band gap. The size dependence is best observed with the saturated QDs, since the band edge absorption for the bare $(CdSe)_6$ and $(CdSe)_{13}$ clusters coincide. In principle, the band edge for the bare $(CdSe)_6$ cluster should be blue-shifted due to its smaller diameter compared to $(CdSe)_{13}$. The peak of the largest $(CdSe)_{34}$ cluster is shifted to the red as expected and agrees well with results reported earlier in literature [12, 18], the differences being only 0.1 eV.

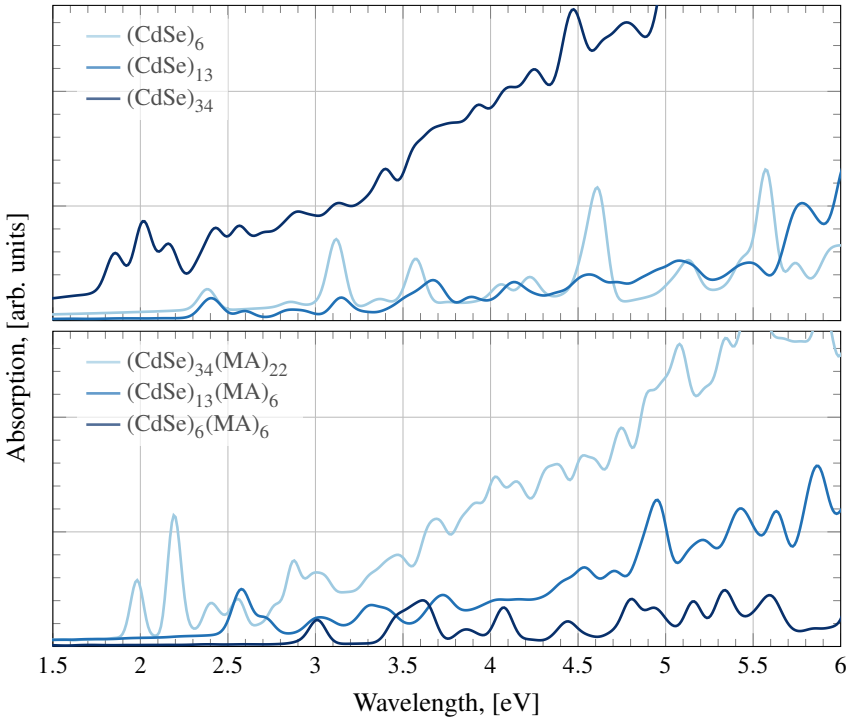

FIG. 3.5 Spectra to demonstrate the size dependence of the location of the first absorption peak. The upper panel shows the spectra of the bare clusters, while in the lower one those of the ligated QDs are illustrated.

As the results for the first absorption peak maxima in Table 3.2 show, the difference between the first absorption peak of the bare and the saturated 13 and 34 CdSe unit clusters is similar; the blue-shift is 0.18 eV when $(CdSe)_{13}$ is saturated, and 0.12 eV when the Cd atoms of the $(CdSe)_{34}$ cluster are ligated.

	E_{abs}, [eV]
$(CdSe)_6$	2.38
$(CdSe)_{13}$	2.40
$(CdSe)_{34}$	1.86
$(CdSe)_6(MA)_6$	3.01
$(CdSe)_{13}(MA)_6$	2.58
$(CdSe)_{34}(MA)_{22}$	1.98

TABLE 3.2 Wavelength of the first absorption peak maximum for the bare and ligated CdSe QDs as extracted from Fig. 3.5.

However, the spectrum of $(CdSe)_6(MA)_6$ is shifted by 0.63 eV compared to the bare cluster, which is a very large shift compared to the other two QD-ligand systems.

Furthermore, the red-shift of E_{abs} between the ligated $(CdSe)_6$ and $(CdSe)_{13}$ clusters amounts to 0.43 eV, and 0.60 eV when going from the $(CdSe)_{13}(MA)_6$ towards the larger $(CdSe)_{34}(MA)_{22}$ QD. Taking these results into account, E_{abs} of $(CdSe)_6$ should be located approximately at 2.8–2.9 eV. Indeed, the LR-TDDFT result indicates exactly that because $E_{abs}^{LR-TDDFT} = 2.68$ eV.

The spectrum of the $(CdSe)_{34}$ cluster nicely reproduces the one obtained by Del Ben *et al.* [12] in that their spectrum of the bare $(CdSe)_{33}$ cluster also shows three peaks, located each at 1.76, 1.96, and 2.09 eV. Please note that the authors pragmatically added 0.43 eV to their obtained results. This value is equivalent to the difference between the band gap that they calculated and the experimental band gap. We subtracted 0.43 eV from their results in order to be able to compare our results with theirs. Therefore, we can say that the triple peak Del Ben *et al.* reported is similar to that represented in Fig. 3.5, which shows up at slightly higher energies: 1.86, 2.02 and 2.16 eV, respectively. Nguyen *et al.* also found that $(CdSe)_{34}$ has the spectrum at slightly higher energies than $(CdSe)_{33}$, although the difference is small [14].

For the saturated $(CdSe)_{34}(MA)_{22}$ cluster we find $E_{abs} = 1.98$ eV, an underestimation compared to theoretical literature values by approximately 0.16 eV [12] and 1.0 eV when compared to experiment where the CdSe clusters are dissolved in toluene [9].

3.4 Distance dependence

When two quantum dots get close enough, the absorption spectrum will inevitably change due to the interaction between them. In Fig. 3.6, three spectra are represented which allow to observe how the spectrum changes depending on the distance between two QDs. Obviously, a separation of 3 Å is too close and the resulting spectrum is completely different from the single $(CdSe)_6$ cluster spectrum; it shows artifacts where the spectrum points in the opposite direction. These artifacts can be explained with the fact that the typical Cd−Se bond is around 2.6 Å, obviously the clusters are already experiencing some attractive

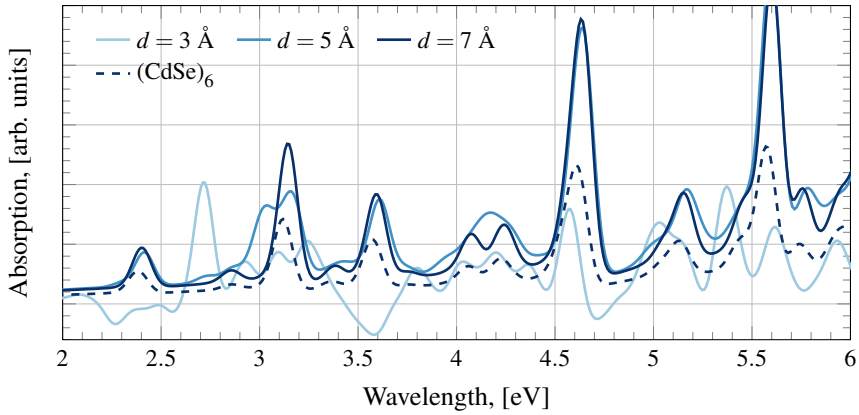

Fig. 3.6 The graphs illustrate the optical absorption spectra spatially separated 2 $(CdSe)_6$ QDs. The distance is indicated in the legend. For reference purpose also a single $(CdSe)_6$ cluster is included in the graph. d refers to the distance between the closest atoms of the two QDs.

interaction towards a bond formation. If two clusters are separated by 5 Å, the spectrum appears better but it still diverges from the single cluster spectrum. In particular, the single peak located at about 3.15 eV in the single $(CdSe)_6$ spectrum is divided into a second peak located at lower energies, and the intensities of these peaks is weaker than the intensity of the peak that shows up when the QDs are separated by 7 Å. Indeed, a distance of 7 Å is sufficient to simulate a spectrum which closely resembles to the $(CdSe)_6$ spectrum. The only difference is that the peaks are roughly as twice as high, which, however, is related to the double number of clusters.

Conclusively, a periodic system can be setup as such that periodic images are separated by at least 7 Å. Non-periodic systems on the other hand need a cell definition that includes roughly 7 Å of vacuum space between the outermost atoms and the cell walls, resulting in a cell size which is approximately 14 Å larger than the diameter of the QD itself.

3.5 Effect of the ligand position in the $(CdSe)_{13}$ cluster

As just shown, the spectra of saturated QDs experience a blue-shift when the dangling bonds on the QD surface are saturated [12, 15, 22]. However, it is also

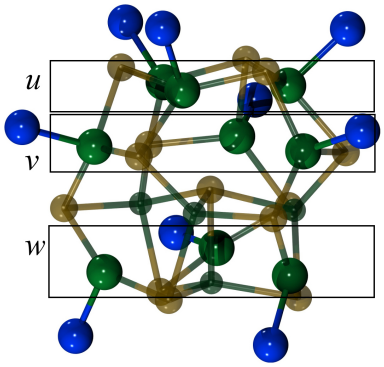

FIG. 3.7 Depiction of the three ligand planes *u, v* and *w*. Each plane consists of three Cd atoms that have a similar bonding environment. In the planes *u* and *v* the Cd are 3-coordinated, while in the lowest plane *w* they form only two bonds to Se. For the sake of visibility, the remaining QD atoms are depicted transparently, while C and H ligand atoms are omitted.

interesting to know which surface atoms contribute how much to the shift. A theoretical study performed earlier indicates that the two-coordinated Cd atoms have the most important influence on the optical spectrum of a CdSe QD [15].

Here, we simulate several spectra of the $(CdSe)_{13}$ QD with different arrangements of ligands. The $(CdSe)_{13}$ QD has three planes, wherein each of the unsaturated Cd atoms have an equivalent the bonding environment. The side view of the $(CdSe)_{13}$ cluster in Fig. 3.7 depicts these planes. Each plane consists of 3 Cd atoms. In the planes *u* and *v*, each Cd atom is 3-coordinated whereas in plane *w* they are only two-coordinated. The average charges localized on the Cd atoms in the bare cluster differs little between the planes. Plane *u* atoms are the least positively charged ones ($q = 0.207\ e$), and those in plane *v* are only slightly more positive ($q = 0.213\ e$). The atoms in the *w* plane are the most positively charged with $q = 0.252\ e$, which reflects the twofold coordination. 4-coordinated Cd have a charge of 0.14 *e*.

To investigate the influence of each ligand plane on the absorption spectrum,

TABLE 3.3 Averaged charges on the Cd atoms within a given plane *u, v* or *w*, together with the band gaps, E_g.

	(*000*)	(*300*)	(*333*)	(*003*)	(*033*)
u	0.207	0.208	0.301	0.211	0.308
v	0.213	0.253	0.223	0.210	0.163
w	0.252	0.242	0.170	0.140	0.143
E_g	2.32	2.34	2.42	2.54	2.49
E_{abs}	2.40	2.41	2.49	2.54	2.58

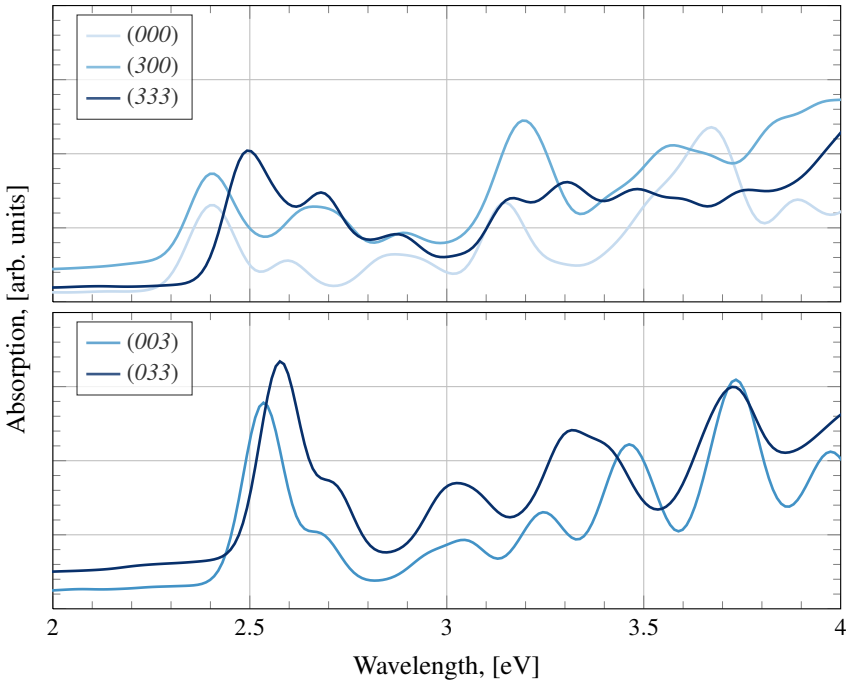

Fig. 3.8 Absorption spectra for the QD-ligand systems as they are described in the main text. The graphs are ordered with respect to the blue-shift of their respective spectrum.

we modeled in total 4 cluster-ligand systems: $(CdSe)_{13}(MA)_n$ with $n = 3, 6, 9$. We label them in the following manner. Each plane can contain at most three ligands, or they are not saturated at all. We did not consider adding only one or two MAs. Therefore, the fully saturated cluster will be labeled as (*333*), while the bare cluster is labeled (*000*), the labels referring to the planes *u*, *v*, and *w*, respectively. The following cluster-ligand systems were employed: (*003*), (*300*), (*033*), and (*333*), plus the bare cluster: (*000*). The corresponding spectra are illustrated in Fig. 3.8.

We observe the largest blue-shift with respect to the bare cluster for the (*033*) model (E_{abs} = 2.58 eV), followed by the (*003*) cluster. The results are presented in Table 3.3. Right after these systems, the fully saturated cluster, (*333*), follows with an E_{abs} = 2.49 eV. If only the *u*-plane Cd atoms are saturated, hardly any shift in the first absorption peak maximum happens. Clearly, the impact on

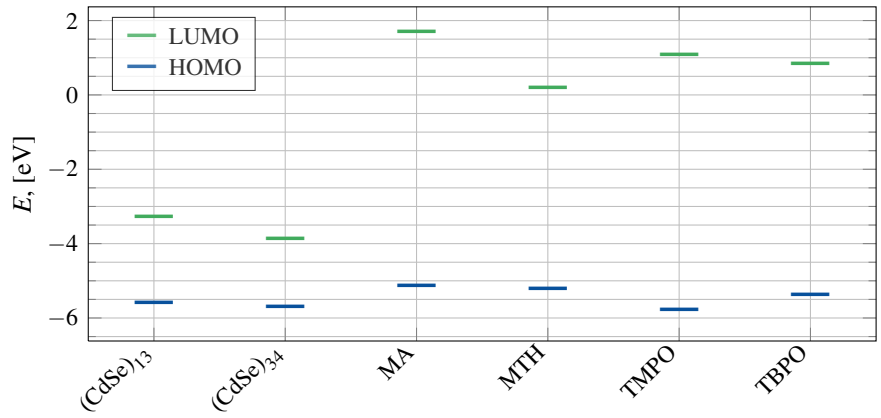

FIG. 3.9 Represented are the HOMO and LUMO energies, respectively, for the $(CdSe)_{13}$ and $(CdSe)_{34}$ clusters, as well as for the four aliphatic ligands that were used in this work. The ligands are not added to the CdSe clusters. HOMOs are shown in blue, LUMOs in green.

the spectrum is largest if the two-coordinated Cd atoms are saturated, while the impact of saturated 3-coordinated Cd atoms in the planes *u* and *v* is small. In this direction point the studies performed by Kilina *et al.* and Inerbaev *et al.* where they state that the number of two-coordinated Cd surface atoms is an important parameter related to the blue-shift of the optical spectrum [15, 22].

In Table 3.3 are also the averaged charges for each plane tabulated. The most interesting feature here is that the band gaps and the first absorption peak maxima correlate with the charge that is localized on the two-coordinated Cd atoms in plane *w*. Furthermore, the binding energy in the plane *w* is much larger ($E_{\text{bind}} = -1.30$ eV) than in plane *u* ($E_{\text{bind}} = -0.72$ eV), in accordance with Kilina *et al.* [15]. This is certainly a consequence of the lower coordination of the Cd atoms in the *w*-plane. In ligand exchange reactions, these ligands are more difficult to be exchanged.

3.6 Aliphatic ligands

In this section, we present the results for the $(CdSe)_{13}$ cluster, where the Cd atoms are saturated with different aliphatic ligand molecules. Apart from the methylamine ligand presented earlier, two additional types of organic molecules

are introduced here: thiols and phosphine oxides. Methylthiol is used as a representative of a thiol, which is structurally similar to methylamine. Two phosphine oxides are employed to mimic trioctylphosphine oxide used as a typical solvent-ligand in CdSe QD synthesis. The difference between them is that one has a short methyl chain (trimethylphosphine oxide, TMPO) and one a longer butyl chain (tributylphosphine oxide, TBPO).

Abuelela *et al.* analyzed the vibrational spectra of MA and TMPO ligands adsorbed onto the CdSe surface [19]. They report that TMPO strongly interacts with the surface Cd atoms whereas MA forms only a coordination bond. This strong interaction of TMPO reduces the P=O to a single bond. The experimental P=O bond length is 1.48 Å [46], which Abuelela *et al.* reproduced with their calculations on a 6-311++g(d,p)/B3LYP level of theory. After that, the ligand binds to the cluster, they report that this bond elongates to 1.64 Å, an increase of 0.16 Å. Here, we find only a small elongation from 1.49 Å (for TMPO) to 1.51 Å, when it is bound to the CdSe surface. For TBPO we find that P=O is slightly larger: $d_{\mathrm{P=O}}$ = 1.50 Å, and 1.52 Å when it is ligated to the QD.

As Frederick *et al.* concluded the ligand's HOMO should be close to or within the VB in order to obtain the maximal resonance effect [31]. Following this argumentation, and having a look at Fig. 3.9, the QD-TMPO system should show the most intense first absorption peak because its HOMO is slightly below the VB band edge of $(\mathrm{CdSe})_{13}$. Then, the longer aliphatic chain in TBPO results in a destabilization of the HOMO by 0.4 eV compared to the TMPO HOMO. The HOMOs of the amine and thiol ligands are slightly higher in energy by 0.2 eV than the TBPO HOMO. Out of this series, the MA ligand has the largest band gap.

To complement this data, we present in Table 3.4 the contributions that the different atom coefficients make to the HOMO-2, HOMO-1, HOMO, and LUMO. Furthermore, in Fig. 3.10 the partial DOS are represented for the bare cluster and all the QD-ligand systems except $(\mathrm{CdSe})_{13}(\mathrm{TBPO})_6$, which has a similar PDOS as $(\mathrm{CdSe})_{13}(\mathrm{TMPO})_6$. The DOS are reproduced in accordance to literature [17, 47–49]. The main part of the VB is contributed by the Se 4*p* orbitals, additionally the Cd 4*d* orbitals contribute to the VB, however, only little. The values in Table 3.4 indicate that the VB edge consists of 90 % Se atomic orbitals, and between 8 and 10 % of Cd atomic orbitals. If ligands are

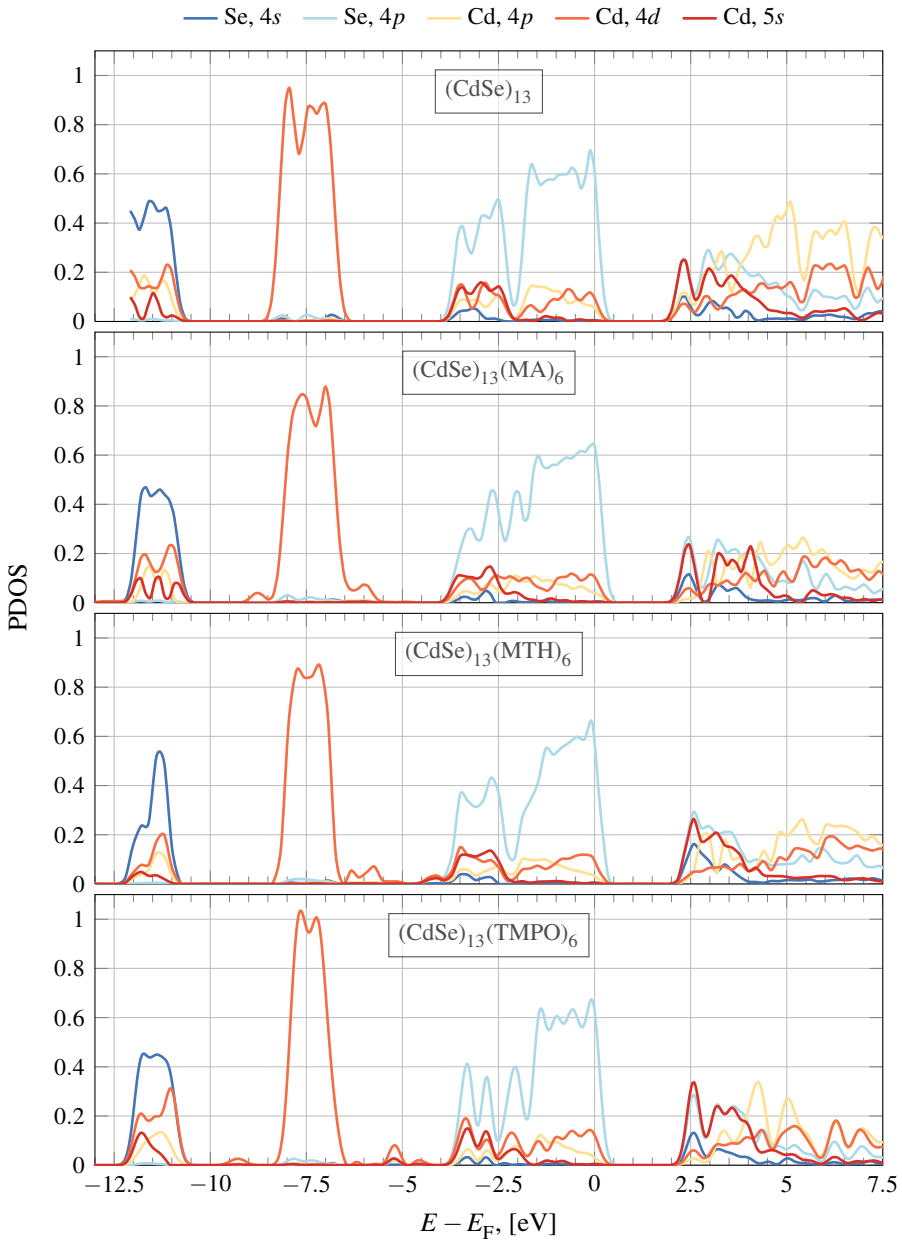

Fig. 3.10 PDOS of Cd and Se orbitals obtained for the bare $(CdSe)_{13}$ cluster as well as for the passivated clusters except $(CdSe)_{13}(TBPO)_6$, whose PDOS is very similar to that of $(CdSe)_{13}(TMPO)_6$.

present, they do not contribute any considerable amount to the MOs at the VB edge. Concerning the LUMO, the contributions change as such that Cd atomic orbitals now contribute 52 % if the bare CdSe cluster is considered, and still around 48 % if the QDs are passivated. Atomic orbitals localized on Se atoms now do contribute only about 45 % to the LUMO. From the ligand side the only significant contribution comes from the atoms that bind to Cd. The valence bands only differ at lower energies, the band edges are very similar for all systems. Conclusively, the electronic structure of the QDs does not change substantially upon passivation of the cluster surface. Similarly, the Cd 4*d* orbitals located at energies centered at −7.5 eV do not differ a lot from one model

TABLE 3.4 Shown is how much the coefficients of each atom species contribute to the 4 molecular orbitals HOMO-2, HOMO-1, HOMO, and LUMO. H coefficients are not included since they contribute very little to the MOs presented in this table.

		% HOMO-2	% HOMO-1	% HOMO	% LUMO
$(CdSe)_{13}$	Cd	8.01%	10.03%	9.91%	52.72%
	Se	91.99%	89.97%	90.09%	47.28%
$(CdSe)_{13}(MA)_6$	Cd	8.48%	10.05%	9.80%	46.27%
	Se	90.77%	89.05%	89.16%	43.94%
	N	0.57%	0.74%	0.85%	7.49%
	C	0.08%	0.08%	0.09%	0.78%
$(CdSe)_{13}(MTH)_6$	Cd	10.41%	8.81%	8.97%	48.19%
	Se	88.79%	89.86%	90.04%	43.25%
	S	0.62%	0.95%	0.84%	7.04%
	C	0.13%	0.27%	0.09%	0.49%
$(CdSe)_{13}(TMPO)_6$	Cd	7.97%	9.15%	8.46%	47.48%
	Se	91.29%	90.03%	90.71%	44.84%
	O	0.29%	0.43%	0.38%	4.52%
	P	0.04%	0.06%	0.06%	1.48%
	C	0.33%	0.27%	0.32%	0.97%
$(CdSe)_{13}(TBPO)_6$	Cd	8.95%	8.32%	8.71%	48.43%
	Se	90.08%	90.67%	90.47%	43.87%
	O	0.48%	0.26%	0.47%	4.60%
	P	0.05%	0.04%	0.05%	1.34%
	C	0.38%	0.60%	0.24%	1.42%

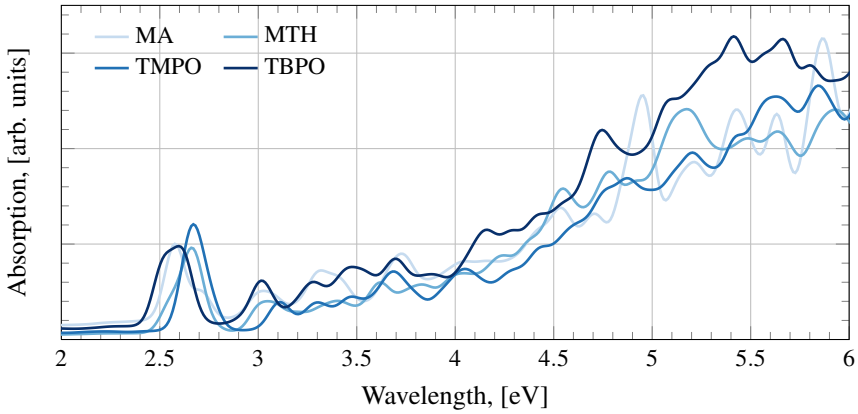

Fig. 3.11 Absorption spectra for the four aliphatic ligand systems $(CdSe)_{13}(LIG)_6$, where LIG refers to the ligands indicated in the legend of the plot.

system to another.

The values for q_{QD} in Table 3.5 reveals that the amine's N push electron density onto the QD, whereas when thiols are used as ligands then less negative charge delocalizes on the QD as compared to MA passivated systems.

The size of the band gaps, E_g, also included in Table 3.5, does not differ much from one system to another, neither does E_{abs}. Both are within 0.1 eV. The spectra in Fig. 3.11 reveal that the intensities of the first absorption maximum peaks are similar, except $(CdSe)_{13}(TMPO)_6$ which has the most intense first absorption feature. This goes along very nicely with the prediction made above that this system should have the most intense first absorption peak maximum. Additionally, a small blue-shift of 0.07 eV is induced when compared to the $(CdSe)_{13}(TBPO)_6$ spectrum. Schreuder *et al.* reported this result earlier in an

Table 3.5 Sums of partial charge of the total QD. Also the band gap E_g and the first absorption maximum E_{abs} are tabulated.

	q_{QD}, [e]	E_g, [eV]	E_{abs}, [eV]
$(CdSe)_{13}(MA)_6$	−1.59	2.49	2.58
$(CdSe)_{13}(MTH)_6$	−0.94	2.48	2.66
$(CdSe)_{13}(TMPO)_6$	−1.08	2.50	2.67
$(CdSe)_{13}(TBPO)_6$	−1.07	2.42	2.60

experimental study where they found that longer alkyl chains in phosponic acids pin the emission wavelength at higher energies [50]. Apart from this, the second peak of the QD-TMPO system is also located at shorter wavelengths (3.11 eV) than those of the remaining systems, which have this absorption peak located right at 3 eV.

The thiol group has a similar impact on the absorption spectrum of $(CdSe)_{13}$ as the TMPO ligand, however not for the overlap of the ligand HOMO but for the S atom's properties. The MTH spectrum in Fig. 3.11 shows that the thiol ligand molecules induce a blue-shift when compared with the $(CdSe)_{13}(MA)_6$ spectrum. One possible explanation for this is that S, similarly to TMPO, hybridizes well with the CdSe VB, although this time not for the relative energy of the HOMO but rather due to symmetry reasons.

3.7 Aromatic ligands

The situation becomes more diverse when aromatic ligands are employed. Here, we use benzene rings with two substituents, out of which one binds to the QD. The second substituent will be changed to investigate the influence of it on the electronic properties of the QD-ligand system. Depending on this substituent, a ligand may become electron-donating or -withdrawing. If it is donating, then the aromatic ligand stabilize the photogenerated hole [27], if it is withdrawing it is thought to shift the spectrum to longer wavelengths [31]. The Hammett constants σ^{+}_{para} and σ^{-}_{para} do quantify the electron-donating or -withdrawing ability of a substituent and, therefore, might serve as a tool to preliminarily assess how strong the *para* substituent's influence on the electronic properties of the QD can be.

The Hammett constants σ^{+}_{para} and σ^{-}_{para} are usually employed when the *para* substituent develops a resonance stability. In this case, the aromaticity of the benzene ring extends to the substituent. Now, electron-donating groups (EDGs) are more effective at donating, while electron-withdrawing groups (EWGs) are more effective at withdrawing electron density. However, if the complete QD-ligand model is optimized, we observe that only one out of the six ligand molecules are completely planar. Therefore, we will use only σ_{para} for what follows.

We check if and to what extent the functional groups of aromatic ligand

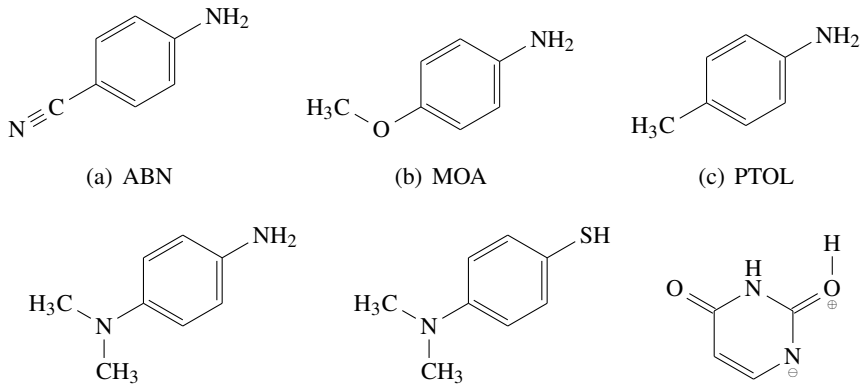

FIG. 3.12 The ligand molecules as they are employed in this work.: (a) 4-aminobenzonitrile, (c) p-toluidine, (b) 4-methoxyaniline, (d) N,N-dimethyl-p-phenylenediamine, (e) 4-dimethylaminothiophenol, and (f) uracil in the zwitterionic form. Uracil binds via the N atom without H to Cd. In the subcaption, the short form of each molecule is written.

molecules influence the absorption spectrum of the CdSe QD. To do so, we employed several ligands based on an aniline-like aryl structure, as well as the thiophenol type DMATP ligand, and uracil. The structures are represented in Fig. 3.12. In the first series of ligand molecules, the amine substituents are the anchors through which the ligands coordinate to the Cd surface atoms. The differences are found at the *para* position. Apart from the dimethylamino group, we chose the methyl, methoxy, and nitrile substituents. With this choice, we define a wide range of electron-donating groups, where σ_{para} ranges from -0.17 (methyl) to -0.83 (dimethylamine). With the nitrile substituent, the series includes also an EWG representative. This results in the following set of ligands: apart from DMATP, we calculated spectra with 4-aminobenzonitrile (ABN), p-toluidine (PTOL), 4-methoxyaniline (MOA), N,N-dimethyl-p-phenylenediamine (DMPDA), and uracil (URA).

We first characterize the ligand molecules. As can be seen in Fig. 3.13 the HOMO of the aniline type ligands is more and more stabilized as the functional group becomes more electron-withdrawing. The HOMO and the LUMO of DMATP and DMPDA have similar energies but with the thiol group, the MOs become slightly more stable by 0.15 eV. E_{g}, however, is the same for both.

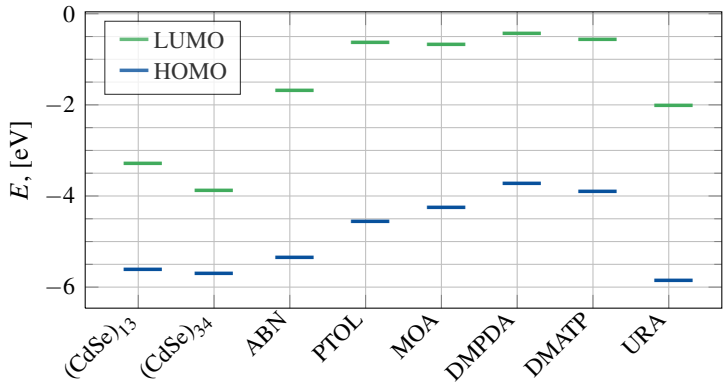

FIG. 3.13 Equivalent to Fig. 3.9, the HOMO and LUMO energies of the naked $(CdSe)_{13}$ and $(CdSe)_{34}$ clusters, as well as those of the isolated aromatic ligands are represented here.

The optical absorption spectra of the ligand molecules only, except uracil, are represented in Fig. 3.14. ABN, as a ligand that contains an EWG, has the same first absorption feature as PTOL, but it shows a second, more intense peak at the same wavelength where the DMATP spectrum has the first absorption peak maximum (4.25 eV). Within the set of electron-donating ligands, the first absorption peak maximum does correlate nicely with the Hammett constant that is attributed to the *para* substituents of the corresponding ligand. The pattern for the three ligands PTOL, MOA, and DMPDA is as such that the higher the ability to donate electron density the more the spectrum shifts to shorter wavelengths.

When the two ligands DMPDA and DMATP that contain the dimethylamino group are compared then the main difference is that the second absorption peak of DMATP is 0.18 eV lower in energy than the corresponding peak in the DMPDA spectrum. It seems that S can interact better with the π cloud of the benzene ring, thereby lowering the energies of the orbitals involved in this excitation.

Uracil complements this ligand series. In principle uracil and other DNA bases have the potential to increase the electronic coupling between QDs by forming base pairs but still without tying QDs too strongly [51]. The cited reference does employ adenine rather than uracil and they find that when adenine is adsorbed onto a bare CdSe cluster the absorption spectrum blue-shifts, but red-shifts if the cluster is H passivated. The second results needs to be taken with

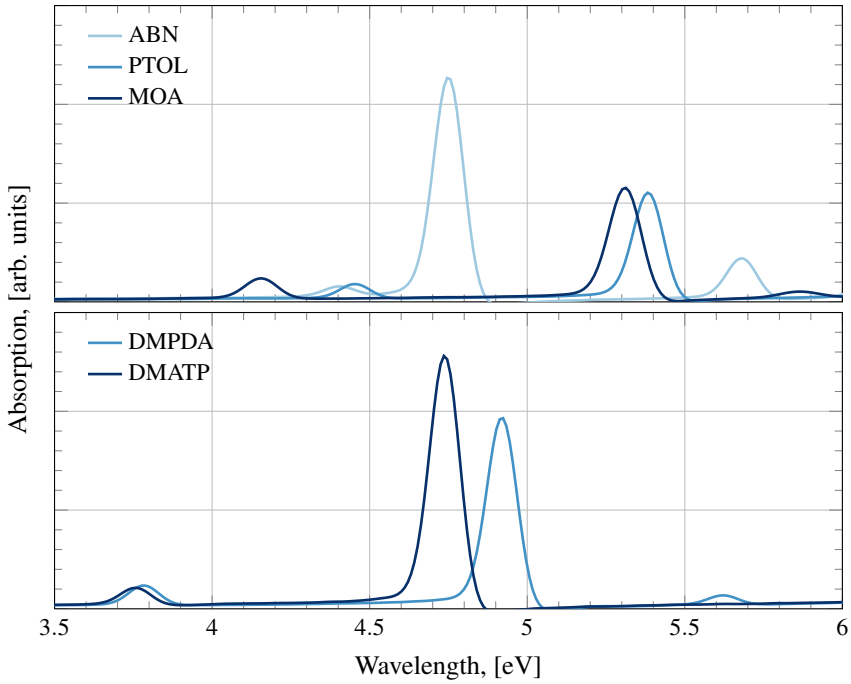

FIG. 3.14 Absorption spectra of the ligands as they are represented in Fig. 3.12.

care as it was shown that H is not a suitable ligand for QD surface passivation, as it tends to disrupt Cd−Se bonds on the surface [24]. Fig. 3.13 shows that uracil in the zwitterionic state, as we employ it, has the lowest E_{HOMO} of all the ligand molecules, it is even located under the VB edge of the two bare CdSe QDs included in the graph. This result is similar to that of the TMPO ligand, and if it behaves like the $(\mathrm{CdSe})_{13}(\mathrm{TMPO})_6$ system, this ligand will induce a noticeable blue shift. All the other ligands have HOMO levels above the CdSe VB edge.

Before we discuss the absorption spectra of the QD-ligand systems we present in Fig. 3.15 the HOMO and LUMO levels of the $(\mathrm{CdSe})_{13}(\mathrm{LIG})_6$ models for which we calculated the optical spectra. For reference reasons, the HOMO and LUMO levels for $(\mathrm{CdSe})_{13}(\mathrm{MA})_6$ are included as well. The relative tendency between the HOMO and LUMO energies is the same as in Fig. 3.13 for the isolated ligands: the better the electron-donating abilities of a given substituent, the more stabilized are the HOMOs. Furthermore, it is the $(\mathrm{CdSe})_{13}(\mathrm{URA})_6$

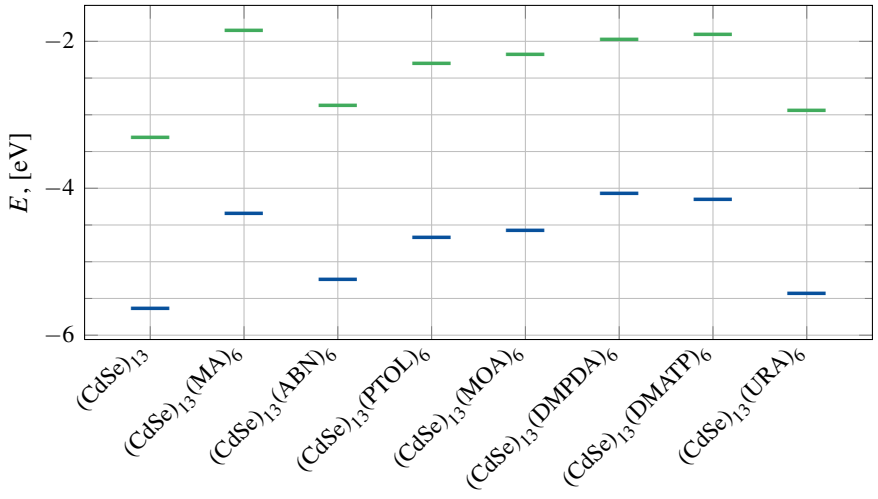

FIG. 3.15 Indicated are the HOMO and LUMO energies for $(CdSe)_{13}$ clusters that are saturated with the aromatic ligands presented in Fig. 3.12.

model that has the most stable HOMO.

We present again data that consists of how much the atomic orbitals of a given element contributes to the MOs HOMO-2, HOMO-1, HOMO, and the LUMO. The results are shown in Table 3.6. This table shows that only $(CdSe)_{13}(ABN)_6$ has a similar composition of the atomic coefficients as the aliphatic ligand systems in Table 3.4 on page 71. The main difference is that the Se atoms contribute less to the LUMO, while it is made of 9 % of C atomic orbitals. This clearly reflects the electron-withdrawing capabilities of the nitrile group since all other systems do not show such a high percentage for C.

The next two QD-ligand models to discuss are the $(CdSe)_{13}(PTOL)_6$ and $(CdSe)_{13}(MOA)_6$ QD-ligand clusters, which are also similar to the systems where aliphatic ligands passivate the CdSe surface. Unlike to $(CdSe)_{13}(ABN)_6$ the C atoms do not contribute more to the LUMO. However, the $(CdSe)_{13}(PTOL)_6$ system shows an irregularity in that the contributions made by the Se, N, and C atomic orbitals to the HOMO-1 are completely incomparable to those systems so far presented. Se atomic orbital coefficients make a 43 %, N almost 17 %, and C atomic orbitals nearly 32 %. This is indeed very strange and difficult to explain, especially because the HOMO-2 and the HOMO

TABLE 3.6 Shown is how much the coefficients of each atom species contribute to the 4 molecular orbitals HOMO-2, HOMO-1, HOMO, and LUMO. H atomic orbitals are not included because except for $(CdSe)_{13}(DMPDA)_6$ they do not contribute significantly to the MOs.

		% HOMO-2	% HOMO-1	% HOMO	% LUMO
$(CdSe)_{13}$	Cd	8.01%	10.03%	9.91%	52.72%
	Se	91.99%	89.97%	90.09%	47.28%
$(CdSe)_{13}(ABN)_6$	Cd	9.41%	8.44%	10.63%	45.94%
	Se	89.68%	90.70%	88.44%	40.50%
	N	0.47%	0.40%	0.45%	4.35%
	C	0.38%	0.42%	0.42%	8.94%
$(CdSe)_{13}(PTOL)_6$	Cd	8.74%	5.19%	8.24%	50.38%
	Se	83.50%	43.24%	89.61%	41.94%
	N	2.82%	16.75%	1.04%	5.39%
	C	4.47%	31.63%	1.00%	1.67%
$(CdSe)_{13}(MOA)_6$	Cd	8.10%	9.05%	8.26%	49.08%
	Se	82.19%	80.64%	87.60%	42.63%
	N	3.23%	3.24%	1.66%	5.76%
	O	1.81%	1.99%	0.64%	0.14%
	C	4.24%	4.63%	1.63%	1.59%
$(CdSe)_{13}(DMPDA)_6$	Cd	1.12%	0.89%	1.27%	48.51%
	Se	4.44%	2.37%	5.17%	41.55%
	N	44.89%	44.69%	44.35%	7.37%
	C	39.27%	40.57%	40.35%	1.59%
	H	10.28%	11.48%	8.86%	0.97%
$(CdSe)_{13}(DMATP)_6$	Cd	5.86%	4.21%	2.90%	48.69%
	Se	61.62%	39.32%	22.92%	41.41%
	N	12.06%	19.95%	22.98%	0.32%
	S	4.30%	9.44%	16.23%	6.07%
	C	13.11%	22.18%	29.43%	3.04%
	H	3.04%	4.89%	5.54%	0.46%
$(CdSe)_{13}(URA)_6$	Cd	8.92%	10.30%	9.60%	45.23%
	Se	88.68%	88.35%	87.78%	47.08%
	N	0.73%	0.64%	0.56%	3.56%
	O	1.15%	0.36%	0.53%	2.01%
	C	0.26%	0.30%	0.18%	0.74%

show the typical distribution of percentages as it is expected from earlier results presented herein.

$(CdSe)_{13}(DMPDA)_6$ and $(CdSe)_{13}(DMATP)_6$ show differing results. In particular $(CdSe)_{13}(DMPDA)_6$ has a VB edge that have very low contributions from Cd and Se atomic orbitals; together they contribute at most 7 % to the three HOMOs that are shown in Table 3.6. Obviously, the VB edge is formed mainly by atomic orbitals localized on the ligand molecules. Nitrogen's share is over 44 %, while C and H contribute 50 % to these HOMOs. When the amine linking group is exchanged with the thiol substituent, the ligands contribute most to the HOMO, about 74 %, but this is reduced to 33 % in the HOMO-2. The LUMO shows again the typical distribution as seen in all the other QD-ligand models, where almost 50 % comes from Cd atomic orbitals, and about 40 % from Se.

Remains $(CdSe)_{13}(URA)_6$, which does not show any diverging features from the general case. The distribution of the percentages is, however, very similar to the $(CdSe)_{13}(ABN)_6$ system. These two systems have the highest contributions from Se atomic orbitals to the three HOMOs that are presented here. When uracil is used as ligand, Se even contributes more than Cd to the LUMO, which is the only case out of all QD-ligand systems considered here.

We mentioned earlier in this chapter that the Hammett constant could be used to predict the red- or the blue-shift, respectively, of an optical spectrum. Unfortunately, as can be seen in Table 3.7, such a relationship can only be made between the Hammett constant and the charges on the QD, q_{QD}. As the functional group is more electron-donating, the QD becomes more negatively

TABLE 3.7 Partial charges on the QD, q_{QD}, Hammett constant of the substituents in the *para* position, σ_{para}. Also the HOMO-LUMO gap E_g and the first absorption maximum E_{abs} are tabulated.

	q_{QD}, [e]	σ_{para}	E_g, [eV]	E_{abs}, [eV]
$(CdSe)_{13}(ABN)_6$	−0.94	0.66	2.37	2.44
$(CdSe)_{13}(PTOL)_6$	−1.06	−0.17	2.35	2.45
$(CdSe)_{13}(MOA)_6$	−1.12	−0.27	2.40	2.56
$(CdSe)_{13}(DMPDA)_6$	−1.21	−0.83	2.09	2.22
$(CdSe)_{13}(DMATP)_6$	−0.82	−0.83	2.24	2.28
$(CdSe)_{13}(URA)_6$	−0.68	–	2.49	2.63

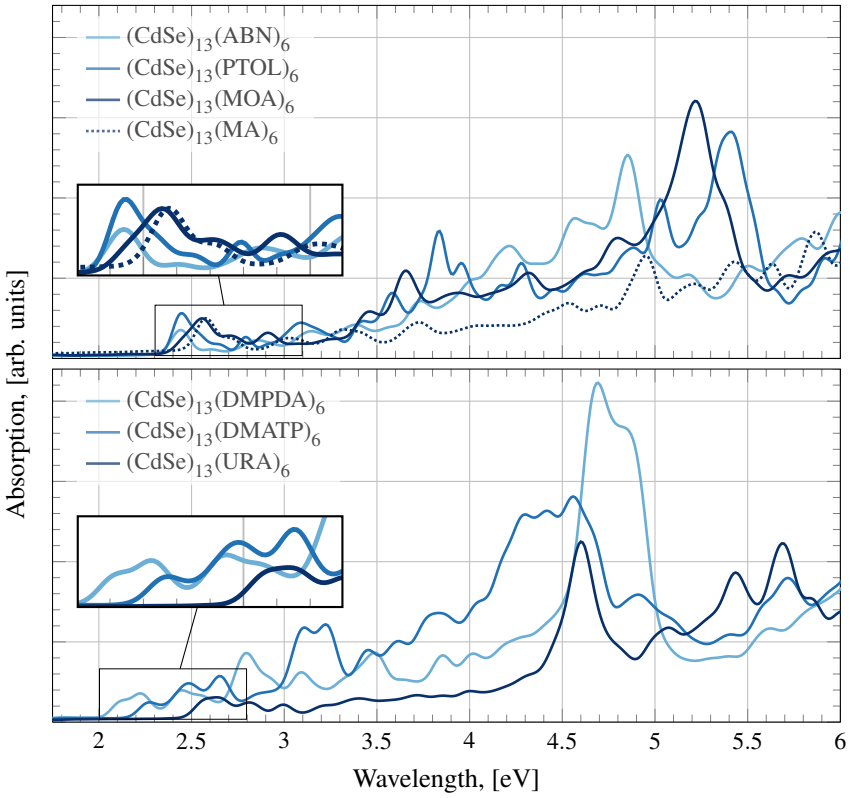

FIG. 3.16 In the upper panel are the spectra of three aromatic ligand-QD systems illustrated, where the ligands are ABN, PTOL, and MOA. for reference purpose, the spectrum of $(CdSe)_{13}(MA)_6$ is included as well. The spectra of the remaining aromatic ligand-QD systems are represented in the lower panel. The different ligands used to calculate these spectra are illustrated in Fig. 3.12. The insets show a magnified portion of the lower energy range of the graphs.

charged. Additionally, we find that the same relation between the amine type and the thiol type ligand occurs as it was discussed on page 72 for the MA and MTH ligands already. When DMATP is used then there is less negative charge on the QD, although the difference between DMPDA and DMATP is by 0.26 e smaller than the deviation between MA and MTH. Throughout all models employed here, the CdSe cluster with the least negative charge is the one where uracil has been adsorbed.

Optical absorption spectra simulated for the different $(CdSe)_{13}(LIG)_6$ sys-

tems are illustrated in Fig. 3.16; the corresponding first absorption peak maxima E_{abs} are also listed in Table 3.7, together with the charge q_{QD} that indicates how much the QD itself is charged, the Hammett constants, and band gaps. A quick comparison with the aliphatic ligand passivated QDs (c.f. Fig. 3.11 on page 72) reveals that the values of E_{abs}, for instance, varies over a range of 0.4 eV, while ΔE_{abs} for the aliphatic ligand is limited to a delta of about 0.1 eV. Also, the shapes of the aromatic ligand spectra are more heterogeneous. Furthermore, the intensities at higher energies are in general higher when aromatic ligands are considered.

The spectra for the $(\text{CdSe})_{13}(\text{ABN})_6$ and $(\text{CdSe})_{13}(\text{PTOL})_6$ represented in the upper panel in Fig. 3.16 show that for both models the first absorption peak occurs at an energy of around 2.45 eV; also the corresponding band gaps are very close. In the ABN spectrum, this first and the second, smaller peak at 2.6 eV cover together the same energy range as the broad PTOL peak; it ranges from 2.3 to 2.7 eV. This finding is somewhat in contrast to the study of Frederick *et al.*, which state that electron-withdrawing groups should result in a red-shift of the spectrum [31], which is obviously not the case. The most probable reason for this is that the amine group does not hybridize as well with the Se $4p$ orbitals as the dithiocarbamate functional group would do, where the S atoms are sp^2 hybridized and, therefore, the whole molecule is able to build up a resonance structure and interact better with the QD.

The third spectrum we present here is the $(\text{CdSe})_{13}(\text{MOA})_6$ system. From a first glance, the first absorption peak is almost identical to the one for $(\text{CdSe})_{13}(\text{MA})_6$. It is located at 2.56 eV, the following, smaller peak is found at 2.72 eV. Only beyond the third peak, which is located at 2.9 eV, the spectra differ. Then, at energies higher than roughly 3.3 eV, all three spectra gain in intensity, while the aliphatic ligand systems show relatively low intensity at higher energies. The $(\text{CdSe})_{13}(\text{PTOL})_6$ spectrum, for example, is three times as intense in this energy range as the $(\text{CdSe})_{13}(\text{MA})_6$ spectrum.

Finally, in the lower panel in Fig. 3.16 are the spectra included for QDs passivated with DMPDA, DMATP, and URA. DMPDA experiences the strongest red-shift of the spectrum out of all QD-ligand systems presented in this work. Following the argumentation of Frederick *et al.* [31] this should have had happen when ABN passivated the QD surface. Tan *et al.*'s argumentation that the

dimethylamino group as a good electron-donating group stabilizes the delocalized hole due to its electron donating properties matches better with our results.

The first absorption peak for the $(CdSe)_{13}(DMPDA)_6$ system shows up at 2.22 eV. A shoulder at even lower energies, 2.13 eV, indicates optical activity. The peaks located at 2.45, 2.8, and 3.1 eV coincide in the wavelength of the first four peaks of the $(CdSe)_{13}(PTOL)_6$ system. The intensities, however, are very different. Unlike the spectra of the DMPDA and the DMATP ligands in Fig. 3.14, the first absorption peaks of $(CdSe)_{13}(DMPDA)_6$ and $(CdSe)_{13}(DMATP)_6$ do not coincide. It seems as if the different properties of N and S like electronegativity and polarizability do have an important impact on the optical properties of the QDs. The DMATP spectrum shows a first peak at 2.28 eV, which is almost as intense as the shoulder in the DMPDA spectrum at 2.13 eV. The following two peaks are more intense and their location coincide approximately with those in the ABN and PTOL spectra. The most intense absorption feature below 3.5 eV is located at a wavelength of about 3.15 eV. It is with much difference the most intense feature observed below this energy from all the spectra represented.

3.8 Discussion

We have presented an extensive overview related to the simulation of optical absorption spectra of CdSe quantum dots. We tackled technical issues like the choice of basis sets and functionals, also interdot distance, and the influence of a given ligand molecule on the spectrum. We employed 3 cluster sizes ranging from 1 to 2.5 nm. All of them have been reported earlier in theoretical and experimental studies and represent realistic models of CdSe QDs.

Since we used the RT-TDDFT methodology as it is implemented in CP2K we first benchmarked the m-DZVP-SR basis sets that are included in the basis set library of this program against the LR-TDDFT methodology. While the LANL2DZ basis set gives very nice results when optical properties are considered, the bond lengths are generally overestimated. Large basis sets like cc-pVDZ or def2-TZVP do reproduce well geometrical properties of the $(CdSe)_6$ cluster but they induce a clear red-shift when it comes to the calculation of optical spectra. With the m-DZVP-SR basis sets, however, accurate geometrical

properties are obtained, and the simulated optical spectra are reasonably well reproduced.

Additionally, we probed four different functionals for their aptitude to simulate optical spectra. From the two GGA functionals BLYP and PBE, only the latter gives useful results. Spectra calculated with the BLYP functional are considerably shifted to much longer wavelengths. PBE does of course underestimate the band gaps and first absorption peak maxima but it still offers a good compromise between accuracy and computational costs. Out of the two hybrid DFT functionals B3LYP and PBE0 we used here, B3LYP gives indeed very nice results. If it would not be for the computational efforts to calculate optical spectra with it, it would be the functional of choice. PBE0 suffers from its well-known limitations that band gaps and optical spectra are severely overestimated.

The interdot distance that is necessary to obtain a spectrum that does not reflect any unwanted interactions between the QD system and the cell walls (in the case of non-periodic calculations), or interactions between periodic images of a periodic system, is found to be around 6 to 7 Å. At 3 Å artifacts occur, which indicate strong interactions between two QDs as they are separated only by little more than a typical Cd−Se bond.

We observed the size dependence of the spectrum as expected: the larger the cluster diameter the more the spectrum shifts to lower energies, getting closer to the bulk band gap. In addition, the effect of surface passivation is reproduced correctly. Upon adsorption of ligand molecules on the QD surface, the spectrum shifts to higher energies. The spectra of QD-ligand model systems that contain aliphatic ligand molecules do not differ substantially. Only small blue-shifts of < 0.1 eV occur when the methylamine is exchanged with methylthiol, and when the phosphine oxide ligand has shorter aliphatic chains. Also the intensities of the spectra are similar.

Another parameter that influences the optical spectrum of $(CdSe)_{13}$ is which Cd atoms are saturated. The spectrum shifts the most to higher energies if Cd atoms that are only two-coordinated are passivated with one ligand molecule per Cd. It resulted that it not necessary to fully saturate the Cd atoms of the $(CdSe)_{13}$ QD, but only the two-coordinated and those atoms next to them.

Optical absorption becomes more diverse when aromatic molecules are used instead of aliphatic ones. Aniline type ligands, a thiophenol based ligand, and

uracil are employed as representatives of aromatic ligands. The variation of first absorption peak maxima is larger, the energy range is almost as broad as 0.4 eV. The four aniline type ligands have the *para* substituent to the amino group exchanged in order to check if the electron-donating and -withdrawing properties of these substituents influence the optical absorption spectrum. They indeed do, and we find that if the *para* substituent consists of a dimethylamino group, the spectrum is shifted most to lower energies. The nitrile group does not shift considerably more to the blue, it is similar to the spectrum of a system that contains a simple methyl group. This was not anticipated and implies that the Hammett constant does not serve very well as a tool to preliminarily estimate the shift that the *para* substituent could induce. Similar to the aliphatic ligands, the thiophenol type ligand, which contains a dimethylamino substituent, too, is located at slightly higher energies than the equivalent aniline type ligand.

3.9 Bibliography

[1] Liu, L.; Zhuang, Z.; Xie, T.; Wang, Y.-G.; Li, J.; Peng, Q.; Li, Y., *J. Am. Chem. Soc.* **2009**, *131*, 16423.

[2] Xia, X.; Liu, Z.; Du, G.; Li, Y.; Ma, M., *J. Lumin.* **2010**, *130*, 1285.

[3] Manna, L.; Scher, E. C.; Alivisatos, A. P., *J. Am. Chem. Soc.* **2000**, *122*, 12700.

[4] Manna, L.; Wang; Cingolani, R.; Alivisatos, A. P., *J. Phys. Chem. B* **2005**, *109*, 6183.

[5] Scher, E. C.; Manna, L.; Alivisatos, A. P., *Phil. Trans. R. Soc. Lond. A* **2003**, *361*, 241.

[6] Jun, Y.-W.; Lee, S.-M.; Kang, N.-J.; Cheon, J., *J. Am. Chem. Soc.* **2001**, *123*, 5150.

[7] Watt, J.; Yu, C.; Chang, S. L. Y.; Cheong, S.; Tilley, R. D., *J. Am. Chem. Soc.* **2012**, *135*, 606.

[8] Jose, R.; Zhanpeisov, N. U.; Fukumura, H.; Baba, Y.; Ishikawa, M., *J. Am. Chem. Soc.* **2006**, *128*, 629.

[9] Kasuya, A.; Sivamohan, R.; Barnakov, Y. A.; Dmitruk, I. M.; Nirasawa, T.; Romanyuk, V. R.; Kumar, V.; Mamykin, S. V.; Tohji, K.; Jeyadevan, B.; Shinoda, K.; Kudo, T.; Terasaki, O.; Liu, Z.; Belosludov, R. V.; Sundararajan, V.; Kawazoe, Y., *Nat. Mater.* **2004**, *3*, 99.

[10] Kudera, S.; Zanella, M.; Giannini, C.; Rizzo, A.; Li, Y.; Gigli, G.; Cingolani, R.; Ciccarella, G.; Spahl, W.; Parak, W.; Manna, L., *Adv. Mater.* **2007**, *19*, 548.

[11] Wang, Y.; Liu, Y.-H.; Zhang, Y.; Wang, F.; Kowalski, P. J.; Rohrs, H. W.; Loomis, R. A.; Gross, M. L.; Buhro, W. E., *Angew. Chem. Int. Ed.* **2012**, *51*, 6154.

[12] Del Ben, M.; Havenith, R. W. A.; Broer, R.; Stener, M., *J. Phys. Chem. C* **2011**, *115*, 16782.

[13] Botti, S.; Marques, M. A. L., *Phys. Rev. B* **2007**, *75*, 035311.

[14] Nguyen, K. A.; Day, P. N.; Pachter, R., *J. Phys. Chem. C* **2010**, *114*, 16197.

[15] Kilina, S.; Ivanov, S.; Tretiak, S., *J. Am. Chem. Soc.* **2009**, *131*, 7717.

[16] Kilina, S. V.; Kilin, D. S.; Prezhdo, O. V., *ACS Nano* **2009**, *3*, 93.

[17] Kilina, S.; Velizhanin, K. A.; Ivanov, S.; Prezhdo, O. V.; Tretiak, S., *ACS Nano* **2012**, *6*, 6515.

[18] Albert, V. V.; Ivanov, S. A.; Tretiak, S.; Kilina, S. V., *J. Phys. Chem. C* **2011**, *115*, 15793.

[19] Abuelela, A. M.; Mohamed, T. A.; Prezhdo, O. V., *J. Phys. Chem. C* **2012**, *116*, 14674.

[20] Deglmann, P.; Ahlrichs, R.; Tsereteli, K., *J. Chem. Phys.* **2002**, *116*, 1585.

[21] Puzder, A.; Williamson, A. J.; Gygi, F.; Galli, G., *Phys. Rev. Lett.* **2004**, *92*, 217401.

[22] Inerbaev, T. M.; Masunov, A. E.; Khondaker, S. I.; Dobrinescu, A.; Plamada, A.-V.; Kawazoe, Y., *J. Chem. Phys.* **2009**, *131*, 044106.

[23] Klimov, V. I., *J. Phys. Chem. B* **2006**, *110*, 16827.

[24] Yang, P.; Tretiak, S.; Masunov, A. E.; Ivanov, S., *J. Chem. Phys.* **2008**, *129*, 074709.

[25] Yang, P.; Tretiak, S.; Ivanov, S., *J. Clust. Sci.* **2011**, *22*, 405.

[26] de la Fuente, M. S.; Sánchez, R. S.; González-Pedro, V.; Boix, P. P.; Mhaisalkar, S. G.; Rincón, M. E.; Bisquert, J.; Mora-Seró, I., *J. Phys. Chem. Lett.* **2013**, *4*, 1519.

[27] Tan, Y.; Jin, S.; Hamers, R. J., *J. Phys. Chem. C* **2012**, *117*, 313.

[28] Liu, I.-S.; Lo, H.-H.; Chien, C.-T.; Lin, Y.-Y.; Chen, C.-W.; Chen, Y.-F.; Su, W.-F.; Liou, S.-C., *J. Mater. Chem.* **2008**, *18*, 675.

[29] Hyeon-Deuk, K.; Prezhdo, O. V., *J. Phys. Condens. Matter* **2012**, *24*, 363201.

[30] Aldana, J.; Wang, Y. A.; Peng, X., *J. Am. Chem. Soc.* **2001**, *123*, 8844.

[31] Frederick, M. T.; Amin, V. A.; Weiss, E. A., *J. Phys. Chem. Lett.* **2013**, *4*, 634.

[32] Frederick, M. T.; Amin, V. A.; Swenson, N. K.; Ho, A. Y.; Weiss, E. A., *Nano Lett.* **2013**, *13*, 287.

[33] Dimmock, J. O.; Wright, G. B., *Phys. Rev.* **1964**, *135*, A821.

[34] Konior, J.; Goniakowski, J.; Kaprzyk, S., *J. Alloys Compd.* **2001**, *328*, 139.

[35] Bryant, G. W.; Jaskólski, W., *Phys. Rev. B* **2003**, *67*, 205320.

[36] Wuister, S. F.; de Mello Donegá, C.; Meijerink, A., *J. Phys. Chem. B* **2004**, *108*, 17393.

[37] Chung, D. S.; Lee, J.-S.; Huang, J.; Nag, A.; Ithurria, S.; Talapin, D. V., *Nano Lett.* **2012**, *12*, 1813.

[38] Kovalenko, M. V.; Scheele, M.; Talapin, D. V., *Science* **2009**, *324*, 1417.

[39] Kovalenko, M. V.; Bodnarchuk, M. I.; Zaumseil, J.; Lee, J.-S.; Talapin, D. V., *J. Am. Chem. Soc.* **2010**, *132*, 10085.

[40] Kovalenko, M. V.; Schaller, R. D.; Jarzab, D.; Loi, M. A.; Talapin, D. V., *J. Am. Chem. Soc.* **2012**, *134*, 2457.

[41] Liu, W.; Lee, J.-S.; Talapin, D. V., *J. Am. Chem. Soc.* **2012**, *135*, 1349.

[42] Nag, A.; Kovalenko, M. V.; Lee, J.-S.; Liu, W.; Spokoyny, B.; Talapin, D. V., *J. Am. Chem. Soc.* **2011**, *133*, 10612.

[43] Liu, W.; Chang, A. Y.; Schaller, R. D.; Talapin, D. V., *J. Am. Chem. Soc.* **2012**, *134*, 20258.

[44] Nadler, R.; Sanz, J. F., *Theor. Chem. Acc.* **2013**, *132*, 1342.

[45] Isborn, C. M.; Kilina, S. V.; Li, X.; Prezhdo, O. V., *J. Phys. Chem. C* **2008**, *112*, 18291.

[46] Engelhardt, L.; Raston, C.; Whitaker, C.; White, A., *Aust. J. Chem.* **1986**, *39*, 2151.

[47] Dong, C.; Li, X.; Qi, J., *J. Phys. Chem. C* **2011**, *115*, 20307.

[48] Wei, H. H.-Y.; Evans, C. M.; Swartz, B. D.; Neukirch, A. J.; Young, J.; Prezhdo, O. V.; Krauss, T. D., *Nano Lett.* **2012**, *12*, 4465.

[49] Wang, X.; Zeng, Q.; Shi, J.; Jiang, G.; Yang, M.; Liu, X.; Enright, G.; Yu, K., *Chem. Phys. Lett.* **2013**, *568–569*, 125.

[50] Schreuder, M. A.; McBride, J. R.; Dukes, A. D.; Sammons, J. A.; Rosenthal, S. J., *J. Phys. Chem. C* **2009**, *113*, 8169.

[51] Kim, H.-S.; Jang, S.-W.; Chung, S.-Y.; Lee, S.; Lee, Y.; Kim, B.; Liu, C.;

Neuhauser, D., *J. Phys. Chem. B* **2010**, *114*, 471.

4

TiO_2 sensitized with CdSe

TiO_2 and ZnO are the semiconductors that are typically employed as the sensitized material in dye and quantum dot sensitized solar cells. Their large band gap make them a bad solar light absorption material since the lower energy photons in the red, or even infrared, part of the solar light spectrum is not harvested. Quantum dots, which replace dye molecules, step up to fill that gap in order to employ a wider energy range of the solar light. TiO_2 nanoparticles are often used as a model, however, the possibility to calculate optical absorption spectra opens up the modeling of periodic systems like nanotubes. Solar cells where quantum dots are directly adsorbed on TiO_2 nanotubes have been found to be more efficient than in a linker-assisted approach, where an organic, bi-functional molecule links the quantum dot to the semiconductor. Although it is less efficient, the desorption rate of thus linked quantum dots is much slower, therefore, the solar cell has a longer lifetime.

4.1 Introduction

Semiconductor nanostructures like CdSe, CdS, PbSe, and others have become promising candidates to further increase availability and efficiency of third generation solar cells. They are easy to synthesize and, consequently, are available quicker and cheaper. Light absorption can be tuned equally as easy, which enhances the efficiency of such solar cells. Furthermore, their usage offers the production of flexible solar cells, similar to dye sensitized solar cells (DSSC). The only disadvantage is the lower efficiencies compared to DSSCs (which employ efficiencies of 12 % [1]): for quantum dot sensitized solar cells (QDSSCs) that work with liquid electrolytes a power conversion efficiency of 5 % has been reported, however, for solid state QDSSCs, efficiencies arrived at almost 10 % [2–4]. Keep in mind that a few years ago efficiencies of hardly 1–2 % have been reached.

The crucial process of a QDSSC is the injection of the excited electrons from the QD into the conduction band of the TiO_2 electrode. The typical design is that a mesoscopic TiO_2 or ZnO film is adsorbed on an optical transparent electrode (OTE). These films do not exceed a thickness of 10 μm. A QD suspension is then added to these films. Different strategies exist to fabricate QDSSCs. Popular methods are drop or spin coating, chemical bath deposition [5–8], surface ionic layer adsorption and reaction (SILAR) [9–11], electrophoretic deposition [12, 13], and the bi-functional linker approach [14–19].

The linker-assisted attachment of QDs to the mesoscopic semiconductor makes use of the fact that the linker has two functional groups. One of them binds to the TiO_2 surface, usually via a carboxylic acid group, while the second substituent coordinates with the metal atoms in the QD. Typically, these groups are thiols or amines, but following the approach of Tan *et al.* this could also be a dithiocarbamate group [20]. The bi-functional approach has the advantage that aggregation of QDs is avoided as this leads to a significant decrease in the incident photon-to-current efficiency (IPCE). It further allows for submonolayer coverage.

The linker type has a substantial influence on the electron transfer kinetics. Chang *et al.* investigated different mercaptoalkanoic acids (MAAs), which differ in the chain length. CdSe/ZnS core/shell quantum dots that are linked via these linkers to TiO_2, showed that longer chain lengths shorten the fluorescence

lifetime, which was found by other authors, too [21, 22]. They also investigated how the fluorescence lifetime changes when an aromatic linker is included. To do so they employed 4-mercaptobenzoic acid (MBA). Although MBA is about twice as long as the shortest MAA linker, the fluorescence lifetime was much shorter, yielding the fastest electron transfer to TiO_2. The authors attributed this effect to the enhanced electronic coupling through the aromatic structure of MBA. Obviously, this finding is similar to those reports we discussed in §3.1 on page 55 where similar properties of aromatic ligands like PTC and MBA were discussed.

The anchor group of the linker that binds to the semiconductor also influences the ET dynamics. Hyun *et al.* measured the fluorescence decay for PbS QDs that are linked to TiO_2 nanoparticles [22]. The anchor groups were chosen to be carboxylic acid, phosphonic acid, silane, and sulfonic acid functional groups. They found the shortest decay times when the linker is anchored via the sulfonic acid group, where the decay time yielded 2.5 ns, and the slowest decay time was reported to be 77 ns, where the silane group acts as anchor. They could not explain conclusively what effect is responsible for those relatively large differences, but they cited a theoretical study where the authors studied a pyridine molecule that carries a phosphonic and a carboxylic acid anchor [23]. They found that the injection rate depends more on the choice of anchor group rather than on the binding mode of the functional groups. Ultimately, the anchor group plays an important role in the moderation of the electron transfer. As a side note, we would like to mention an article by Vercelli *et al.* who linked CdSe nanoclusters with diamines and hydrazine [24], where the authors found that the photoconductivity in a multilayered structure is highest when the QDs are linked with hydrazine. However, due to the toxicity of hydrazine, ethylenediamine would be the best choice to link the QDs.

An extensive study about anchoring groups through which dye molecules bind to anatase(101) and rutile(110) surfaces of TiO_2 was presented by Ambrosio *et al.* [25]. They identified acetylacetone, hydroxamic acid, catechol, and phosphonic acid as good anchor groups. Phosphonic acid was reported earlier by these authors in the same context [26]. Furthermore, on the anatase surface catechol has the fastest injection rate in its bridging bidentate mode. The hydrogen atoms are donated to the TiO_2 surface.

Medintz *et al.* studied QD–dopamine bioconjugates, which they employed for biolabeling [27]. The electron transfer occurs via a peptide to the dopamine molecule, thereby effectively quenching the QD's photoluminescence. The hydroquinone type structure of dopamine enables the same binding modes to the TiO_2 as does catechol. Additionally it offers the possibility to bind to a QD via the amine group, eventually acting as a linker molecule.

Further, Pernik *et al.* listed a few points that have an impact on the efficiency of a QDSSC [28]. One of the more important point is that the surface of the QDs should be cleaned of any residual phospine oxide ligands that were used during synthesis, referencing to the insulating properties of ligands with long aliphatic tails like TOPO. They also mentioned that direct adsorption of the QDs on TiO_2 shows faster electron injection over CdSe clusters that are linked with mercaptopropionic acid (MPA).

In DSSCs the dye molecules are usually adsorbed on TiO_2 nanoparticles [29]. DSSCs are, however, not limited to employ solely nanoparticles, there are also reports that employed TiO_2 nanotubes as the sensitized material [30–33]. Nanoparticles have to transport the photogenerated charge across a 3-dimensional structure, which is thought to hamper the efficiency of such systems. Nanotubes, on the other hand, are limited the only 1-dimension, therefore, charges are separated much faster.

Obviously, the same strategy can be chosen for the preparation of QDSSCs, too. For instance, Li *et al.* reported that the photocatalytic activity of QD-TiO_2 nanotube heterostructures is higher than a pure QD solution or TiO_2 nanotubes [34]. Other groups reported such QD-TiO_2 nanotube systems also as a possible photovoltaic application [11, 35–42]. The efficiencies of the power conversion is still relatively low; it did not exceed 3 % in these reports. Also theoretically TiO_2 nanotubes sensitized with QDs have been the subject of investigation. A rather minimal $(CdSe)_2$-TiO_2 nanotube system was investigated by Dong *et al.* by means of hybrid DFT calculations [43].

4.2 TiO_2

TiO_2 is a wide gap semiconductor used in dye and quantum dot sensitized solar cells. The bulk band gap of the anatase phase is about 3.15 eV [46], too large to

exploit photons that lie energetically within the ultraviolet and visible (UV/Vis) range of the sunlight. In this section we present results for different TiO_2 systems, which are anatase bulk and surfaces, nanotubes, and nanoparticles.

As discussed in earlier chapters, band gaps, E_g, that are calculated with the PBE functional are underestimated; in contrast, that arising from PBE0 calculations is clearly overestimated. The HSE06 hybrid functional results in slightly better numbers, but the band gaps of TiO_2 systems like nanotubes, for instance, are still overestimated [48]. See also Table 4.1 for more details. A most effective way to circumvent this problem without the necessity of expensive computational methods, is to apply DFT+U [49]. For TiO_2 we use the effective parameter U as it was derived by Deskins and Dupuis using CP2K, which they determined to be 4.1 eV [50, 51].

We first present the results for a bulk system of TiO_2 anatase. The PBE results are within the results that were published earlier. The band gap is 0.2 eV higher than the one reported by Landmann *et al.* [45], but it underestimates the experimental band gap by 1 eV. See Table 4.1 for more details. The optimized PBE lattice parameters, on the other hand, are very close to the experimental values, they differ by as little as a few hundreds of Å. The PBE+U calculation reproduces better the experimental band gap, it is underestimated by 0.2 eV. Furthermore, the experimental lattice parameters are slightly underestimated by PBE+U.

The absorption spectra for the bulk systems are represented in Fig. 4.1, and E_{abs} are tabulated in Table 4.1. Again, the PBE+U first absorption maximum

Method	E_g, [eV]	E_{abs}, [eV]	a, [Å]	c, [Å]
PBE	2.12	2.41	3.776	9.486
PBE+U	2.97	3.30	3.691	9.413
PBE0[a]	4.50	–	3.758	9.704
PBE[b]	1.94	–	–	–
HSE06[b]	3.60	–	–	–
Exp.	3.15[c]	–	3.784[d]	9.515[d]

[a] Reference [44]
[b] Reference [45]
[c] Reference [46]
[d] Reference [47]

TABLE 4.1 Band gaps, E_g, of bulk TiO_2 anatase obtained with different functionals. Also, the unit cell vectors a and c are included. The spectra that correspond to the PBE and the PBE+U results are shown in Fig. 4.1.

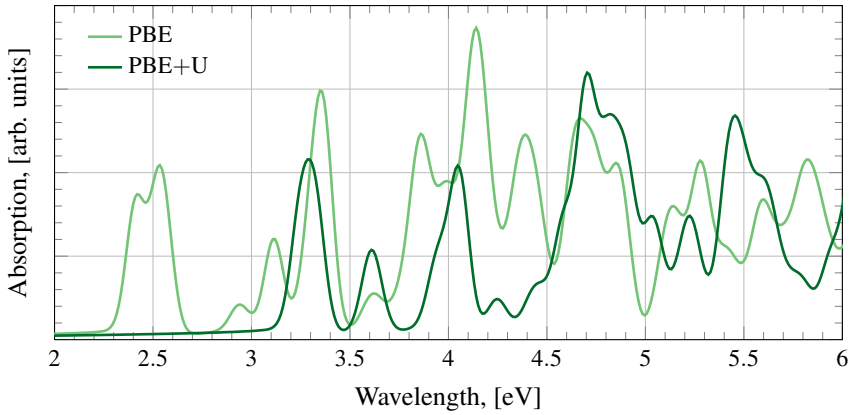

FIG. 4.1 Absorption spectra for TiO_2 anatase bulk calculated with the PBE and the PBE+U methodologies.

is located at a higher energy (3.30 eV) than the pure PBE first absorption peak maximum, which is located at 2.41 eV. Furthermore, the first PBE absorption peak is divided into two subpeaks, whereas the first absorption peak for PBE+U is not. The intensity of both peaks, however, is roughly the same. The PBE+U spectrum illustrated in Fig. 4.1 reproduces nicely the experimental UV–Vis spectrum published by Asahi *et al.* [52] and Zhao and Yu [53] for TiO_2 anatase. In Fig. 4.2 our calculated PBE+U spectrum is shown together with the experimental spectrum reported by Asahi *et al.*. The experimental spectrum of the bulk anatase TiO_2 was obtained by measuring dry-pressed disk samples applying UV–Vis diffuse reflectance spectroscopy, which is the reason for the low resolution of their spectrum in comparison to our calculated spectrum. The first peak starts to raise at roughly 3.18 eV (390 nm) and reaches the maximum height at 3.3 eV (375 nm), similar to the experimental spectrum. Based upon these results, we will apply the PBE+U methodology on the TiO_2 systems in what follows.

Next, we give our attention to the TiO_2 nanotubes. Ferrari *et al.* considered only the $(2n,n)$ and $(0,m)$ rollup vectors to generate 1 ML (101) anatase-type nanotubes [48]. According to them, the $(n,0)$ rollup vector did not produce stable structures. Here, we employ the $(0,m)$ roll-up vector where $m = 8, 12, 16$; consequently, the individual tubes are denominated as NT(0,8), NT(0,12), and

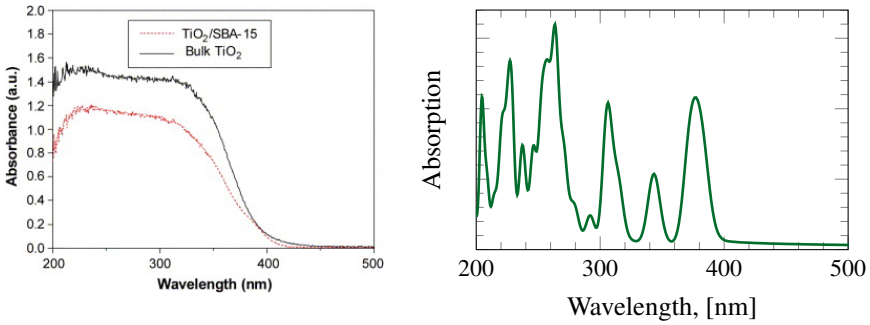

(a) (b)

FIG. 4.2 In (a) is the experimental spectrum represented as it was obtained by Zhao and Yu [53]. This UV–Vis diffuse reflectance spectrum was obtained using the dry-pressed disk samples. In (b) the PBE+U spectrum is illustrated, but this time we use nm as the energy unit to better be able to compare it to the experimental spectrum.

NT(0,16). The geometries and the spectra of these tubes are depicted in Fig. 4.3 and 4.4. This choice of roll-up vectors allows for relatively small nanotubes that can be used as the sensitized material in a theoretical model.

Since some QDs that we employ have larger diameters than others, two different tube lengths are used. Typically, we set the length of the nanotubes to 20.5 Å. In some cases this tube length is too short to include a given cluster, therefore, it is extended to 30.75 Å. The $(Cdse)_{34}$ cluster is an example for such a cluster that needs a longer tube in order to model the QD-nanotube system. However, due to the already large number of atoms that are needed to model the NT(0,12) and NT(0,16), only the smallest NT(0,8) tube will be employed also with a length of 30.75 Å.

In Table 4.2 the band gaps and the first absorption peak maxima are given. Ferrari *et al.* calculated E_g using the PBE0 functional, which is why their results are very large. Apart from this technical difference, we calculated the same band gap energy sequence as in their paper: NT(0,8) has the smallest gap, NT(0,12) the largest, and NT(0,16) lies in-between [48]. Our result for NT(0,8) is in accordance with other literature as well [43, 54].

In Fig. 4.4 are the absorption spectra for the three nanotubes represented, the corresponding first absorption peak maxima are tabulated in Table 4.2. The sequence of E_{abs} is different to the E_g sequence. The lowest excitation en-

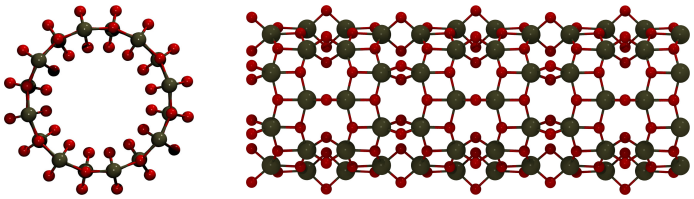

(a) NT(0,8)

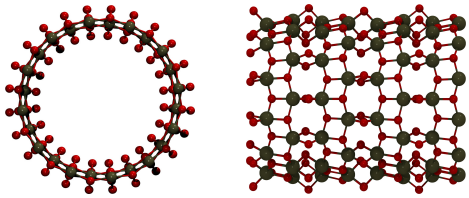

(b) NT(0,12)

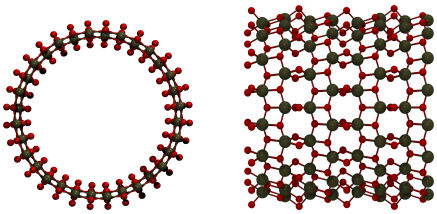

(c) NT(0,16)

FIG. 4.3 The cross-sections and side-views of the three nanotube systems are represented here. In (a) the tube with the smallest diameter in this work is shown, which is labeled NT(0,8). Here, the 30.75 Å long nanotube is shown. In (b) the NT(0,12) nanotube is illustrated. Finally, in (c) the geometry of the largest diameter nanotube is depicted, labeled NT(0,16).

ergy is also attributed to the NT(0,8) tube, while E_{abs} for the NT(0,12) tube is slightly higher. $E_{\text{abs}}^{\text{NT(0,16)}}$ is localized at somewhat higher energies than $E_{\text{abs}}^{\text{NT(0,12)}}$. However, the tube with the largest diameter also shows optical activity right above 4 eV, which is indicated by a shoulder that is about half as intense as the peak at 4.23 eV. While the shoulder is obvious for this system, also the other two systems have such shoulders, although they show either very low intensity (NT(0,8)), or it is hardly noticeable (NT(0,12)). The spectra as they are illustrated in Fig. 4.4 are shifted by about 1 eV to the blue compared to the spectrum presented by Li *et al.* [55]. The higher energy of our results is explained with the smaller diameters of our nanotube systems: here they are between 1.0 and 2.0

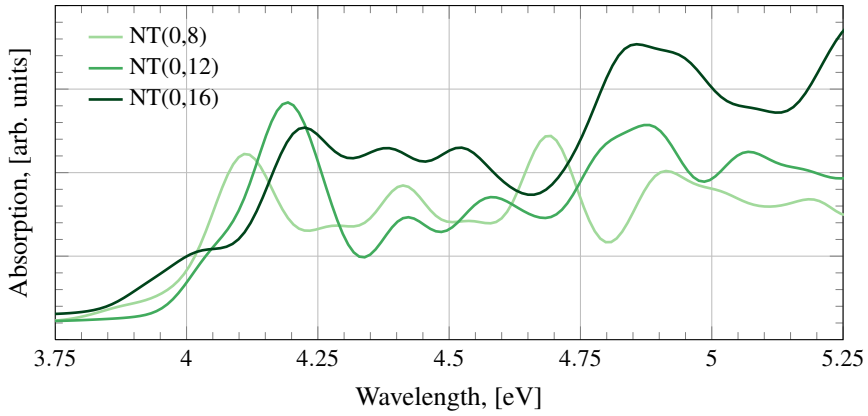

Fig. 4.4 Shown are the optical absortpion spectra of the three nanotube systems as they are illustrated in Fig. 4.3.

nm, whereas Li *et al.* synthesized titanate nanotubes with diameters of 10 nm. All in all, we reproduce well the optical properties of anatase(101) nanotubes.

Apart from the nanotube systems discussed above, we also use a non-periodic $(TiO_2)_{38}$ nanoparticle and sensitize it with CdSe QDs. Its E_g is equal to 2.83 eV, slightly below the corresponding gap for the bulk anatase. The optimized geometry is shown in Fig. 4.5. It is formed by two layers of anatase(101), however, these layers collapse at the edges of the cluster, where most Ti atoms form only 4 bonds to adjacent oxygens. The absorption spectrum for $(TiO_2)_{38}$ represented in Fig. 4.5(a) does not show a distinct first absorption peak maximum, but rather it increases steadily at energies higher than 3 eV. This is 0.5 eV above E_{abs} of the bulk spectrum. The lack of distinct peaks is attributed to the distorted geometry

Tube model	E_g, [eV]	E_{abs}, [eV]
NT(0,8)	3.37	4.11
NT(0,8), PBE0[a]	5.32	–
NT(0,12)	3.78	4.19
NT(0,12), PBE0[a]	5.70	–
NT(0,16)	3.71	4.23
NT(0,16), PBE0[a]	5.64	–

[a] Reference [48]

Table 4.2 Calculated PBE+U band gaps E_g, and first absorption peak maximum E_{abs} of the TiO_2 nanotubes. The corresponding absorption spectra are represented in Fig. 4.4. The spectrum of NT(0,16) shows a shoulder at 4.03 eV.

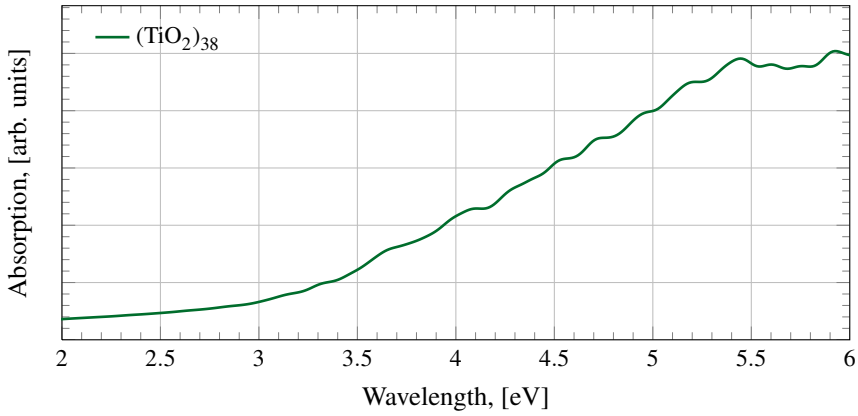

(a) Optical absorption spectrum.

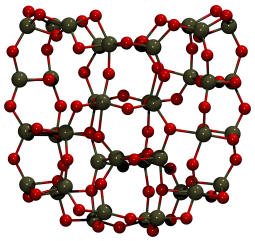

(b) Top view.

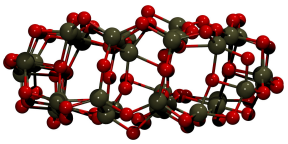

(c) Side view.

FIG. 4.5 The absorption spectrum of $(TiO_2)_{38}$ is shown in (a). Top and side view of the optimized $(TiO_2)_{38}$ cluster are illustrated in (b) and (c), respectively.

of the cluster and unsaturated bonds on the surface, which leads to a manifold of possible excitations.

Finally, in Fig. 4.6 the HOMO and LUMO energy levels of the above presented TiO_2 systems are shown. The $(CdSe)_{13}$ and $(CdSe)_{13}(MA)_6$ clusters, as well as the $(CdSe)_{34}$ cluster, are also included in order to illustrate the relative arrangement of the valence and conduction band edges between QD and semiconductor. The LUMOs of the bare $(CdSe)_{13}$ and $(CdSe)_{34}$ clusters coincide energetically only with the LUMO of the $(TiO_2)_{38}$ nanoparticle.

When it will be combined with nanotubes, the efficiency of such a system will probably be low since an excited electron will more likely recombine with the photogenerated hole within the QD if the electronic wave function of the MO into which the electron is transferred is not spread over the TiO_2 part. This is in

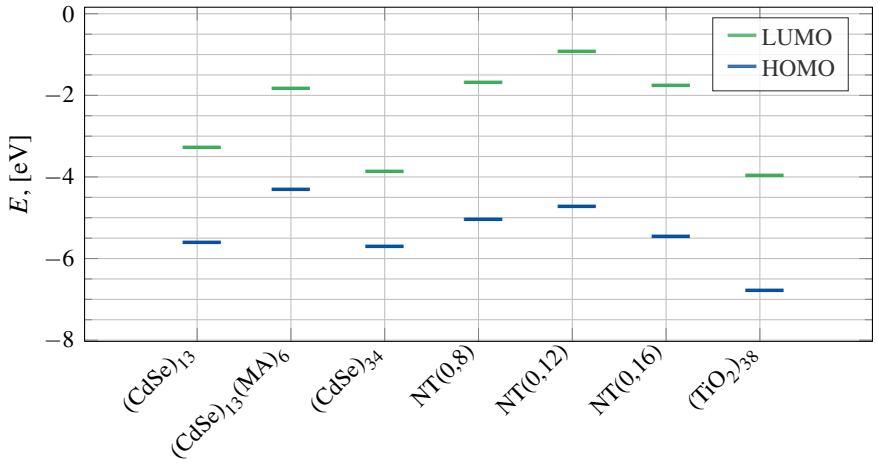

FIG. 4.6 HOMO and LUMO energies of the TiO_2 nanotube systems and the nanoparticle introduced in this section are presented here. Additionally, the $(CdSe)_{13}$ and $(CdSe)_{13}(MA)_6$ clusters are included to demonstrate the relative energy between these MOs.

the spirit of Le Bahers *et al.* who reported that the presence of *tert*-butylpyridine in a DSSC should reduce the rate of electron injection [56], because it alters the electronic structure of the investigated DSSC as such that the LUMO+1 orbital of the dye lies consistently below the CB edge of ZnO. On the other hand, addition of Li^+ ions will enhance the electron transfer rate because the LUMO+1 is shifted well beyond the CB edge of ZnO. The LUMO of the ligated cluster, however, does overlap with the LUMOs of the nanotubes. Consequently, the performance of the cell should be good.

4.3 Linker molecules

Although different studies showed that the efficiency of the electron transfer from the QD to the mesoscopic semiconductor is higher when the QD is adsorbed directly [28, 57], the usage of a linker molecule does have certain advantages like submonolayer coverage, and preventing the QDs to aggregate, which would hamper the solar cell efficiency.

Here, we chose two organic molecules that will link the quantum dots with the TiO_2 structures described earlier. These are 3-mercaptopropionic acid (MPA)

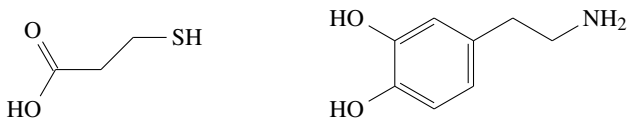

(a) 3-mercaptopropionic acid (MPA)

(b) Dopamine (DA)

FIG. 4.7 The aliphatic linker 3-mercaptopropionic acid is illustrated in (a), while dopamine represents an aromatic-type linker as it is shown in (b).

and dopamine (DA). Both molecules are represented in Fig. 4.7. MPA is a typical linker molecules used in the synthesis of TiO_2 structures with CdSe [28]. DA has a partially aromatic structure. It is used in bio-sensing applications where the photoexcited electron is transferred to it [27]. It belongs to the same family of quinones like catechol, and since catechol is used as a sensitizer in DSSCs, we investigate DA as a possible linker molecule. Another reason that favors the usage of DA is that aromatic linkers lead to enhanced electronic coupling of the QD with TiO_2 [21, 22].

The adsorption mode of catechol has been reported to be the dissociative bidentate adsorption mode [58, 59]. DA adsorbs to the nanotube in the bridging mode only by inducing a strong deformation to the tube, where it obtains rather an ellipsoidal than a circular form. We found that both DA and MPA are adsorbed in a crossed, bidentate adsorption mode on the TiO_2 nanotubes, which is 0.12 eV more stable than the bridging bidentate adsorption mode.

4.4 $(TiO_2)_{38}$ cluster sensitized with CdSe QDs

The $(TiO_2)_{38}$ cluster is the largest cluster that has been employed in a series of articles written by Sánchez-de Armas *et al.* [60, 61]. In these articles they also reported that the $(TiO_2)_6$ cluster is smallest nanocluster model to successfully reproduce the electronic absorption spectra of dye–TiO_2 systems. However, the size relation between a QD and the TiO_2 nanoparticle is matched much better with the larger TiO_2 cluster, which is why we will use it as the sensitized part of the QDSSC model. We consider both MPA and DA as the linker molecules.

In order to check if any interactions between the ligands and the TiO_2 cluster

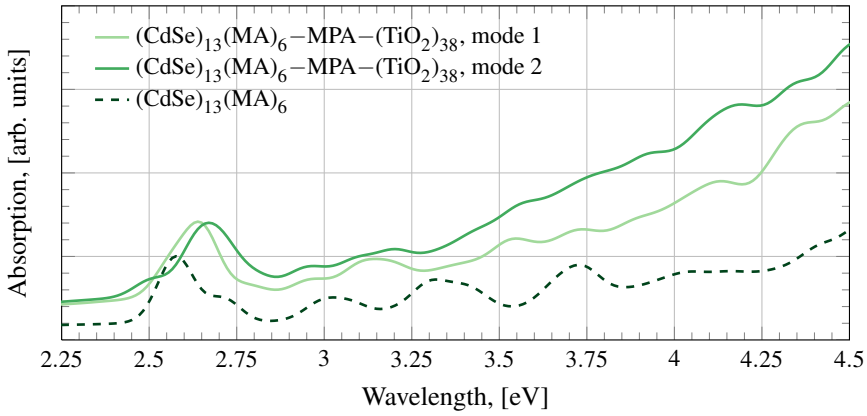

(a)

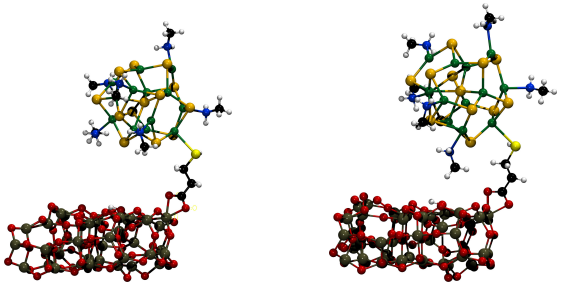

(b) Mode 1 (c) Mode 2

FIG. 4.8 Represented are in (a) the optical absorption spectra of $(CdSe)_{13}(MA)_6$−MPA−$(TiO_2)_{38}$, $(CdSe)_{13}(MA)_6$, and the $(TiO_2)_{38}$ cluster. Mode 1 and 2 refer to the orientation of the QD's ligand molecules with respect to the TiO_2 cluster, see the main text for details. The respective geometries are illustrated in (b) for mode 1, and in (c) for mode 2.

would have an influence on the spectrum, we employed to different modes for the $(CdSe)_{13}(MA)_6$−MPA−$(TiO_2)_{38}$ system. They differ in that for one mode no interaction between the ligand molecules and the TiO_2 cluster occurs (mode 1), whereas for the second mode a weak interaction between one MA ligand and the cluster surface exists (mode 2). Since the ligands contribute only little to the MOs near the valence band edge and the LUMO, which is shown in Table 3.4 on page 71 for the aliphatic ligands and in Table 3.6 on page 78 for the aromatic ligands, it is not expected that this type of interaction between ligand molecules

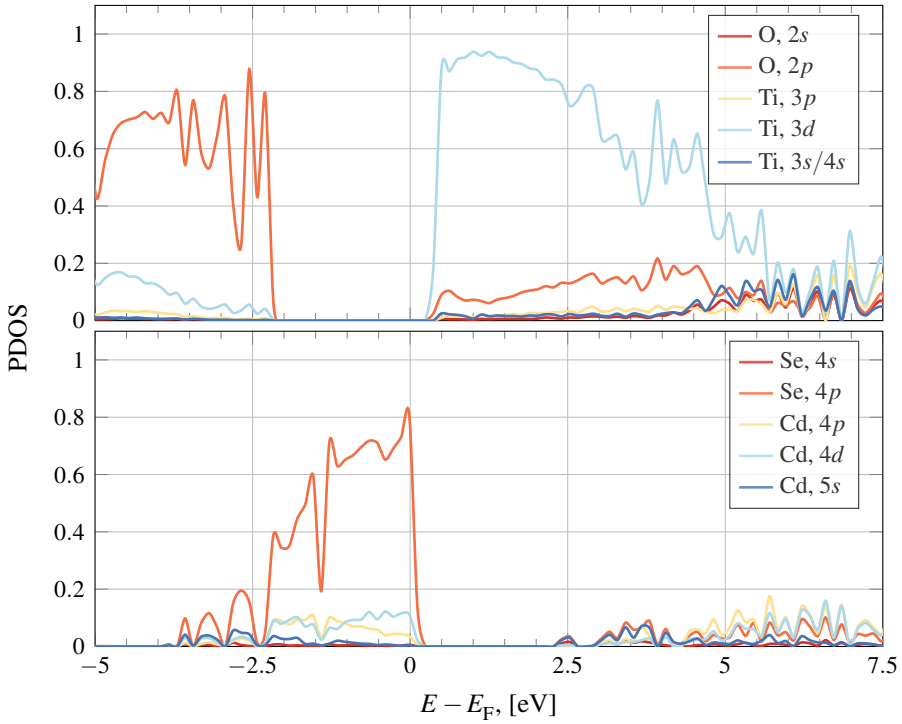

FIG. 4.9 Partial DOS of $(CdSe)_{13}(MA)_6$−MPA−$(TiO_2)_{38}$.

and the TiO_2 surface has an important influence on the energetically lowest lying optical transitions.

The calculated spectra for both modes and the optimized geometry are represented in Fig. 4.8. A look at the two spectra makes it clear immediately that ligand-TiO_2 cluster interaction does not substantially alter the spectrum. The first absorption peak maximum is located at a slightly higher wavelength when the ligand interacts with the TiO_2 cluster, the peak itself is a little bit broader, and a small peak forms at almost 3 eV. But these changes are too small as that we would have to take care of them; consequently, we are not concerned about such interactions for other systems that we will calculate.

If we compare the $(CdSe)_{13}(MA)_6$−MPA−$(TiO_2)_{38}$ spectrum to the one obtained for the $(CdSe)_{13}(MA)_6$ QD, then we observe a small blue-shift of the first absorption peak from 2.58 to 2.64 eV. This is in contrast to the red-shift that is observed when alizarin is adsorbed on TiO_2 clusters [58, 60]. Optical activity,

however, occurs also at lower wavelengths: in the QD-TiO_2 model it is indicated by a small shoulder that is located at the energy where the QD spectrum has the first E_{abs} maximum. On the other hand, in the QD spectrum a shoulder is observed near to where the $(CdSe)_{13}(MA)_6$−MPA−$(TiO_2)_{38}$ spectrum has it first absorption peak maximum. Up to 3.5 eV the spectra are formed mainly by the absorption features correlated to the CdSe cluster, above 3.5 eV the TiO_2 cluster contributes to the spectrum as well, which leads to a higher intensity of the spectrum compared to both the isolated QD and TiO_2 clusters.

Although E_{abs} is 2.64 eV, the band gap, E_g, for this system is effectively 0.51 eV. As can be seen in Fig. 4.9, the HOMO and the VB are formed by the orbitals of the QD, while the LUMO and the CB consist of orbitals from the $(TiO_2)_{38}$ cluster. Only about 2 eV above the CB edge, CdSe does contribute to the CB, too, which is favorable in terms of an efficient electron transfer from the QD to the TiO_2 cluster.

The TiO_2 gap is 2.83 eV, whereas the CdSe gap is about 2.48 eV. These band edges found for the CdSe as well as for the TiO_2 part are basically the same as for the independent systems. The PDOS for $(CdSe)_{13}(MA)_6$ part, which is illustrated in the lower panel in Fig. 4.9, reveals that it did not change substantially compared to the PDOS of the isolated cluster (c.f. Fig. 3.10 on page 70). The single peak at the CB edge still exists, and the Se $4p$ orbitals make the largest contribution to the VB. Therefore, the inclusion of a QD as the sensitizing system does not change the relative order of the MOs of the individual parts of the system.

From the optical absorption spectrum in Fig. 4.8, the PDOS in Fig. 4.9, and the band gap of the system, it becomes clear that the electron transfer is of indirect type. This is reasoned with the fact that the first absorption peak corresponds more to band gap of the isolated QD rather than to the band gap of the total system.

What happens if the MPA linker is exchanged for a dopamine molecule? The spectra that are represented in Fig. 4.10 reveal that when the linker molecule is exchanged the resulting spectrum differs a lot. Suddenly, below 2.5 eV optical activity occurs, which does not show up when MPA links the QD to $(TiO_2)_{38}$. Furthermore, the band gap of the DA linked system becomes suddenly zero.

To reveal the origin of this optical activity, the absorption spectrum of the

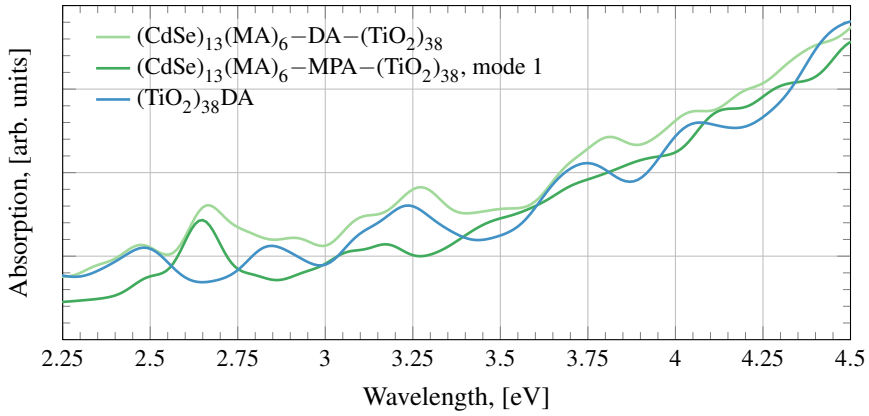

FIG. 4.10 Optical spectrum of the DA linked $(CdSe)_{13}(MA)_6$−DA−$(TiO_2)_{38}$ system. Apart from the spectrum of the system that uses the MPA linker in Fig. 4.8, the spectrum of a DA molecule adsorbed on the $(TiO_2)_{38}$ cluster is also included.

$(TiO_2)_{38}$DA system is included in the same figure. Obviously, it is related to the adsorption of the aromatic DA molecule on the TiO_2 cluster since both spectra resemble each other very much. There is one absorption peak at 2.6 eV that is not present in the spectrum of $(TiO_2)_{38}$DA, but which is present in the spectrum of $(CdSe)_{13}$−MPA−$(TiO_2)_{38}$ and $(CdSe)_{13}(MA)_6$−DA−$(TiO_2)_{38}$, therefore, we assign it to the first absorption peak that takes place in the QD. In the DA linked system it is even slightly more intense than when MPA is the employed linker.

The DA's aromaticity and the symmetry of its π-orbitals make it possible that the electron wave function extends better over the whole system. In Fig. 4.11 the HOMOs and the LUMOs of both the MPA and the DA linked systems are illustrated. There it can be seen that in general the HOMO is localized more on the QD, whereas the LUMO is found for large parts on the TiO_2 cluster. Although this is basically true for both models, this effect is more pronounced for $(CdSe)_{13}(MA)_6$−MPA−$(TiO_2)_{38}$, and less when DA is the linker. In the latter system, a different effect occurs. Here, the π-orbitals of the linker molecule are part of the HOMO and the LUMO, effectively bridging the QD and the TiO_2 cluster. This does not occur when MPA links the two clusters. DA has as well an aliphatic part, which coordinates with the amine group to the QD. It would be interesting to see what influence a linker molecule like mercaptobenzoic acid would have on the optical properties and on the frontier MOs of the QD–linker–

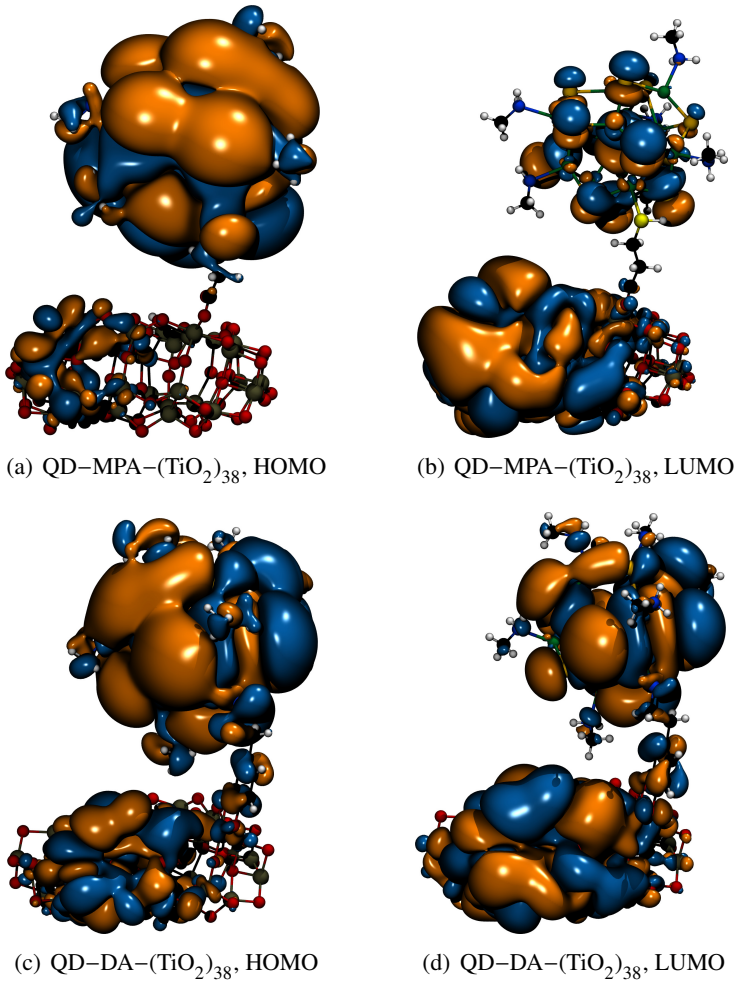

(a) QD−MPA−$(TiO_2)_{38}$, HOMO

(b) QD−MPA−$(TiO_2)_{38}$, LUMO

(c) QD−DA−$(TiO_2)_{38}$, HOMO

(d) QD−DA−$(TiO_2)_{38}$, LUMO

FIG. 4.11 Illustrated are the HOMOs and LUMOs of the $(CdSe)_{13}(MA)_6$ cluster linked to $(TiO_2)_{38}$. In (a) and (b) the HOMO and the LUMO, respectively, of the MPA linked QD are represented, while in (c) and (d) the HOMO and the LUMO of the DA linked QD are shown. For the isosurfaces an isovalue of $\pm 10^{-3}$ is applied.

TiO_2 system.

In Fig. 4.12 the PDOS of the DA linked system is presented. Additionally to the Cd, Se, Ti and O orbitals that we use to illustrate the electronic properties of the system around the band gap, we include the $2p$ orbitals of dopamine's O, C, and N atoms in the lowest panel. Also, a portion of the Ti $3d$ orbital between

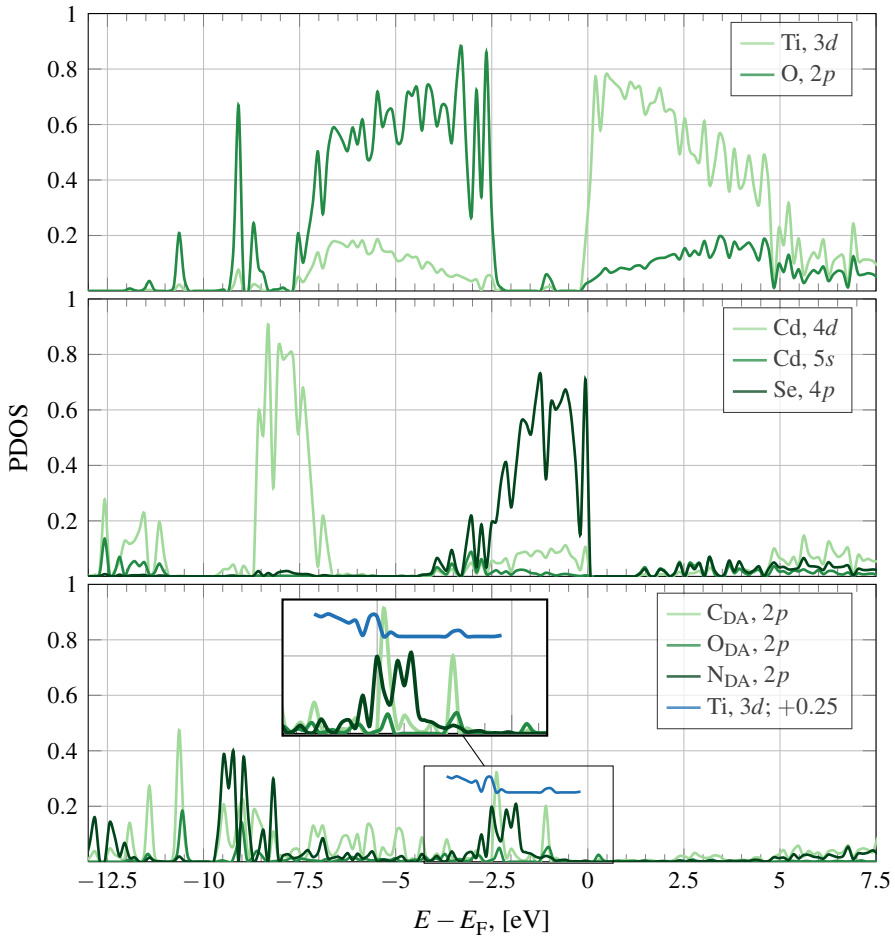

FIG. 4.12 Partial DOS for the DA linked system. In the lowest panel, PDOS of the C, O, and N atoms that form the dopamine linker are represented. For better illustration, the Ti $3d$ orbitals are shifted along the y-axis. The inset in the lowest panel shows a magnified portion of the orbitals for better representation.

−2.6 and 0 eV is included as well. It is shifted as such that it is not covered by the remaining plots. The dopamine O atoms form a bond with the Ti atoms, which is indicated through the relatively strong peak at −2.5 eV that occurs in the O_{DA} $2p$ plot. The band at −2.0 eV consists of O and C $2p$ orbitals, these are certainly the π bonds in DA. Nitrogen shows a peak for its $2p$ orbitals at −1.6 eV. Carbon does not contribute anything to the MO at this energy, neither $2p$ nor

the 2*s* orbitals, which are not included in this figure. Therefore, this molecular orbital reflects the Cd−N bond since the Cd 4*d* and 4*p* orbitals, where the latter is also not included in the figure, contribute to this MO. It results a situation where the DA linker forms part of the VB. The linker, however, is not part of the CB, at least not near the band edge. Only at energies as high as 4 eV, C 2*p* orbitals show considerable contribution to the unoccupied MOs in that energy range.

At this point it would be extremely interesting to see if and how the different linker molecules have an influence on the kinetics of the electron transfer. Two scenarios seem reasonable. First, the fact that DA leads to an electron wave function that is extended over the whole system, could be interpreted in a way that an aromatic linker facilitates the electron transfer. However, the optical activity below 2.5 eV, induced by the interaction between DA and TiO_2, indicates that a second possible scenario is possible, too: that the DA–TiO_2 complex is also optically active and as such lifts the predictability of the first absorption peak of QDs, which is inherently related to the size of a given QD.

There exists a methodology developed by Chen *et al.* where the photo-induced electron transfer is estimated [62]. This includes also the transfer from the excited system, in our case when the photogenerated electron is localized on the QD, to the TiO_2 part. However, the calculations are computationally extremely demanding. Apart from that, to the best of our knowledge, the method is not yet implemented in any computational code.

4.5 TiO_2 nanotubes sensitized with CdSe QDs

In this section we present the results for TiO_2 nanotube systems that are sensitized with bare or ligated CdSe clusters. We first start with the smallest NT(0,8) tube, which, due to its size, is the nanotube that we used the most in this work. To it, results obtained for QDs that sensitize NT(0,12) and NT(0,16) nanotubes are added to round off the picture of quantum dot sensitized TiO_2 nanotubes.

For the NT(0,8) three different QD–NT models are employed. One, where one bare $(CdSe)_{13}$ cluster is added to the tube, which is illustrated in Fig. 4.13(a). The second system is then modeled by linking one $(CdSe)_{13}(PTOL)_6$ cluster via the MPA linker to NT(0,8), as it is shown in Fig. 4.13(b). The third QD–NT

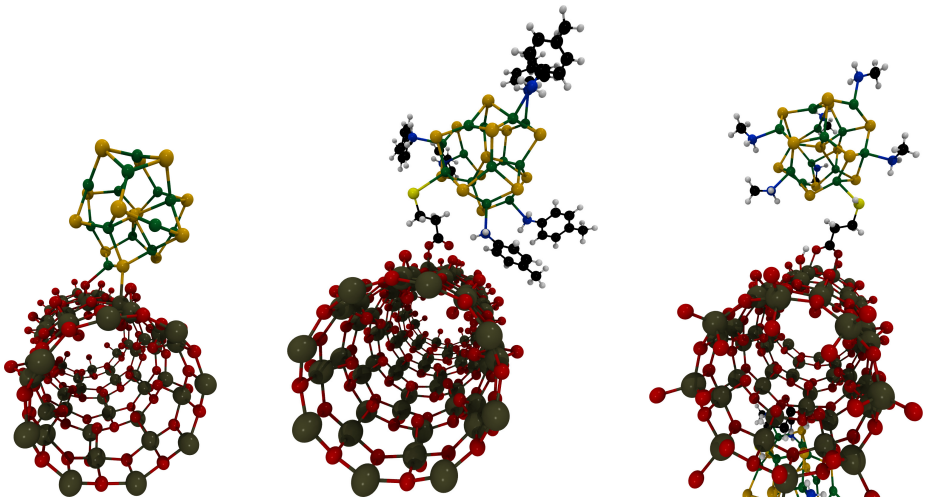

(a) (b) (c)

FIG. 4.13 In (a) and (b) are the geometries represented of $(CdSe)_{13}$−NT(0,8), and of $(CdSe)_{13}(PTOL)_6$−MPA−NT(0,8), respectively. Finally, in (c) the geometry of $((CdSe)_{13}(MA)_6$−MPA$)_2$−NT(0,8) is shown, however, only one QD is included in the figure, which is indicated by the carboxylic anchor group at the bottom of the figure.

model consists of two $(CdSe)_{13}(MA)_6$ QDs that are also linked with a MPA molecule to the nanotube. Its geometry is represented in Fig. 4.13(c).

Similar to the QD–TiO_2 cluster systems, the VB of CdSe lies within the band gap of the TiO_2 nanotube, and the CB edge of the TiO_2 part reaches into the band gap of the QD. This can be observed again for the $(CdSe)_{13}$−NT(0,8) system in Fig. 4.14. The band gap for the total system is 1.62 eV, see also Table 4.3. Since the CdSe cluster is adsorbed directly on the tube, certain hybridization of the MOs of the two parts manifests. While the Ti 3*d* and the O 2*p* orbitals of $(CdSe)_{13}$−MPA−$(TiO_2)_{38}$ does not show any indication that they contribute to any MO right above the TiO_2 VB edge, the contrary is the case for the present QD–NT system. Even though the contribution is small, it is observable between −1.8 and −1.0 eV, indicating that the direct adsorption of the QD on the nanotube does alter the electronic wave function of the single atomic species. Although these states are small, it might be that through them additional excitonic relaxation channels open up, which could either be bad or good. It would be bad if charge carrier recombination would occur; good, if it

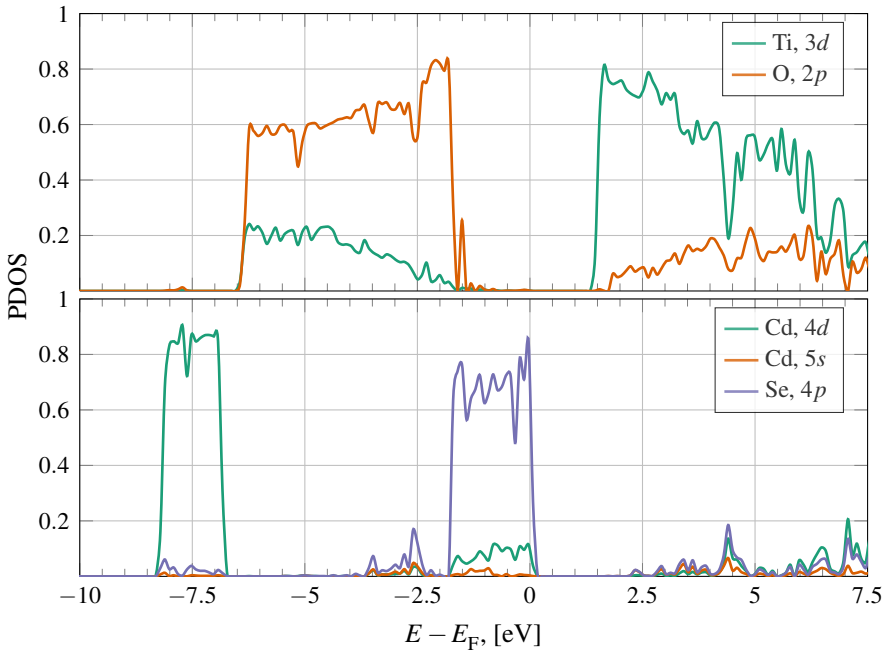

FIG. 4.14 Represented are the PDOS of $(CdSe)_{13}$−NT(0,8). The upper panel shows the PDOS of the Ti $3d$ and the O $2p$ orbitals, while in the lower panel the corresponding $4d$ and $5s$ orbitals for Cd as well as the $4p$ orbitals for Se are plotted.

would serve as a transfer channel of the excited electron towards the nanotube [28, 57]. Unfortunately, and as indicated already at the end of §4.4, we are not in the position to comment on these assumptions since we did not perform any calculations that would confirm or refute either of these hypothesis.

Also the $(CdSe)_{13}$−NT(0,8) model, much like the $(CdSe)_{13}$−MPA−$(TiO_2)_{38}$ model, has the CdSe CB edge located close to 2.5 eV, which is again within the TiO_2 CB. This is about the same energy where the bare $(CdSe)_{13}$ cluster has the CB edge. The optical absorption spectrum for this model system is illustrated in Fig. 4.15. A blue-shift of roughly 0.05 eV occurs upon adsorption of the QD on the nanotube. This phenomenon is also observed when the saturated $(CdSe)_{13}$ cluster is linked to the TiO_2 nanoparticle via the MPA and DA linkers. Furthermore, one sees that the NT(0,8) spectrum, which is indicated with a black, dashed line, does not overlap with the part of the CdSe cluster below energies of 3.5 eV, which actually is the most interesting part of the spectrum as this is the

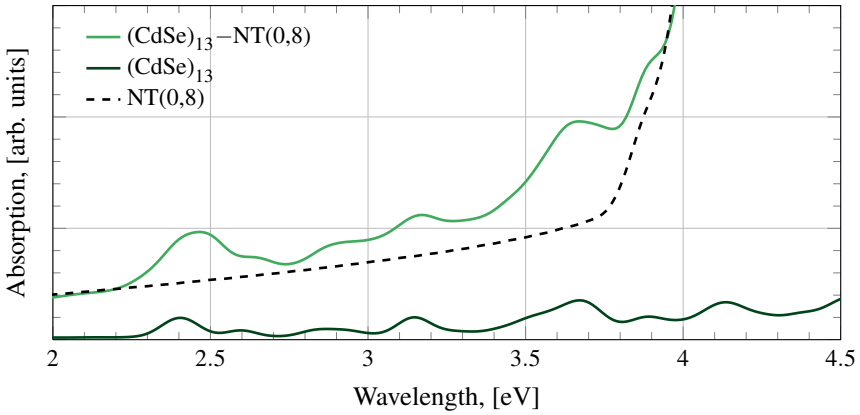

Fig. 4.15 Shown are the optical absorption spectra for the $(CdSe)_{13}$−NT(0,8) system and for the single QD as well.

UV/Vis range of the solar light.

As can be seen in Fig. 3.15 on page 77, the VB and CB edges of $(CdSe)_{13}(MA)_6$ are 1.3 eV higher in energy than that of the bare QD. This is almost the size of the band gap of the $(CdSe)_{13}$−NT(0,8) model. Since the tube remains the same, one could speculate that the band gap of the $((CdSe)_{13}(MA)_6$−$MPA)_2$−NT(0,8) system will be small. Indeed, this is what can be observed in Fig. 4.16: the VB, which consists again mainly of Cd and Se orbitals, and the CB, which has the main contribution from the Ti 3*d* orbitals, are both lying closer to the Fermi level, and the band gap $E_g = 0.71$ eV.

Table 4.3 Band gaps, E_g, and first absorption peak maxima, E_{abs}, of the different QD–NT systems.

Method	E_g, [eV]	E_{abs}, [eV]
$(CdSe)_{13}$−NT(0,8)	1.62	2.45
$((CdSe)_{13}(MA)_6$−$MPA)_2$−NT(0,8)	0.71	2.68
$(CdSe)_{13}(PTOL)_6$−MPA−NT(0,8)	0.71	2.66
$(CdSe)_{34}$−NT(0,8)	1.81	2.02
$(CdSe)_{34}$−MPA−NT(0,8)	1.67	1.87
$((CdSe)_{13})_2$−NT(0,12)	1.62	2.45
$((CdSe)_{13}$−$MPA)_4$−NT(0,16)	0.94	2.43

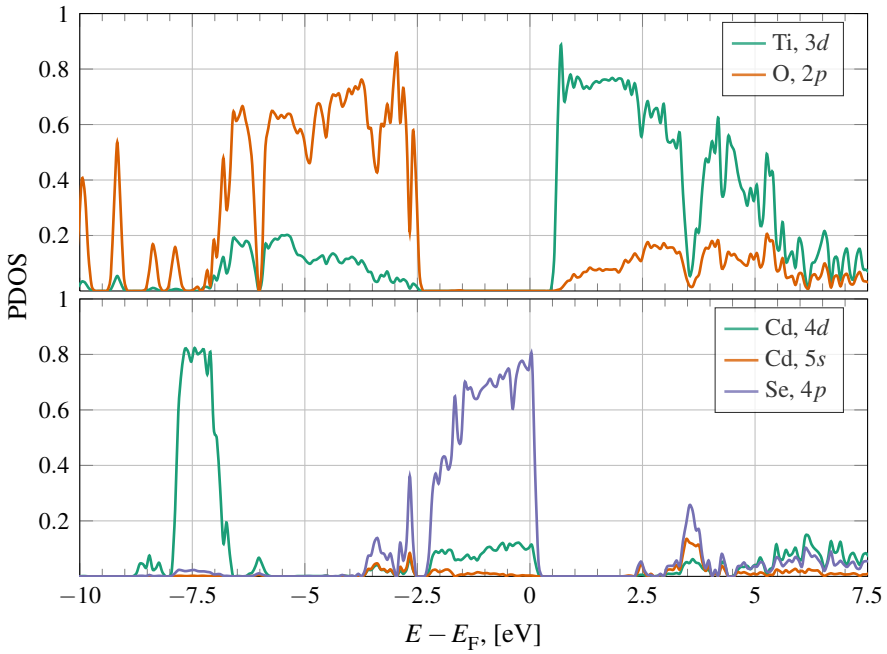

FIG. 4.16 Represented are the PDOS of $((CdSe)_{13}(MA)_6{-}MPA)_2{-}NT(0,8)$. The upper panel shows the PDOS of the Ti $3d$ and the O $2p$ orbitals, while in the lower panel the corresponding $4d$ and $5s$ orbitals for Cd as well as the $4p$ orbitals for Se are plotted.

Apart from the height of the bands, the contribution of the Cd and Se atomic orbitals to the valence and conduction bands in Fig. 4.16 reproduce closely those of the isolated QD in the second panel of Fig. 3.10. The effect of the MPA linker on the electronic structure of the QD-NT(0,8) system is the same as in the $(TiO_2)_{38}$ case: it avoids that any mixed states between CdSe and TiO_2 occur. Below 2.5 eV, neither Cd nor Se orbitals do significantly add to the MOs. Therefore, between the Fermi level and 2.5 eV the MOs are localized only on the TiO_2 nanotube.

The MOs that correspond to those VB and CB edges of the total system, as well as to those bands that are formed by the CdSe cluster at 2.5 eV, are represented in Fig. 4.17. The HOMO-1 and the HOMO resemble to the HOMO of the $(CdSe)_{13}{-}MPA{-}(TiO_2)_{38}$ cluster, where the main part of the orbital is also localized on the QD. However, while for the $(CdSe)_{13}{-}MPA{-}(TiO_2)_{38}$ model part of the HOMO extends also over the TiO_2 nanoparticle, for the QD–NT(0,8)

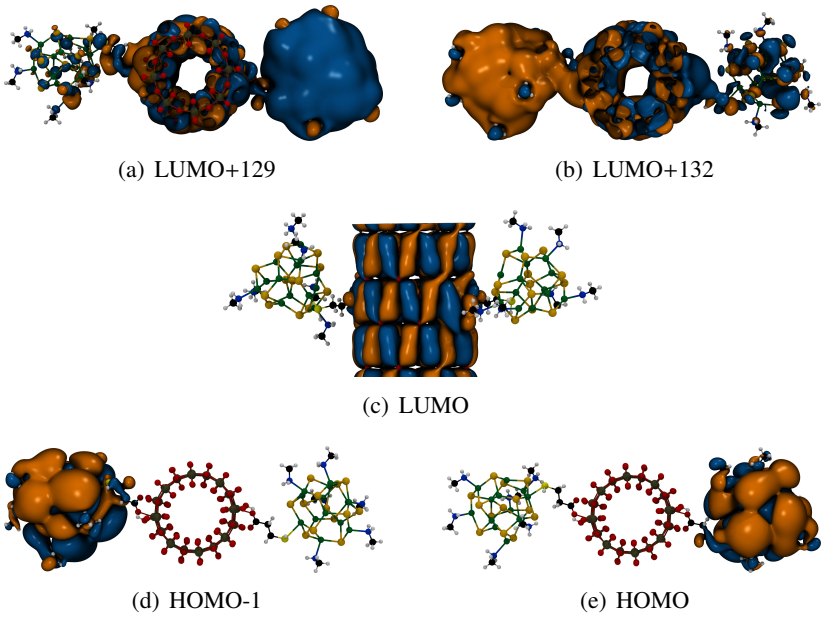

(a) LUMO+129 (b) LUMO+132

(c) LUMO

(d) HOMO-1 (e) HOMO

FIG. 4.17 Illustrated are the LUMO+129 and LUMO+132, respectively, in (a) and (b). These molecular orbitals correspond to the band at around 2.5 eV in the lower panel of the PDOS in Fig. 4.16. The LUMO is represented in (c), while the HOMO-1 and HOMO are shown in (d) and (e). The orientation and the view angle is the same for all graphics except the LUMO. For the isosurfaces an isovalue of $\pm 10^{-3}$ is applied.

system it shows up solely on the CdSe clusters. It is furthermore interesting to note that the HOMO and the HOMO-1 are located on either QD; both MOs do not extend over the two CdSe clusters, as can be seen in Fig. 4.17(e) and Fig. 4.17(d), respectively. Similarly, the LUMO extends solely over the tube. Both features reflect what is observed in the PDOS in Fig. 4.16: the VB edge is formed by Cd and Se orbitals, whereas the CB closest to the Fermi level constitutes of Ti and O orbitals.

The situation is different if the LUMO+129 and the LUMO+132 are considered, which are represented in Fig. 4.17(a) and 4.17(b). As just mentioned, these MOs belong to the bands that occur at around 2.5 eV. Here, the orbitals extend not only over one CdSe cluster, but rather they extend over the whole nanotube, and partially over the second CdSe cluster as well. However, this contribution is rather small. Both MOs are basically degenerate; the energy difference between

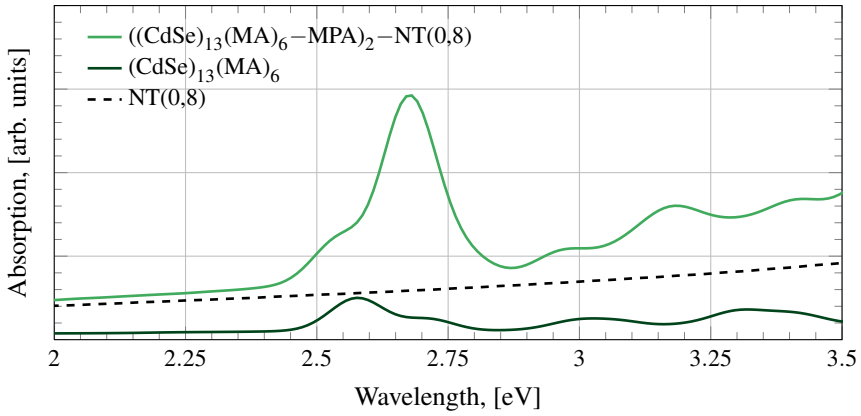

FIG. 4.18 Illustrated are the optical absorption spectra for the $((CdSe)_{13}(MA)_6-MPA)_2-NT(0,8)$ system, and for the isolated $((CdSe)_{13}(MA)_6$ cluster.

them is 0.012 eV.

Also for the $((CdSe)_{13}(MA)_6$ cluster a blue-shift of the first absorption peak maximum is observed. It is, however, stronger than it was for the directly adsorbed, unsaturated cluster; the shift is found to be 0.1 eV. The main peak in $((CdSe)_{13}(MA)_6-MPA)_2-NT(0,8)$, which is located at 2.68 eV, is preceded by a small shoulder at an energy of roughly 2.55 eV. This coincides with the first absorption peak of the isolated cluster. It seems as if the inclusion of a linker molecule makes it energetically more expensive to excite this system compared to the bare cluster which was adsorbed directly on the nanotube. Although the blue-shift for the $((CdSe)_{13}(MA)_6-MPA)_2-NT(0,8)$ model in absolute numbers is not large, it is twice as much when related to the $(CdSe)_{13}-NT(0,8)$ system.

Similar results are found for the $(CdSe)_{13}(PTOL)_6-MPA-NT(0,8)$ model system, for which the optimized geometry is shown in Fig. 4.13(b). The PDOS are included in Fig. 4.19. One can easily see that these DOSes do not change qualitatively when compared those in Fig. 4.16. The band gap of the TiO_2 nanotube is the same, also the bands that correspond to this part of the system are very similar. The main difference to the graphs in Fig. 4.16 is that the CB formed by the QD are less intense.

In Fig. 4.20 is the optical spectrum of $(CdSe)_{13}(PTOL)_6-MPA-NT(0,8)$ illustrated. Interestingly, the comparison of Figures 4.18 and 4.20 reveals that the

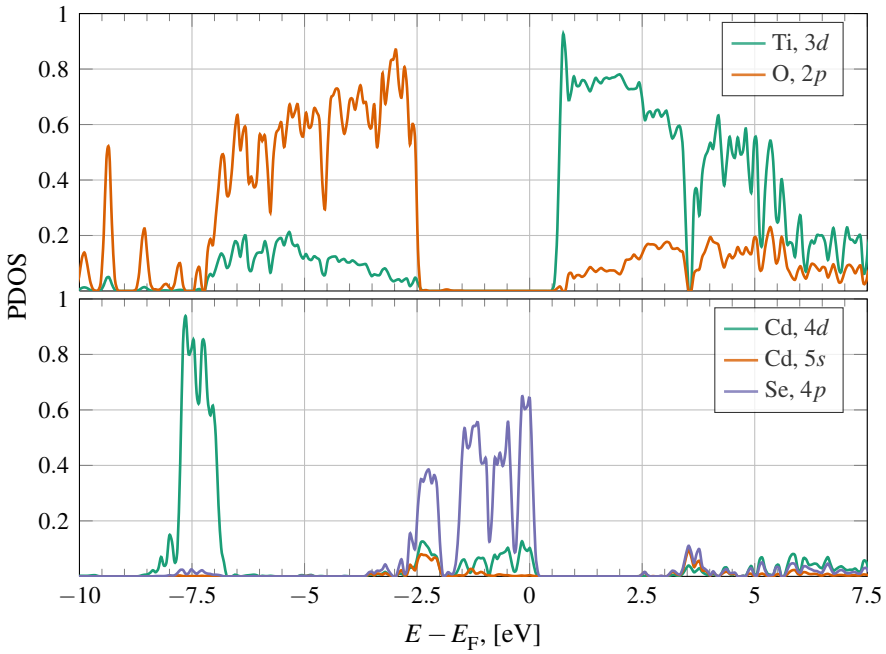

FIG. 4.19 Represented are the PDOS of $(CdSe)_{13}(PTOL)_6$−MPA−NT(0,8). The upper panel shows the PDOS of the Ti $3d$ and the O $2p$ orbitals, while in the lower panel the corresponding $4d$ and $5s$ orbitals for Cd as well as the $4p$ orbitals for Se are plotted.

first absorption peak maximum of the $(CdSe)_{13}(PTOL)_6$−MPA−NT(0,8) spectrum is located at the same wavelength as the first absorption peak maximum of $((CdSe)_{13}(MA)_6$−$MPA)_2$−NT(0,8). If the spectra of the two isolated clusters are compared, however, the first absorption peak maximum of $(CdSe)_{13}(PTOL)_6$ has an energy 0.13 eV below that of $(CdSe)_{13}(MA)_6$. The effect of linking the QD and the nanotube with MPA is that the two spectra are aligned with respect to the first absorption peak maxima, independently on what kind of ligands passivate the QD surface.

The next QD model that sensitizes the NT(0,8) nanotube is the naked $(CdSe)_{34}$ cluster. Two systems are modeled, one where the QD is adsorbed directly on the tube, for which the optimized geometry is shown in Fig. 4.21(a); and one that is linked with the MPA linker, as it is represented in Fig. 4.21(b). The H atom of the MPA linker is adsorbed next to the adsorption site of the linker. The length of either nanotube is 30.75 Å in order to avoid interactions

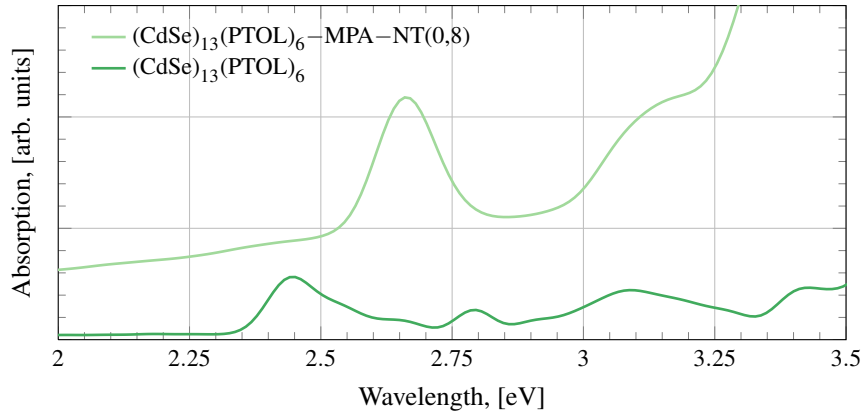

FIG. 4.20 Shown are the optical absorption spectra for the $(CdSe)_{13}$−NT(0,8) system and for the single QD as well.

between the periodic images of the QDs along the tube axis.

The earlier presented systems where saturated and unsaturated $(CdSe)_{13}$ clusters were adsorbed on the NT(0,8) showed that the band gap of the total system is wider if the unsaturated cluster is adsorbed directly on the tube. Since no unsaturated cluster was adsorbed via the MPA linker, it is not clear if the band gap decrease observed in $((CdSe)_{13}(MA)_6-MPA)_2-NT(0,8)$ and $(CdSe)_{13}(PTOL)_6-MPA-NT(0,8)$ occurs due to the linker or because the dangling bonds on the Cd surface atoms are saturated. Since the $(CdSe)_{34}$ cluster is modeled without saturating ligands in both systems, we are now in the position to clarify the ambigous results presented above for the $(CdSe)_{13}$ clusters.

Fig. 4.22(a) shows the PDOS of the $(CdSe)_{34}$−NT(0,8) system where the QD is directly adsorbed, and in Fig. 4.22(b) the PDOS of $(CdSe)_{34}$−MPA−NT(0,8) is illustrated. From these graphs it becomes clear that the MPA linker is not the cause for the smaller band gap in the $((CdSe)_{13}(MA)_6-MPA)_2-NT(0,8)$ and $(CdSe)_{13}(PTOL)_6-MPA-NT(0,8)$ models compared to the $(CdSe)_{13}-MPA-NT(0,8)$ model. The PDOS in Fig. 4.22(b) shows also a smaller band gap. For the MPA linked model E_g = 1.67 eV, when the QD adsorbs directly on the tube it results E_g = 1.81 eV. Since the only difference between these models is the MPA linker, the linking molecule does narrow the band gap and induces a change in the electronic structure of the QD-NT system. Analogically

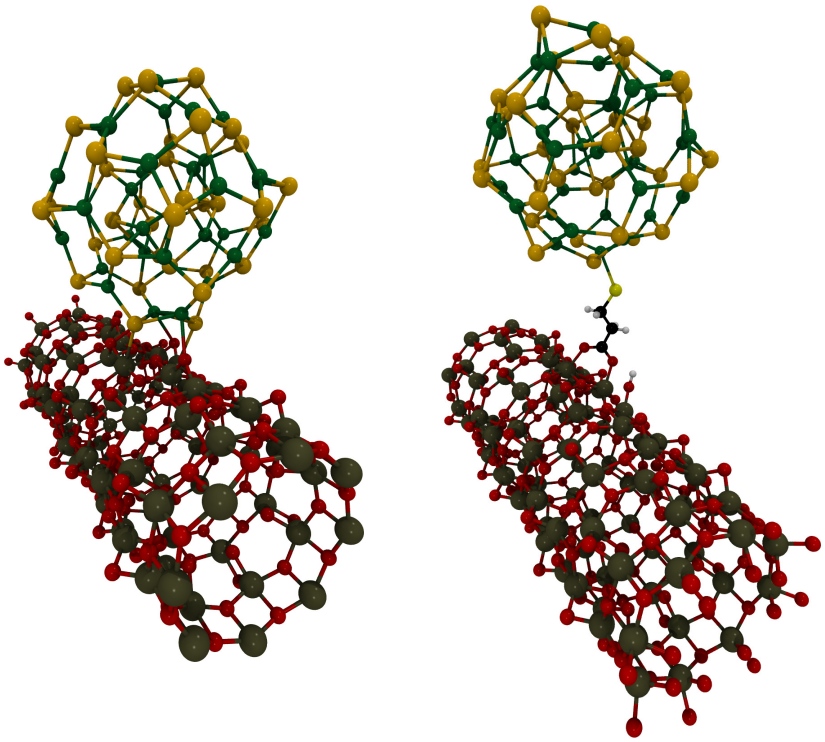

(a) (b)

FIG. 4.21 In (a) is illustrated the optimized geometry of $(CdSe)_{34}$−NT(0,8), and in (b) the one of $(CdSe)_{34}$−MPA−NT(0,8).

to the band gap discussion, also the several states in the band gap of the TiO_2 part are observed in Fig. 4.22(a). As discussed above, these states occur only due to the interactions of the bare QD with the TiO_2 nanotube, since in both systems the cluster is naked.

Earlier we mentioned that the LUMO of the QD should be above the CB of the TiO_2, citing the work of Le Bahers *et al.* [56]. We also presented in Fig. 4.6 HOMO and LUMO energies of TiO_2 systems and $(CdSe)_{34}$. Since in that figure the LUMO of this QD is clearly below the CB of any of the TiO_2 nanotube systems, it is likely that it will not be suitable as a sensitizer of these tubes. Indeed, the PDOS in Fig. 4.22(a) reveal that the CB edge of the CdSe part is below the CB edge of NT(0,8). Obviously, the interaction between $(CdSe)_{34}$ and the NT(0,8) leads to a destabilized CB on the TiO_2 tube, which is stronger here than

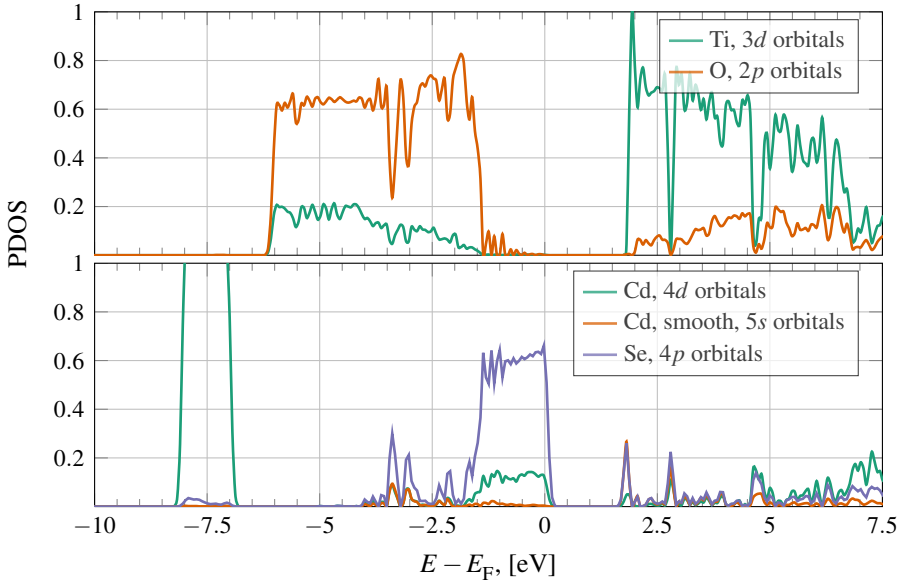

(a) $(CdSe)_{34}$–NT(0,8)

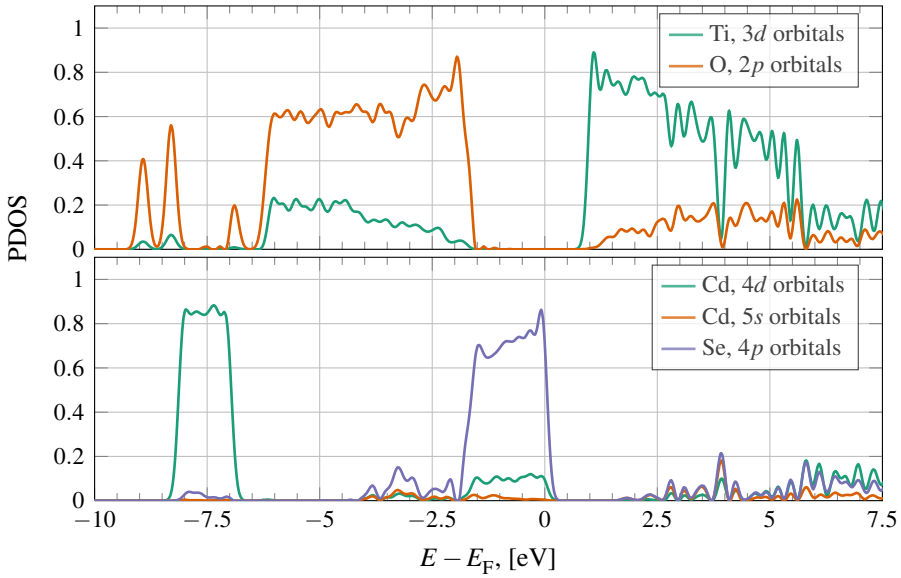

(b) $(CdSe)_{34}$–MPA–NT(0,8)

FIG. 4.22 Represented are in (a) the PDOS of the $(CdSe)_{34}$ QD adsorbed directly on the NT(0,8), as it is illustrated in Fig. 4.21(a). In (b) is shown the PDOS of the $(CdSe)_{34}$–MPA–NT(0,8) QD-NT model as it is depicted in Fig. 4.21(b).

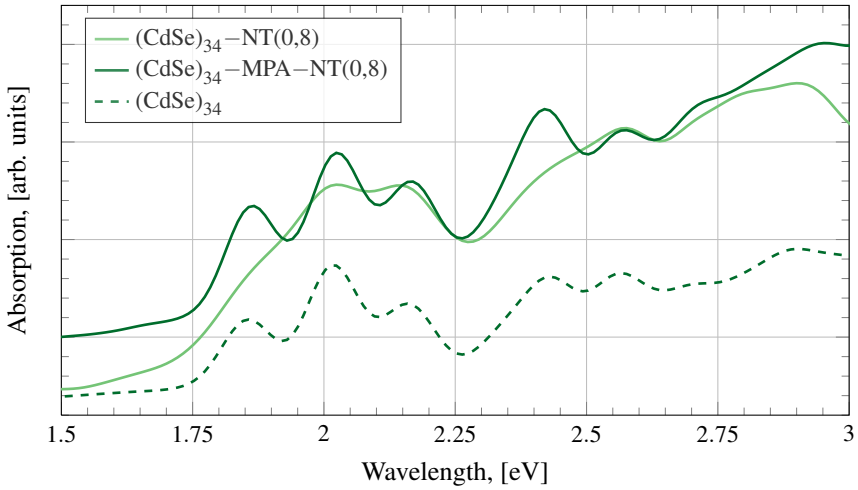

FIG. 4.23 Illustrated are the spectra of $(CdSe)_{34}$−NT(0,8) and $(CdSe)_{34}$−MPA−NT(0,8). For better comparison, the spectrum of the $(CdSe)_{34}$ QD is included also. The inset shows a magnified portion of the spectrum where the lowest lying optical activity of the QDs usually occurs.

in the $(CdSe)_{13}$−NT(0,8) model. What also leads to a CdSe CB edge below that of the TiO_2 nanotube is the smaller band gap of the $(CdSe)_{34}$ cluster compared to the $(CdSe)_{13}$ QD. If the QD is linked with the MPA linker, the NT(0,8) CB is much more stabilized compared to the systems where the QD is directly adsorbed on the nanotube. This is observed for both systems, $(CdSe)_{13}$−NT(0,8) and $(CdSe)_{34}$−NT(0,8).

The spectra of the $(CdSe)_{34}$ clusters that are adsorbed directly or via the MPA linker to the NT(0,8) nanotube are illustrated in Fig. 4.23. Unlike the $(CdSe)_{13}$−NT(0,8) systems, no blue-shift occurs here when compared to the spectrum of the isolated cluster; the spectra for the $(CdSe)_{34}$−NT(0,8) and $(CdSe)_{34}$−MPA−NT(0,8) models start to gain intensity at the same energy as the isolated cluster. Also the higher lying absorption features between 2.25 and 2.75 eV do not shift in both models upon adsorption on, or linkage to, the TiO_2 nanotube. The spectrum of the $(CdSe)_{34}$ cluster that is adsorbed directly on the nanotube, however, looses almost completely the characteristic structure of the bare $(CdSe)_{34}$ cluster spectrum. The first three peaks of this spectrum turn into one broad peak centered at 2 eV. This occurs although the electronic structure of

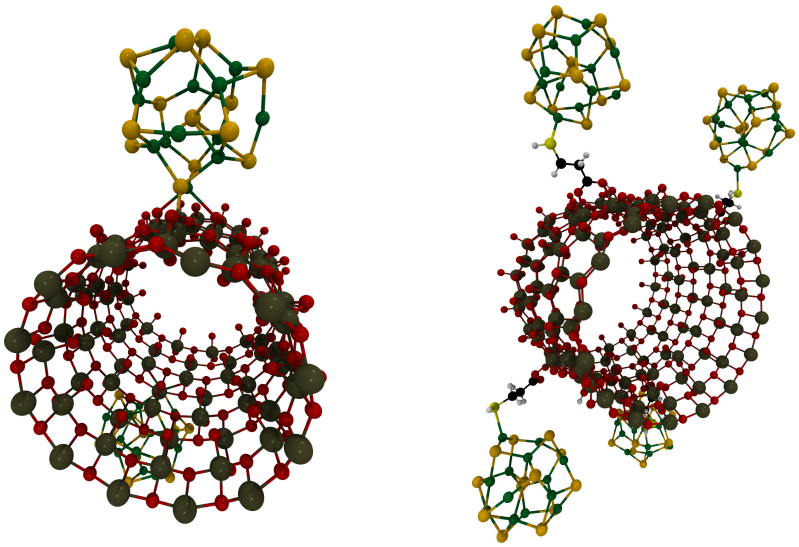

(a) (b)

FIG. 4.24 Illustrated are the geometries of the $((CdSe)_{13}-MPA)_2-NT(0,12)$ and $((CdSe)_{13}-MPA)_4-NT(0,16)$ model.

both models does not change consistently, as is seen in Fig. 4.22(a) and 4.22(b).

In the last part of this section, we present results of two QD-NT systems, where naked $(CdSe)_{13}$ clusters are adsorbed on or linked to the larger NT(0,12) and NT(0,16) nanotubes. On the smaller NT(0,12) nanotube, two bare QDs are directly adsorbed on the nanotube, whereas on the NT(0,16) tube 4 bare clusters are linked via the MPA linker. The geometries are presented in Fig. 4.24(a) and 4.24(b), respectively. We do not include the PDOS of these systems as it would not contribute anything new to the already discussed systems.

Eventually, we present the optical absorption spectra of these systems. The corresponding graphs are shown in Fig. 4.25, together with the spectrum of the bare $(CdSe)_{13}$ cluster. In this figure, one observes the blue-shift again that occurs for all the $(CdSe)_{13}-NT(0,8)$ systems presented so far, independently if they were directly adsorbed or linked with MPA. Since the two $(CdSe)_{34}-NT(0,8)$ models do not show such blue-shifts, we could speculate that only the smaller QDs see their first absorption peak maxima shifting to higher energies. A possible explanation is that the electronic structure of the larger clusters is not as

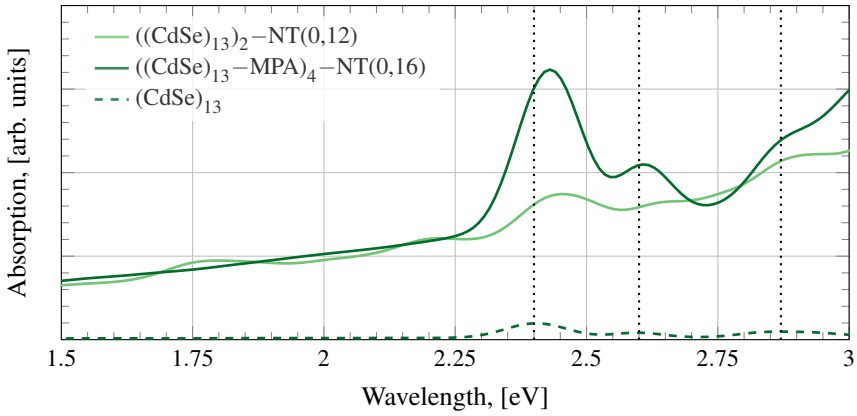

FIG. 4.25 Spectra of $((CdSe)_{13})_2$−NT(0,12) and $((CdSe)_{13}$−$MPA)_4$−NT(0,16) are illustrated. The spectrum of the isolated bare $(CdSe)_{13}$ cluster is included as well. The black dashed vertical lines indicate the first 3 absorption features as they occur in the spectrum of $(CdSe)_{13}$.

strongly affected by the adsorption on the TiO_2 nanostructure as the one of the small clusters.

A different size dependency is observed also for the intensity of the spectrum. But here it involves only the number of clusters included in the model. For instance, the lower intensity observed in Fig. 4.25 for the $(CdSe)_{13}$−NT(0,12) spectrum when compared to the larger system that contains 4 CdSe clusters, is a consequence of the smaller number of QDs included in the system. As a result the intensity is noticeably smaller because the dipoles of the 2 QDs are weaker than those of the 4 CdSe cluster linked to NT(0,16).

The absorption spectrum of $((CdSe)_{13})_2$−NT(0,12) reveals an absorption feature below the supposed first absorption peak maximum of $(CdSe)_{13}$. However, this peak is very weak compared to first absorption peak at 2.45 eV, and it is attributed to the direct adsorption of the QD on the TiO_2 nanotube. Since this adsorption mode leads to states in the band gap of the TiO_2 part, this mode and the energetically lower lying absorption feature are probably related.

The $((CdSe)_{13}$−$MPA)_4$−NT(0,16) system does reproduce the first absorption peak maximum of the $(CdSe)_{13}$ cluster, similar to the other QD–NT systems that use the MPA linker to connect the $(CdSe)_{13}$ cluster with the TiO_2 nanotube. From Fig. 4.25 a small blue-shift of 0.1 eV occurs for both the first

absorption peak maximum as well as for the second, similar to the $((CdSe)_{13}(MA)_6{-}MPA)_2{-}NT(0,8)$ and $(CdSe)_{13}(PTOL)_6{-}MPA{-}NT(0,8)$ models that also experienced such blue-shifts of the same size. As can be seen, the shift is independent on the number of the QDs linked to the nanotube.

4.6 Discussion

In this chapter, we extended the simulation of optical absorption from the isolated QDs to TiO_2 systems that are sensitized with some of the beforehand investigated CdSe clusters. Putting them together results in a system that models quite realistically a QDSSC. We first showed that the electronic and optical properties of the TiO_2 models only are reproduced satisfactorily within the chosen level of theory. The nanotubes reveal some diameter dependent shifts of the band gaps and the first absorption peak maxima. While the E_{abs} shift linearly with increasing tube diameter, the same cannot be said for the E_{g}. Here, $E_{\mathrm{g}}^{\mathrm{NT(0,16)}}$ lies between the band gaps of NT(0,8) and NT(0,12), where the tube with the smallest diameter has the band gap at the shortest wavelength out of these three nanotube models.

The two modes for the $(CdSe)_{13}(MA)_6{-}MPA{-}(TiO_2)_{38}$ model further reveal that the interaction of the ligands, which passivate the QD, with the surface of the TiO_2 nanoparticle does not alter the optical spectrum, at least not the MA ligands. This is important to note since these passivating ligands are important to increase the solar cell efficiency by saturating the defect surface states. Furthermore, we find from analyzing PDOS and optical spectra of QDs on TiO_2 systems, that the electron transfer is of indirect type.

Upon addition of the QD to the TiO_2 semiconductor, the electronic structure of the CdSe and the TiO_2 parts does not substantially change when they are compared to their respective isolated counterpart. However, if the CdSe clusters are adsorbed directly on the TiO_2 system, the electronic structure does change: the orbitals of the CdSe clusters and the TiO_2 models interact and as a consequence, several band states occur in the energy ranges where the TiO_2 system has its band gap. Since earlier reports indicate that the excited electron transfer occurs faster, we suppose that this direct interaction introduces ways to faster transport the electron from the QD, on which the LUMOs are mainly localized, to the

TiO_2. Furthermore, the direction adsorption mode also leads to a destabilization of the TiO_2 CB. In the case of the larger $(CdSe)_{34}$ cluster, the destabilization is stronger, and, due to the lower lying LUMO of the isolated cluster, the CdSe CB edge is even lying below the CB edge of NT(0,8). As it was pointed out in earlier reports, this situation is highly undesired since the electron transfer to the nanotube becomes inefficient. A direct consequence of this is that the band gaps of these systems become larger by about 0.7 to 0.9 eV, depending on the system, as compared to the MPA linked clusters.

The MPA and the dopamine linker separate effectively the two parts of the QD–NT system. This manifests in the PDOS, where no states are observed in the gaps of the respective system. Also, the VB edge of the total systems is formed mainly by the CdSe clusters, while the CB edge is formed by the TiO_2 part. This is nicely observed in the graphical representations of the MOs. The effect was stronger for the QD–NT(0,8) model: the HOMO-1 and the HOMO were completely localized on the CdSe clusters, while the LUMO was only found on the NT(0,8). For the $(CdSe)_{13}(MA)_6$−MPA−$(TiO_2)_{38}$ system, this separation was not observed as strongly. Here, the TiO_2 nanoparticle contributes consistently to the HOMO, whereas the CdSe cluster also adds in some contribution to the LUMO. For the DA linked system, the contribution of the TiO_2 cluster to the HOMO, and the QDs contribution to the LUMO is even higher. The aromatic system of DA facilitates to extend the electronic wave function of the HOMO and the LUMO over the whole QD–NT model.

Another important effect of the MPA linker is that when the QD is linked with it to a TiO_2 nanotube, the CB edge of the TiO_2 part of the system is consistently stabilized, especially when compared to the models where the QD is directly adsorbed. Furthermore, MPA lifts the different first absorption peak maxima of the isolated QDs that are saturated with MA and PTOL ligands. As soon as the clusters are linked to the nanotubes, all models have roughly the same first absorption peak maximum.

Direct adsorption of QDs has an observable influence on the absorption spectrum. For instance, the three first absorption peak maxima at the lower end of the $(CdSe)_{34}$ spectrum go over into one broad peak when the QD is adsorbed on the TiO_2 NT(0,8); the typical optical absorption structure observed for the isolated cluster and the $(CdSe)_{34}$−MPA−NT(0,8) model is lost. If the

same cluster is linked with MPA to the same nanotube, these features are preserved. For the $((CdSe)_{13})_2$−NT(0,12) system, a absorption peak occurs at a lower energy than that of the first absorption peak maximum.

A feature that is only observed for the smaller $(CdSe)_{13}$ clusters, but not for the $(CdSe)_{34}$ cluster, is that their first absorption peak maxima blue-shifts by up to 0.1 eV. This goes along nicely with the work of [55], where they adsorbed CdS and ZnS QDs on TiO_2 nanotubes, and the resulting spectra of the QD–NT systems also show only a slight blue-shift compared to the QD spectra only. This is not seen at all in the spectra of the $(CdSe)_{34}$ clusters adsorbed on the NT(0,8) tubes.

Analyzing the spectra of the differently sized models, we can safely state that it is not necessary to model systems as large as the $((CdSe)_{13}$−$MPA)_4$−NT(0,16) model. There, the large tube implies that more than one QDs are included in order to enhance the relation of the peak heights that belong to the CdSe clusters to the high intensity peaks that are formed by the 400+ atom NT(0,16) nanotube. All in all we can say that the spectrum of the QD–TiO_2 systems simulated in this chapter resemble those of the pure QD systems in the visible range of the light. Above it, TiO_2 does also show the typical absorption features of TiO_2-based system, but they are not as interesting to us because they are lying outside of the UV/Vis range of the solar light spectrum. Eventually, we showed that the RT-TDDFT can be successfully applied to periodic systems as well.

4.7 Bibliography

[1] Yella, A.; Lee, H.-W.; Tsao, H. N.; Yi, C.; Chandiran, A. K.; Nazeeruddin, M.; Diau, E. W.-G.; Yeh, C.-Y.; Zakeeruddin, S. M.; Grätzel, M., *Science* **2011**, *334*, 629.

[2] Ip, A. H.; Thon, S. M.; Hoogland, S.; Voznyy, O.; Zhitomirsky, D.; Debnath, R.; Levina, L.; Rollny, L. R.; Carey, G. H.; Fischer, A.; Kemp, K. W.; Kramer, I. J.; Ning, Z.; Labelle, A. J.; Chou, K. W.; Amassian, A.; Sargent, E. H., *Nat. Nano* **2012**, *7*, 577.

[3] Kim, H.-S.; Lee, C.-R.; Im, J.-H.; Lee, K.-B.; Moehl, T.; Marchioro, A.; Moon, S.-J.; Humphry-Baker, R.; Yum, J.-H.; Moser, J. E.; Gratzel, M.; Park, N.-G., *Sci. Rep.* **2012**, *2*, 591.

[4] Lee, M. M.; Teuscher, J.; Miyasaka, T.; Murakami, T. N.; Snaith, H. J., *Science*

2012, *338*, 643.

[5] Gorer, S.; Hodes, G., *J. Phys. Chem.* **1994**, *98*, 5338.

[6] Niitsoo, O.; Sarkar, S. K.; Pejoux, C.; Rühle, S.; Cahen, D.; Hodes, G., *J. Photochem. Photobiol., A* **2006**, *181*, 306.

[7] Diguna, L. J.; Shen, Q.; Kobayashi, J.; Toyoda, T., *Appl. Phys. Lett.* **2007**, *91*, 023116.

[8] Switzer, J. A.; Hodes, G., *MRS Bull.* **2010**, *35*, 743.

[9] Nicolau, Y., *Appl. Surf. Sci.* **1985**, *22–23, Part 2*, 1061.

[10] Nicolau, Y. F.; Dupuy, M.; Brunel, M., *J. Electrochem. Soc.* **1990**, *137*, 2915.

[11] Baker, D. R.; Kamat, P. V., *Adv. Funct. Mater.* **2009**, *19*, 805.

[12] Islam, M. A.; Herman, I. P., *Appl. Phys. Lett.* **2002**, *80*, 3823.

[13] Brown, P.; Kamat, P. V., *J. Am. Chem. Soc.* **2008**, *130*, 8890.

[14] Robel, I.; Subramanian, V.; Kuno, M.; Kamat, P. V., *J. Am. Chem. Soc.* **2006**, *128*, 2385.

[15] Leschkies, K. S.; Divakar, R.; Basu, J.; Enache-Pommer, E.; Boercker, J. E.; Carter, C. B.; Kortshagen, U. R.; Norris, D. J.; Aydil, E. S., *Nano Lett.* **2007**, *7*, 1793.

[16] Mora-Seró, I.; Giménez, S.; Moehl, T.; Fabregat-Santiago, F.; Lana-Villareal, T.; Gómez, R.; Bisquert, J., *Nanotechnology* **2008**, *19*, 424007.

[17] Lopez-Luke, T.; Wolcott, A.; Xu, L.-p.; Chen, S.; Wen, Z.; Li, J.; De La Rosa, E.; Zhang, J. Z., *J. Phys. Chem. C* **2008**, *112*, 1282.

[18] Guijarro, N.; Lana-Villarreal, T.; Mora-Seró, I.; Bisquert, J.; Gómez, R., *J. Phys. Chem. C* **2009**, *113*, 4208.

[19] Watson, D. F., *J. Phys. Chem. Lett.* **2010**, *1*, 2299.

[20] Tan, Y.; Jin, S.; Hamers, R. J., *J. Phys. Chem. C* **2012**, *117*, 313.

[21] Chang, Y.-P.; Tsai, P.-Y.; Lee, H.-L.; Lin, K.-C., *Electroanalysis* **2013**, *25*, 1064.

[22] Hyun, B.-R.; Bartnik, A. C.; Sun, L.; Hanrath, T.; Wise, F. W., *Nano Lett.* **2011**, *11*, 2126.

[23] Nilsing, M.; Persson, P.; Ojamäe, L., *Chemical Physics Letters* **2005**, *415*, 375.

[24] Vercelli, B.; Zotti, G.; Berlin, A., *J. Phys. Chem. C* **2011**, *115*, 4476.

[25] Ambrosio, F.; Martsinovich, N.; Troisi, A., *J. Phys. Chem. Lett.* **2012**, *3*, 1531.

[26] Ambrosio, F.; Martsinovich, N.; Troisi, A., *J. Phys. Chem. C* **2011**, *116*, 2622.

[27] Medintz, I. L.; Stewart, M. H.; Trammell, S. A.; Susumu, K.; Delehanty, J. B.; Mei, B. C.; Melinger, J. S.; Blanco-Canosa, J. B.; Dawson, P. E.; Mattoussi, H., *Nat. Mater.* **2010**, *9*, 676.

[28] Pernik, D. R.; Tvrdy, K.; Radich, J. G.; Kamat, P. V., *J. Phys. Chem. C* **2011**, *115*, 13511.

[29] O'Regan, B.; Grätzel, M., *Nature* **1991**, *353*, 737.

[30] Zhu, K.; Neale, N. R.; Miedaner, A.; Frank, A. J., *Nano Lett.* **2007**, *7*, 69.

[31] Roy, P.; Kim, D.; Lee, K.; Spiecker, E.; Schmuki, P., *Nanoscale* **2010**, *2*, 45.

[32] Pan, X.; Chen, C.; Zhu, K.; Fan, Z., *Nanotechnology* **2011**, *22*, 235402.

[33] Pastore, M.; De Angelis, F., *Phys. Chem. Chem. Phys.* **2012**, *14*, 920.

[34] Li, X.; Liu, L.; Kang, S.-Z.; Mu, J.; Li, G., *Catal. Commun.* **2012**, *17*, 136.

[35] Hsu, M.-C.; Leu, I.-C.; Sun, Y.-M.; Hon, M.-H., *J. Cryst. Growth* **2005**, *285*, 642.

[36] Kukovecz, A.; Hodos, M.; Kónya, Z.; Kiricsi, I., *Chem. Phys. Lett.* **2005**, *411*, 445.

[37] Kim, M.; Ahn, S.; Jang, D.-J., *J. Nanosci. Nanotechnol.* **2006**, *6*, 180.

[38] Gao, X.-F.; Sun, W.-T.; Ai, G.; Peng, L.-M., *Appl. Phys. Lett.* **2010**, *96*, 153104.

[39] Song, X.-M.; Wu, J.-M.; Meng, L.; Yan, M., *J. Am. Ceram. Soc.* **2010**, *93*, 2068.

[40] Guan, X.-F.; Huang, S.-Q.; Zhang, Q.-X.; Shen, X.; Sun, H.-C.; Li, D.-M.; Luo, Y.-H.; Yu, R.-C.; Meng, Q.-B., *Nanotechnology* **2011**, *22*, 465402.

[41] Lai, Y.; Lin, Z.; Zheng, D.; Chi, L.; Du, R.; Lin, C., *Electrochim. Acta* **2012**, *79*, 175.

[42] Ma, X.; Shen, Y.; Wu, Q.; Shen, T.; Cao, M.; Gu, F.; Wang, L., *J. Inorg. Organomet. Polym. Mater.* **2013**, *23*, 798.

[43] Dong, C.; Li, X.; Qi, J., *J. Phys. Chem. C* **2011**, *115*, 20307.

[44] Labat, F.; Baranek, P.; Domain, C.; Minot, C.; Adamo, C., *J. Chem. Phys.* **2007**, *126*, 154703.

[45] Landmann, M.; Rauls, E.; Schmidt, W. G., *J. Phys. Condens. Matter* **2012**, *24*, 195503.

[46] Rajeshwar, K.; de Tacconi, N. R.; Chenthamarakshan, C. R., *Chem. Mater.* **2001**, *13*, 2765.

[47] Horn, M.; Schwerdtfeger, C. F.; Meagher, E. P., *Z. Kristallograph.* **1972**, *136*, 273.

[48] Ferrari, A. M.; Szieberth, D.; Noel, Y., *J. Mater. Chem.* **2011**, *21*, 4568.

[49] Calzado, C. J.; Hernández, N. C.; Sanz, J. F., *Phys. Rev. B* **2008**, *77*, 045118.

[50] Deskins, N. A.; Dupuis, M., *J. Phys. Chem. C* **2009**, *113*, 346.

[51] Deskins, N. A.; Rousseau, R.; Dupuis, M., *J. Phys. Chem. C* **2011**, *115*, 7562.

[52] Asahi, R.; Morikawa, T.; Ohwaki, T.; Aoki, K.; Taga, Y., *Science* **2001**, *293*, 269.

[53] Zhao, L.; Yu, J., *J. Colloid Interface Sci.* **2006**, *304*, 84.

[54] Nunzi, F.; De Angelis, F., *J. Phys. Chem. C* **2010**, *115*, 2179.

[55] Li, H.; Zhu, B.; Feng, Y.; Wang, S.; Zhang, S.; Huang, W., *J. Solid State Chem.* **2007**, *180*, 2136.

[56] Le Bahers, T.; Labat, F.; PauportÃl', T.; LainÃl', P. P.; Ciofini, I., *J. Am. Chem. Soc.* **2011**, pages null–null.

[57] Guijarro, N.; Shen, Q.; Giménez, S.; Mora-Seró, I.; Bisquert, J.; Lana-Villarreal, T.; Toyoda, T.; Gómez, R., *J. Phys. Chem. C* **2010**, *114*, 22352.

[58] Duncan, W. R.; Prezhdo, O. V., *J. Phys. Chem. B* **2004**, *109*, 365.

[59] Giorgi, G.; Fujisawa, J.-i.; Segawa, H.; Yamashita, K., *Phys. Chem. Chem. Phys.* **2013**, *15*, 9761.

[60] Sánchez-de Armas, R.; Oviedo López, J.; A. San-Miguel, M.; Sanz, J. F.; Ordejón, P.; Pruneda, M., *J. Chem. Theory Comput.* **2010**, *6*, 2856.

[61] Sánchez-de Armas, R.; San-Miguel, M. A.; Oviedo, J.; Marquez, A.; Sanz, J. F., *Phys. Chem. Chem. Phys.* **2011**, *13*, 1506.

[62] Chen, H.; Ratner, M. A.; Schatz, G. C., *J. Phys. Chem. C* **2011**, *115*, 18810.

5

FeS_2

Iron pyrite, FeS_2, is a very interesting semiconductor for applications in PV solar cells due to its beneficial optical properties. However, a low open circuit voltage, supposedly occurring due to S defects, which prevent iron pyrite from being a successfully applied PV material, thereby taking advantage of its abundance, non-toxicity, and optoelectronic properties. From a theoretical point of view, a proper description of the band gap is crucial. However, GGA functionals underestimate the band gap of FeS_2 drastically, leaving us with an actual metallic system. Hybrid GGA functionals, on the other hand, severely overestimate E_g. There remains the DFT+U methodology, which successfully circumvents such drawbacks at affordable computational costs. With this method and the assumption that Fe is high-spin, the Fe surface atoms of FeS_2 pyrite surfaces are described as magnetic and the band gap and the lattice constant are reproduced very close to experimental results.

5.1 Introduction

The large interest in iron pyrite, FeS_2, is based upon its properties that would render this material as a perfect photovoltaic material. The band gap is 0.95 eV, located in the red part of the light spectrum; it absorbs light very well ($\alpha > 10^5$ cm^{-1} for $h\nu > 1.4$ eV). Very important is also the long carrier diffusion length (100 – 1000 nm) which would enhance the collection of these carriers for electricity production. Finally, the almost infinite abundance of iron pyrite is another important advantage, which distinguishes FeS_2 from other PV material [1–4]. Furthermore, the raw materials extraction costs are extremely low; Wadia *et al.* estimated it to as less as $1.9 \cdot 10^{-6}$ ¢/W [4]. The raw materials extraction costs for CdSe are $1.2 \cdot 10^{-2}$ ¢/W, for CdTe $9.7 \cdot 10^{-2}$ ¢/W, and for ZnO they are $2.8 \cdot 10^{-1}$ ¢/W, to give a few examples. Colloidal synthesis of pyrite nanocrystals for solution deposition under ambient conditions further allow to maintain production costs of FeS_2 PV at a very low level.

The main drawback of FeS_2 used in solar cells is its low open-circuit potential, V_{oc}, which leads to low efficiency of thin film pyrite solar cells, despite the fact that the photocurrents are indeed relatively large (30 – 42 mA cm^{-2}) [5–8]. Moreover, even though numerous works was dedicated to remedy this flaw, no consensus was achieved so far. Sulfur vacancies, or near-surface nonstoichiometry, could cause a drop in V_{oc} [9–11]. In addition, surface Fermi pinning is thought to alter the efficiency of a PV cell, which can be caused by midgap defect states [9, 12–14], as do metallic FeS surface layers [15, 16]. Finally, occurrence of small domains of different phases like marcasite, pyrrhotite, and amorphous iron sulfide [9, 17] deteriorates the optoelectronic properties of iron pyrite.

Pyrite has a cubic structure where Fe^{2+} cations occupy the octahedral sites and sulfur S_2^{2-} anions occupy the tetrahedral sites. The crystal structure resemble to rock salt which has the space group $pa\bar{3}$. The Fe^{2+} cations form a face-centered cubic (*fcc*) sublattice. The Fe cations have six electrons outside the closed shells. The crystal field induced by S_2^{2-} leads to filled t_{2g} and empty e_g^* orbitals. The system is low-spin as the t_{2g} orbitals are completely filled by the six *d*-electrons. The electronic structure of FeS_2 pyrite has been subject of intensive research, both experimentally [18–22] and theoretically [15, 23–27].

Only in few studies, the samples are prepared from naturally grown pyrite

crystals. One example of such mechanical preparation methods that do not include synthesis is Reference [28]. They prepared thin film samples of iron pyrite by cutting the crystals perpendicular to the prominent (100) face with a diamond saw. Then, the slices are ground with special silicon-carbide grinding paper to a thickness of about 100 μm [28]. More common preparation methods of FeS_2 thin films are sulfurization of iron thin films [29–33], flash evaporation [34, 35], sputtering [36–39], electrodeposition [40], molecular beam epitaxy [41], spray pyrolysis [42], and chemical vapor deposition (CVD) [43–55].

Besides these thin film preparation procedures, there are studies that synthesize FeS_2 nanostructures [56–60]. Li *et al.* synthesized cubic FeS_2 nanocubes with differently set reaction times [59]. After 20 min reaction time, the nanocubes reached 150 nm edge lengths, after 180 min the edges were 250 nm long. Other work prepared nanocubes between 60 and 300 nm [56–58, 60]. In contrast, the nanodendrites that Li *et al.* synthesized have sizes of around 40 nm and it seems that they consist of smaller particles of around 10 nm sizes. In this size regime, the authors did not find any quantum size effects, which goes along with the relatively small excitonic Bohr radius of FeS_2 only $\sim$ 1.3 nm [61]. Li *et al.* tested the nanodendrites for their suitability in photovoltaic applications. They found that the prepared thin films absorb in the visible and near-infrared, which is an interesting range for PV light-harvesting [59]. The authors did not consider nanocubes as the thin film material due to its roughness of over 100 nm. The thin films prepared with the nanodendrites on the other hand are much smoother with height differences of roughly 30 nm over micrometer distances.

Nevertheless, Macpherson and Stoldt reported a synthesis procedure where small iron pyrite nanocubes form, the averaged length corresponds to $\sim$ 37 nm [62]. These nanocubes would allow for the making of FeS_2 thin films with smooth surfaces that are necessary to get the highest possible efficiencies. Apart from the size of the nanocrystals, it is also important to consider the optimal surface termination. Macpherson and Stoldt believe that surface reconstruction is an irreversible process; therefore, low temperatures and long reaction times are needed to eventually obtain perfectly shaped nanocubes with optimally surface termination. A different study synthesized FeS_2 nanocubes via a colloidal synthesis route, using 1-hexadecanesulfonate as ligand [60]. TEM images that were made during the synthesis show very small crystals after 2 minutes of re-

action time, which eventually aggregate and form nanocubes of 100 nm lengths. Aggregation took place rapidly, however, it should in principle be possible to adjust the reaction conditions as such that the yield for FeS_2 nanocrystals in the size regime of a few nanometers can be maximized. We should mention here a very extensive review written by Gao *et al.* where they discuss several synthesis methods to obtain metal chalcogenide nanomaterials that could be applied in energy conversion and storage, as well as in Li-ion batteries and supercapacitors [63].

The most stable surface under S lean conditions is the (001)-S surface [64], which has one layer of S atoms exposed to the vacuum, which are one-fold undercoordinated. The synthesis of nanocubes that expose this surface is feasible [62], therefore, we choose them as a model system for FeS_2 nanocluster in our calculations. The approach is to take bulk FeS_2 and cut a cube as such that the S^{1-} species is left at the surface, effectively breaking the S−S bonds of the S_2 dimers at the tetrahedral positions.

Surface states in FeS_2 are found to occur due to symmetry reduction of the metal atom coordination sphere, which can be explained by using a simple ligand field model to explain the surface states [13]. According to the authors of that study, the intrinsic Fe d_z^2 and d_{xy} states are the reason for the low open-circuit voltages. However, Sun *et al.* performed GGA and GGA+U calculations and did not find any surface states within the band gap [65]. Zhang *et al.* did reproduce their results applying a low-spin state to the (001) surface, thereby pointing out some deficiencies of the Bronold model [13], like missing out structural relaxation, and charge transfer that occurs at the surface.

Bulk iron pyrite FeS_2 is indeed in a low-spin state, and the same is generally thought of the (001) surface [64], at least if the surface does not show any imperfections. For his calculations, Alfonso did apply spin-polarization, but he did not probe for high-spin states. In contrast, Zhang *et al.* applied the DFT+U methodology and probed for a possible high-spin state. They found that the surface Fe atoms are magnetic with a moment of $2.0\,\mu_B$ per surface Fe atom [66]. The energy gain is 1.87 eV/cell, as compared to the low-spin state.

When surface defects do occur, for example by the formation of substoichiometric FeS_{2-x} sites, the splitting between t_{2g} and e_g^* becomes smaller, since the t_{2g} levels shift into the forbidden energy region and electrons can promote to

the e_g^* level [6, 9]. Furthermore, Alonso-Vante *et al.* observed that FeS_2 is paramagnetic with a magnetic susceptibility of $\chi = +0.175 \cdot 10^{-6}$ emu $\cdot$ g^{-1}, however, iron pyrite is expected to be diamagnetic [9].

The origin of the low V_{oc} is a controversial subject. Possible candidates are, for instance, sulfur vacancies and phase impurities. These would lead to phases like FeS, $Fe_{1-x}S_x$, and marcasite FeS_2. Wadia *et al.* reported that such impurities could have a negative impact on the V_{oc} due to their small band gaps [67]. Yet Steinhagen *et al.* found that this is not necessarily a sufficient reason for low V_{oc} because they did not find any indication about such phase impurities in their XRD and Raman spectra of their FeS_2 nanocrystal samples [68].

Another reason was suggested to be sulfur vacancies that pin the Fermi level of pyrite FeS_2 [10, 11, 55, 67]. This would also lead to a reduction of V_{oc}. However, Ellmer and Höpfner determined iron pyrite as a line compound [69], and bulk sulfur vacancies are thought to be unlikely [17]. Sun *et al.* reported that actually native defects have high formation energies [70], and that they hardly form. They further conclude that the native defect equilibrium concentrations are too low as that pure pyrite FeS_2 could be off-stoichiometric. Steinhagen *et al.* associated the sulfur deficiencies, which they measured via inductively coupled plasma atomic emission spectroscopy (ICP-AES), with the nanocrystal surfaces [68]. They linked the high electrical conductivity of the samples to the surface S deficiencies, because the FeS_2 surface decomposed into S deficient phases with high vacancy and carrier concentration [17]. Finally, the drop of the Fermi level towards to VB might be a consequence of O impurities that are incorporated during fabrication of pyrite thin films [70]. These impurities lead to an unintentional *p*-type conductivity.

O impurities may have undesired implications on the pyrite FeS_2 systems, however, Hu *et al.* performed a theoretical study where they alloyed FeS_2 with oxygen [71]. They were able to demonstrate that $FeS_{2-x}O_x$ films have stable band gaps larger than 1.2 eV, while it still maintains the favorable electrical and optical properties of pure pyrite FeS_2. Then again, a study about sulfur-doped hematite α-Fe_2O_3 showed that an increasing S concentration leads to a decrease of the band gap [72]. These authors reported that α-$Fe_2O_{3-x}S_x$ with $x \approx 0.17$ has a direct band gap of about 1.45 eV and a high optical absorption of $\sim 10^5 \text{cm}^{-1}$. It seems that doping of FeS_2 with O or α-Fe_2O_3 with S would

lead to very promising PV absorber materials, however, it is yet to be seen if experimental studies can reproduce these theoretical results, and if thin films of O doped FeS_2 or S doped hematite are not really affected by the problems inherited to the undoped systems.

There is yet another approach to explain and enhance the occurrence of low V_{oc}. Yu *et al.* established a design principle that deviates from the traditional point of view that S deficiencies are the main reason for the low V_{oc}. Their selection criterion is that a selected system must avoid spontaneous phase-separation into S deficient conducting materials with small band gaps [17]. Furthermore, these systems must assure a sufficiently large band gap. To fulfill this criterion, the Fe^{2+} ions must bind to at least six S atoms. This will provide a ligand-field splitting that is large enough for effective solar radiation absorption. The octahedral site on the Fe^{2+} ions can be stabilized with an electronegative element, which favors strong covalent Fe−S bonds. Based upon these rules, the authors examined Fe_2MS_4 materials, where M could be either Si or Ge. Especially Si would be a very interesting choice since it is much like Fe a very abundant element. Also doping with O seems a valid choice [71].

5.2 FeS_2 bulk and surfaces

We mentioned earlier that the PBE functional underestimates the band gap of semiconducting systems. In some cases this might be a quantitative problem only, because the band gap of, for example, anatase TiO_2 is large enough and,

TABLE 5.1 Shown are the lattice constant a_0, the band gap E_g, as well as the first absorption peak maximum E_{abs}, all calculated for bulk FeS_2 and different theoretical methodologies.

	a_0, [Å]	E_g, [eV]	E_{abs}, [eV]
PBE	5.342	0.27	0.87
PBE[a]	–	0.50	–
PBE+U	5.403	0.97	0.77, 0.99
PBE+U[a]	5.422	1.02	–
HSE06[a,b]	–	2.66	–
Exp.[c]	5.417	0.73–1.2	–

[a] Reference [66].
[b] Reference [73].
[c] References [28, 74–79].

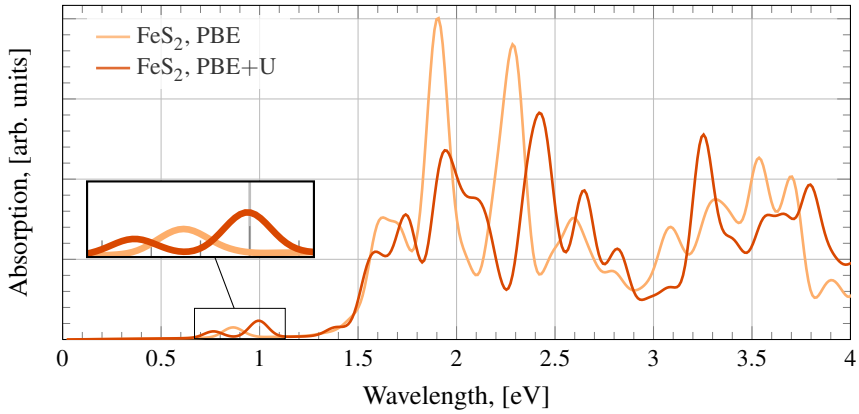

FIG. 5.1 Optical absorption spectra of bulk FeS_2, once calculated with the PBE functional, and with the PBE+U methodology.

therefore, the PBE band gap still represents a semiconducting system, which is qualitatively correct. Yet for systems with band gaps lower than 1 eV, the underestimation becomes also a quantitative problem. The probability is high that the band gap calculated with the PBE functional is reduced too much and the system turns from being semiconducting to metallic. FeS_2 is such a candidate. Experimentally, iron pyrite's band gap is generally found to be 0.95 eV, yet the results show a range between 0.73 and 1.2 eV [28, 74–81]. The risk of pyrite being characterized as a metallic system by PBE exists. Recent attempts to determine the band gap computationally using the PBE functional found that it results indeed very small (0.5 eV) [66, 73]. The results from our calculations are tabulated in Table 5.1. We calculated the PBE band gap to be even smaller than the one reported by Zhang *et al.*: $E_g = 0.27$ eV. Also the lattice constant is underestimated but the relative difference is not as large, the deviation being 2 %. The same authors calculated E_g with the HSE06 hybrid functional, but the resulting band gap was severely overestimated by more than 1.6 eV [66].

A methodology that can successfully tackle the problematic description of the electronic properties of pyrite at relatively low computational costs is the DFT+U methodology. It provides a viable alternative to the standard GGA and hybrid GGA functionals. For instance, Zhang *et al.* applied spin-polarized DFT+U calculations to a neutral (001)-FeS_2 surface, and correctly determined that the Fe surface atoms have a magnetic moment with DFT+U of 2.0 μ_B per

surface Fe atom. For the bulk pyrite they reported a band gap of 1.02 eV and a lattice constant of 5.422 Å [66].

Since not even hybrid functionals like the HSE06 functional reproduce well the electronic properties of FeS_2, we applied the DFT+U methodology together with the PBE functional. Zhang *et al.* derived an effective parameter U, U_{eff}, of 2 eV. Since they used the plane wave code VASP, we cannot apply this value directly, because we use the mixed Gaussian and plane wave code CP2K. Consequently, we have to determine the optimal U_{eff} specifically for this code, and we determine it to be 3.4 eV, which reproduces the band gap E_{g} and the lattice constant a_0 very close to the experimental values, see Table 5.1.

The optical absorption spectrum calculated with PBE illustrated in Fig. 5.1 reproduces surprisingly well the experimental spectra; the first absorption peak maximum is found at a wavelength of 0.87 eV. The FP-LAPW spectrum calculated by Vadkhiya and Ahuja, where they also apply the PBE GGA functional, shows absorption that starts already at 0.60 eV [82].

The PBE+U spectrum does show two absorption maxima, which are centered at 0.88 eV. The first maximum is located at 0.77 eV, the second, more intense peak has an energy of 0.99 eV. This goes along with the experimental spectrum reported by Ferrer *et al.*, for instance, for which absorption starts at 0.70 eV [83]. Unlike the spectrum obtained with the PBE functional, a small shoulder forms at 1.39 eV in the PBE+U spectrum. In this energy region between 0.5 and 1.5 eV, the latter spectrum is more feature rich; however, these features are less intense. Then, at energies higher than 1.5 eV, the intensity of both spectra increases and several features appear, as can be seen partially in Fig. 5.1. This intensity increase occurs for both spectra at the same energy. Comparing to literature, we find that the two spectra are actually similarly reproduced as those reported in earlier work [62, 82, 83].

Now we present the optical spectra for the (001)-S surface. As Hung *et al.* and Alfonso reported, the (001)-S surface is the most stable surface under S-lean conditions [64, 84]. Also, Zhang *et al.* used this surface for some of their calculations, which they label “Surf(0)” [66]. Here, we stick with the (001)-S label. The S atoms that are exposed to the vacuum are one-fold undercoordinated. They form S−S bonds, but they miss one bond to an adjacent Fe atom. The exposed Fe atoms themselves lack one bond, too, therefore the octahedron

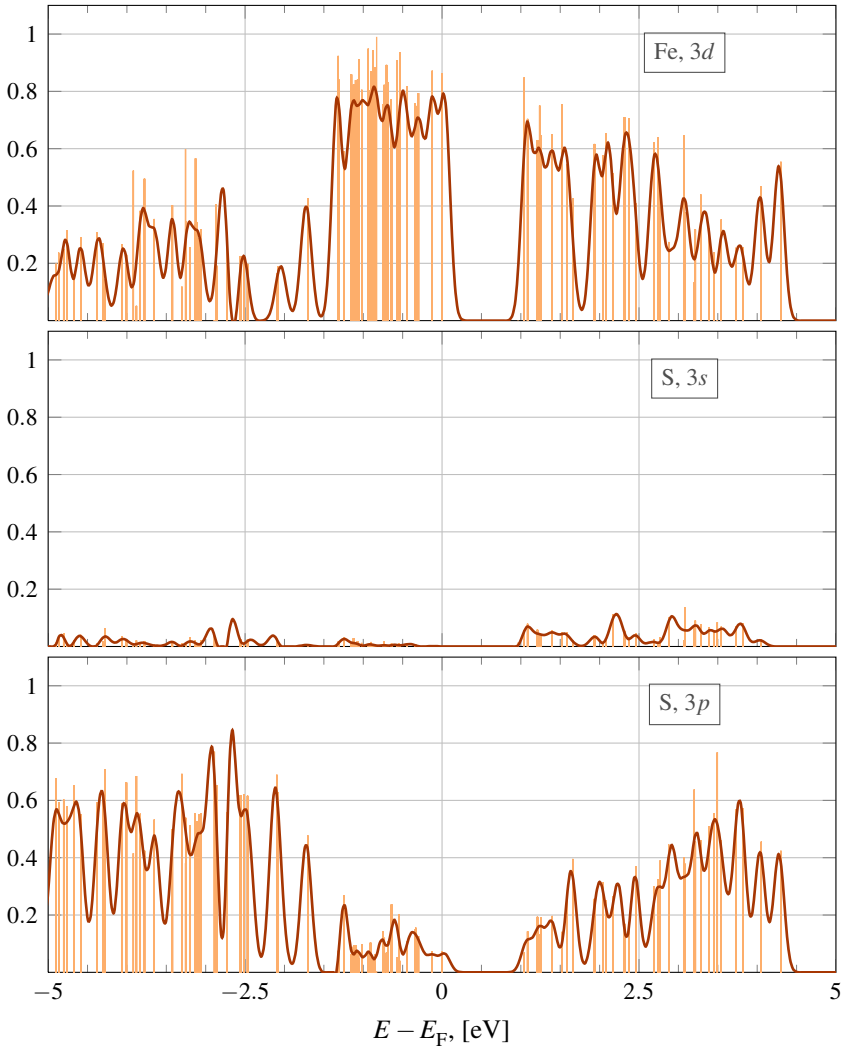

FIG. 5.2 Partial DOS of FeS_2 bulk calculated with the PBE+U methodology.

becomes a quadratic pyramid. The surface is electrically neutral.

In Fig. 5.3 the spectra of the (001)-S slab surface for PBE and PBE+U are illustrated. Unlike the bulk spectra, the surface spectra do differ noticeably. First and foremost, they differ mostly at the lowest absorption wavelengths. The PBE spectrum reveals weak optical activity at wavelengths as low as 0.21 eV, while the PBE+U spectrum does not. The first, weak absorption peak for PBE+U

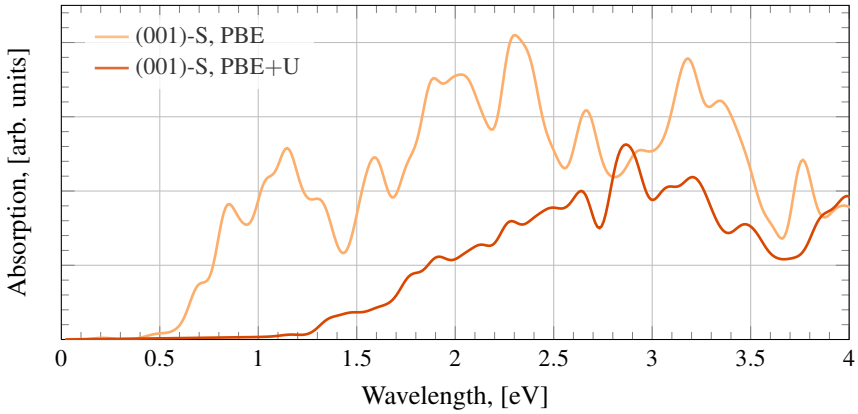

FIG. 5.3 Absorption spectra for the (001)-S surface of FeS_2, again calculated with both PBE and PBE+U.

occurs at 1.16 eV. After these first absorption peaks, the most intense features are found at 0.5 and 0.71 eV for PBE, and at 1.37 and 1.47 eV for PBE+U. These results demonstrate opposite behavior upon exposure of the (001)-S face to the vacuum relative to the bulk spectra: the PBE spectrum shifts to the red by roughly 0.3 eV, while it shifts to the blue by about 0.4 eV when the U_{eff} parameter has been applied. Additionally, the intensity of the PBE+U spectrum is weaker as it is for the PBE spectrum. Overall, the spectrum of the (001)-S surface is better reproduced with PBE+U than with PBE, and this is the reason that we will use PBE+U for the calculation of the FeS_2 clusters that have the (001)-S exposed. The band gap for the PBE+U surface is 0.98 eV, only slightly higher than the bulk band gap. Zhang *et al.* found a surface band gap of 0.72 eV [66]. However, in contrast to their work, the surface in this work is in a low-spin state.

5.3 FeS_2 clusters

After the bulk and surface slab systems, we present in this section the results for the iron pyrite clusters. Three different cluster sizes are employed. The smallest iron pyrite nanoparticle is the $(FeS_2)_{13}$ cluster, then a medium sized cluster that is modeled by 37 FeS_2 units, and, finally, the $(FeS_2)_{67}$ cluster. The optimized geometries are represented in Fig. 5.4. In that figure all geometries are obtained

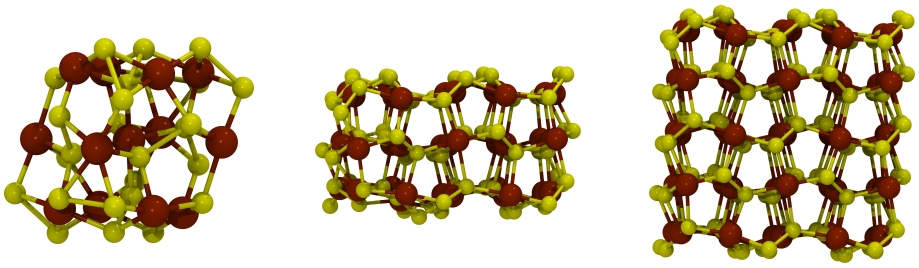

(a) (b) (c)

FIG. 5.4 Optimized low-spin geometries of the $(FeS_2)_{13}$, $(FeS_2)_{37}$, and $(FeS_2)_{62}$ clusters. For each cluster the side view is shown to visualize that the (001)-S surface is exposed to the vacuum.

with the clusters being in the low-spin state. The size of the $(FeS_2)_{13}$ cluster allows for exactly one Fe atom in the center that maintains the octahedral structure, which is typical for iron pyrite systems. The $(FeS_2)_{37}$ and $(FeS_2)_{62}$ models clearly show the iron pyrite structure within their cores, also on the surface only mild reconstruction takes place. $(FeS_2)_{13}$ has edges that are about 7.6 Å long; the edge lengths of $(FeS_2)_{37}$, which is not cubic, are $13\times13\times8.2$ Å. The $(FeS_2)_{62}$ cluster is again cubic and has 13 Å long edges.

All clusters are stoichiometric. However, since these clusters are cut out of a pyrite bulk, they inevitably suffer from surface defects. Considering first the surface planes of these clusters, we state that they are identical to a (001)-S terminated surface plane as we discussed it above. The borders of the clusters contain S atoms that are two-fold, and Fe atoms that are four-fold undercoordinated. Four vertices consist of S dimers, while two vertices are single S atoms, the only ones that have the S−S bond broken. These features are the same for all three clusters that we employ in this section.

The structure of $(FeS_2)_{13}$ in Fig. 5.4 was obtained assuming that the cluster is in a low-spin state. A different view of it is shown in Fig. 5.5(a). There it can be seen that the cluster contains in total 6 pairs of Fe atoms that have equivalent electronic environments. Reddish highlighted atoms only have four bonds formed to S atoms, while the bluish highlighted atoms have five, although the angle between the bonds is not always 90°, a consequence of the distortions already induced in low-spin cluster.

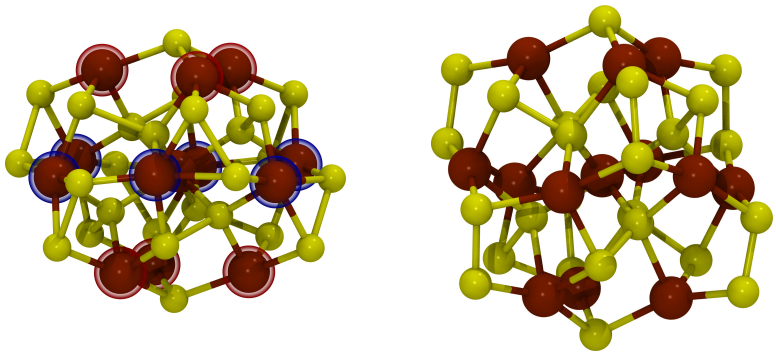

(a) $(FeS_2)_{13}$, low-spin (b) $(FeS_2)_{13}$, high-spin

FIG. 5.5 Represented in (a) is the cluster in Fig. 5.4(a), which has been rotated by about 60° clockwise in order to obtain the representation illustrated here. The Fe atoms in red and blue spheres, respectively, indicate atoms that have a similar bonding environment. For comparison reasons, in (b) is the same cluster illustrated, but optimized with a multiplicity of 5.

Following Zhang *et al.* [66] it is certain that the clusters as we employ them here are in a high-spin state, i.e. each Fe atom has four unpaired *d*-electrons. Indeed, the energy difference between the low- and the high-spin cluster is found to be 1.95 eV per FeS_2 unit when the smallest cluster is considered, favoring the high-spin state. For the largest 62 FeS_2-unit cluster the energy difference is 1.87 eV, again the high-spin state is the more stable one. In the high-spin state, the α-spin electrons occupy all the t_{2g} and e_g *d*-orbitals, whereas only one β-spin electron per Fe atom pairs with an electron of opposite spin. This results in a multiplicity of 5 per Fe atom. Therefore, the larger two clusters represented in Fig. 5.4 are already optimized assuming that they are in a high-spin state.

Only the smallest cluster undergoes some distortions if the models are calculated in a high-spin state. The low-spin and the high-spin version of $(FeS_2)_{13}$ are illustrated in Fig. 5.5. As can be seen in Fig. 5.5(b), the surface S atoms are puckered out more compared to the low-spin cluster Fig. 5.5(a). Although it is difficult to see, the almost perfect octahedron around the central Fe atom is lost. What is perfectly observed is that the high-spin cluster expands its volume consistently. The other two clusters, however, do not suffer from such changes, as they are large enough to maintain the iron pyrite structure that is observed in the sub-surface part of the cluster.

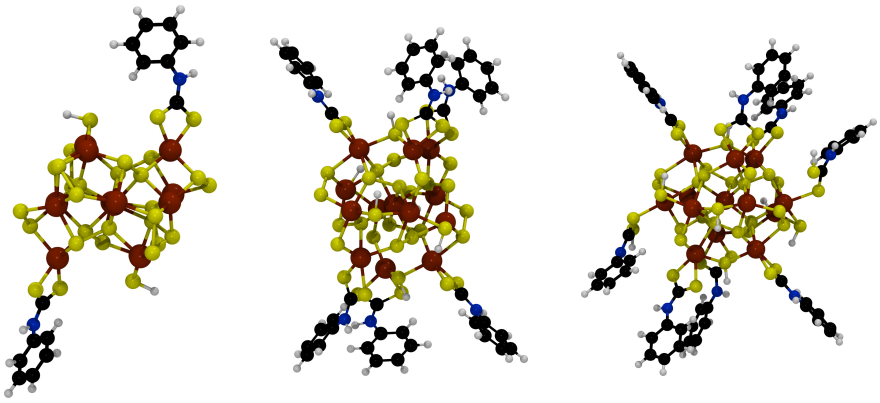

(a) (b) (c)

FIG. 5.6 Optimized geometries of the $(FeS_2)_{13}$ with 2, 6 and 8 PTC ligands adsorbed. Each model is represented in (a), (b), and (c), respectively. The orientation of the cluster corresponds roughly to one in Fig. 5.5, where the bluish highlighted atoms are in the middle plane.

In order to investigate if the electronic and optical properties of FeS_2 clusters are sensitive to the adsorption of ligand molecules, we added a different number of phenyldithiocarbamate (PTC) ligands to the $(FeS_2)_{13}$ cluster. The resulting cluster-ligand models are represented in Fig. 5.6. The first QD-ligand model in Fig. 5.6(a) contains only 2 PTC ligands, which are added to two four-coordinated Fe atoms, one in each plane of the reddish highlighted atoms in Fig. 5.5(a). The next model system, which is illustrated in Fig. 5.6(b), contains six PTC ligands in total, all of which are adsorbed onto all 4-coordinated Fe atoms. In both models, all these ligands are adsorbed in a dissociative manner, i.e. the H atoms are adsorbed on the FeS_2 cluster. Finally, the third $(FeS_2)_{13}$-ligand system shown in Fig. 5.6(c) has additional 2 PTC molecules adsorbed, which are put on two 5-coordinated Fe atoms in the hexagonal plane around the central Fe atom. The additional ligands are added in a coordinated fashion, that means that H atoms are still bound to S on the ligand. Also the medium and largest sized clusters are partially saturated with PTC, for these models all the Fe atoms that are only 4-coordinated are ligated. Therefore, 20 PTC molecules are added to $(FeS_2)_{37}$, and 24 to the $(FeS_2)_{62}$ cluster. Their structures are represented in Fig. 5.7.

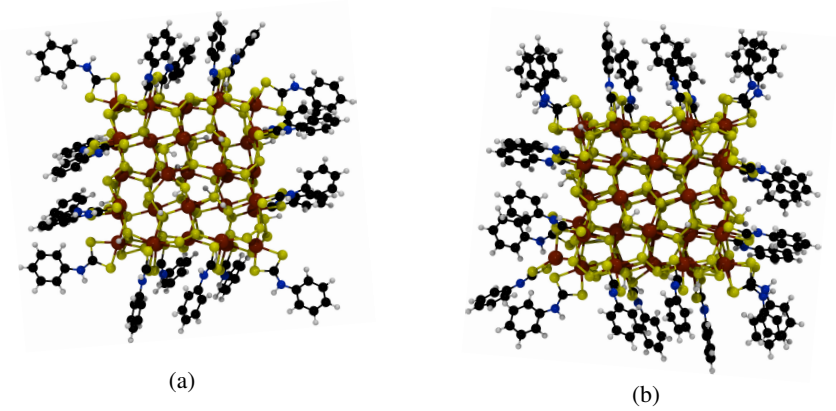

(a) (b)

FIG. 5.7 Optimized geometries of the $(FeS_2)_{37}(PTC)_{20}$ and $(FeS_2)_{62}(PTC)_{24}$ clusters are represented in (a) and (b), respectively.

Before we compare the PDOS of the different cluster models, we show what the ligands contribute to the MOs, which is illustrated in Fig. 5.8. For Fe only the $3d$, for the S atoms the $3p$ orbitals, and for C the $2p$ orbitals are included in the figure, other atomic orbitals do not have any important contribution in the energy range we employ here. It can be seen that α-VB edge is dominated by the $3p$ orbitals of S that is contained in the cluster. The $3d$ orbitals of Fe contribute only little to the VB edge. S_{PTC} and C hardly contribute to the highest lying MOs at all. The CB is then dominated by S and C. Especially the C atoms show some significant contributions to these states. For the β-spin channel the situation changes. Fe and S equally form the VB edge, while the CB is dominated by the

TABLE 5.2 E_g for both α- and β-spins of the different $(FeS_2)_{13}$-PTC systems, as well as for the two $(FeS_2)_{37}$ and $(FeS_2)_{62}$ clusters. The band gap of the low-spin $(FeS_2)_{13}$ cluster is 0.17 eV

	E_g^{α}, [eV]	E_g^{β}, [eV]
$(FeS_2)_{13}$	0.20	0.66
$(FeS_2)_{13}(PTC)_2$	0.25	0.37
$(FeS_2)_{13}(PTC)_6$	0.18	0.87
$(FeS_2)_{13}(PTC)_8$	0.21	0.82
$(FeS_2)_{37}$	0.10	0.02
$(FeS_2)_{37}(PTC)_{20}$	0.10	0.33
$(FeS_2)_{62}$	0.01	0.27
$(FeS_2)_{62}(PTC)_{24}$	0.03	0.41

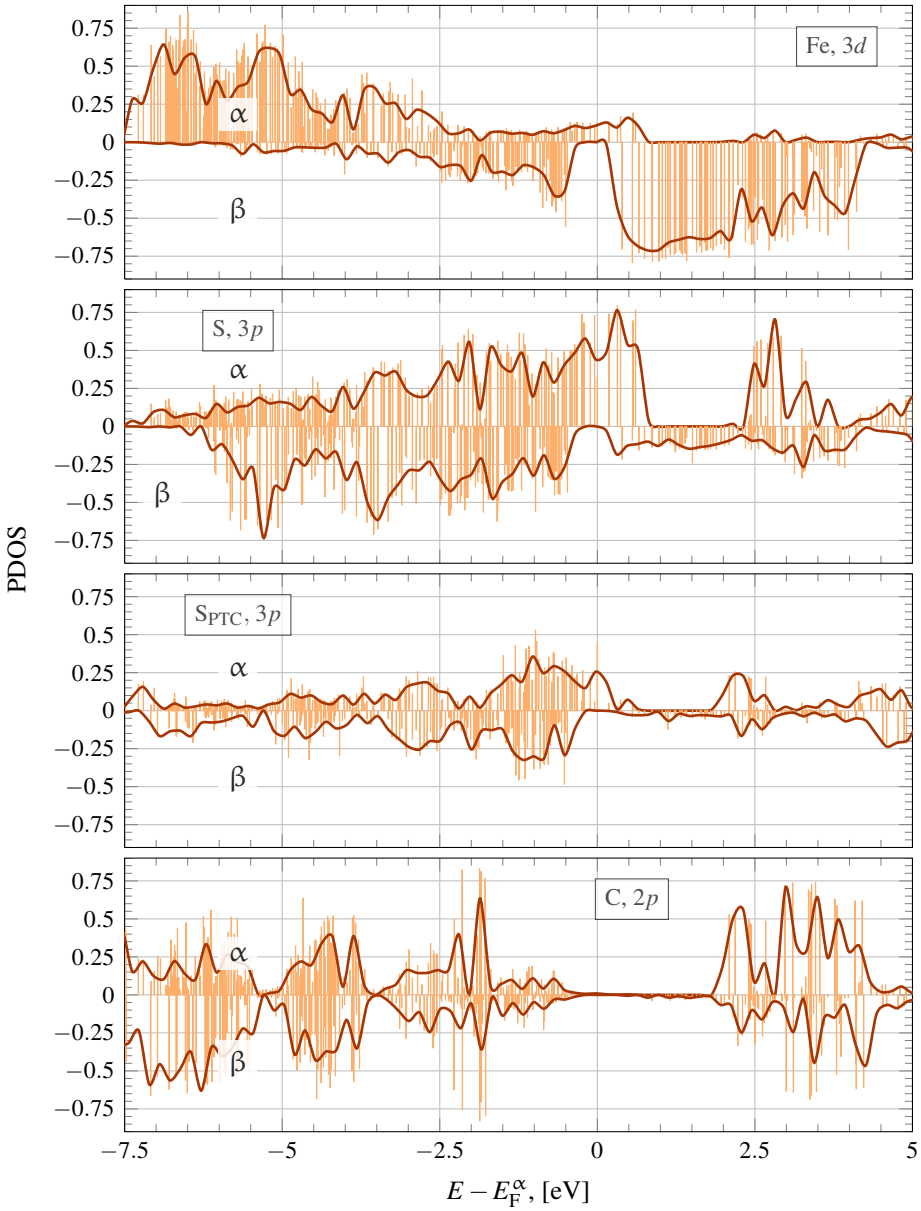

FIG. 5.8 PDOS for the $(FeS_2)_{13}(PTC)_6$ cluster model.

Fe 3*d* orbitals. The ligands do not contribute much anymore. The other models have similar distributions of the atomic orbitals, therefore, we do not include them here.

For the α-spin orbitals, the C 2*p*-orbitals again do not contribute almost anything to the VB. At E_g^α the S 2*p*-orbitals localized on the ligand molecules do show a significant contribution, although the S atoms in the FeS_2 cluster do contribute much more. These cluster S 2*p*-orbitals add most to the MOs that form right above the α-Fermi level. We discussed already the large gaps that occur above the MOs that still could be attributed to the VB. The α-CB edge is formed almost uniquely of S and C 2*p*-orbitals localized on the ligands. Here, C 2*p*-orbitals contribute most to these MOs, which are found at 2.1 eV. Then, at energies above 2.4 eV, the CB consists still mainly of C 2*p*-orbitals and of orbitals that are localized on the cluster's S atoms.

For each of the naked FeS_2 models, in Fig. 5.9 the PDOS of the Fe *d*-orbitals are represented, for both α- and β-spin. The band gaps for these systems are also listed in Table 5.2. There one can see that the α-band gap, E_g^α, decreases with the increasing size of the clusters. However, for $(FeS_2)_{62}$ it is nearly zero. Above the LUMO opens another gap between it and the LUMO+1. These gaps are usually much larger. They occur for each system, in the case of the $(FeS_2)_{13}$ cluster it results to be 1.74 eV, for $(FeS_2)_{37}$ 1.62 eV, and for the $(FeS_2)_{62}$ cluster 1.54 eV. All cluster models show the same sequence. If this α-band gap is considered, similarly to the CdSe QDs, then we find that the diameter of the cluster correlates with the gap between the LUMO and the LUMO+1: the smaller the cluster's diameter the larger is the gap above the LUMO. Apart from this, we note that the appearance of the α-spin channel for all clusters is very similar.

Compared to the α-HOMOs, the β-HOMOs are lying at lower energies, the differences between the HOMOs being 0.30 eV for the $(FeS_2)_{13}$ cluster, while for $(FeS_2)_{37}$ and $(FeS_2)_{62}$ the β-HOMOs lie 0.40 and 0.37 eV below the α-HOMO. In each panel in Fig. 5.9, these β-HOMOs are indicated with a black dotted line. In this figure one also observes that although E_g^β for $(FeS_2)_{37}$ is nearly zero, similar to the α-spin channel, a large gap exists right above the LUMO, it being 1.09 eV. This system shows in general a clean PDOS, in the sense that both LUMOs lye energetically close to the HOMOs and that above the LUMO a larger gap exists.

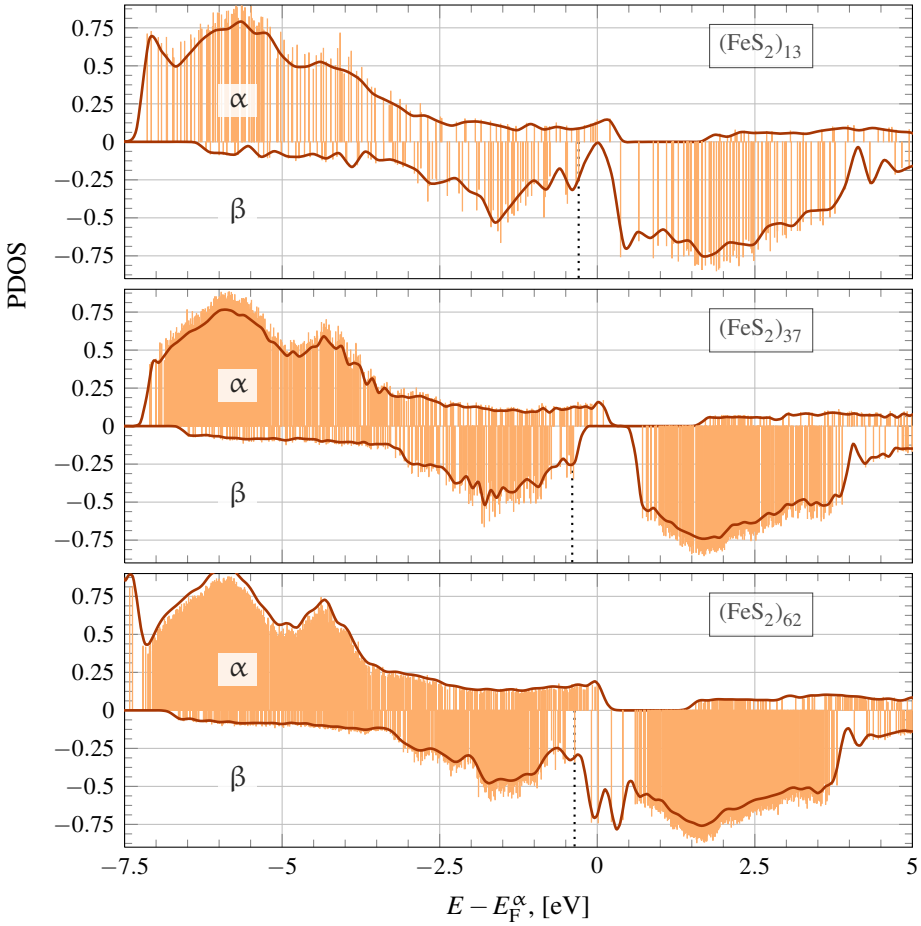

FIG. 5.9 PDOS of the Fe *d*-orbitals, both α- and β-spin, for the bare FeS_2 clusters $(FeS_2)_{13}$, $(FeS_2)_{37}$, and $(FeS_2)_{62}$. All models are high-spin. The black dotted lines indicate the E_g^β.

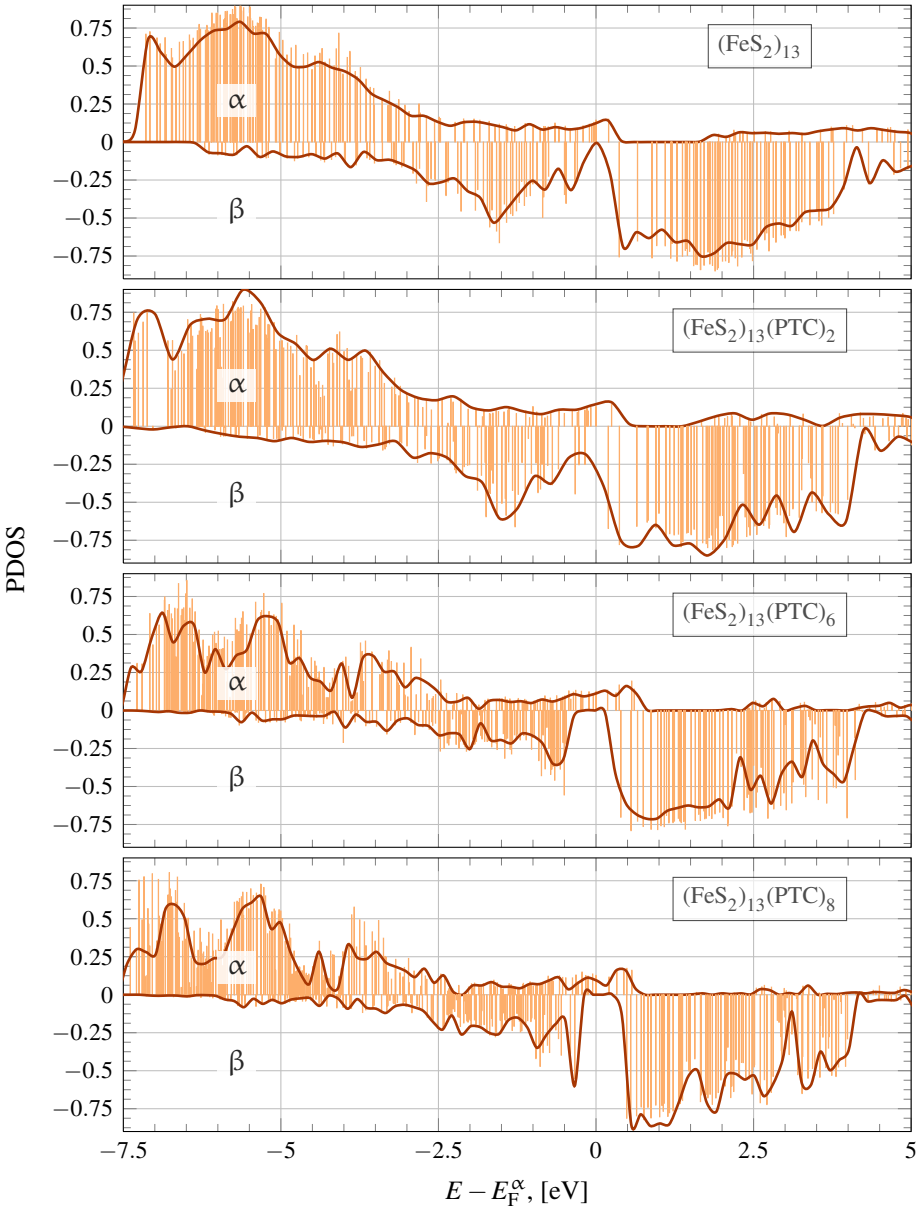

FIG. 5.10 PDOS of the $(FeS_2)_{13}$ cluster with different numbers of PTC ligands adsorbed. The corresponding systems are indicated within each panel.

This is not necessarily the case for the $(FeS_2)_{13}$ and $(FeS_2)_{62}$ clusters. As it is tabulated in Table 5.2, the $(FeS_2)_{13}$ cluster has a E_g^{β} of 0.66 eV, but the $(FeS_2)_{62}$ cluster has a gap of only 0.25 eV. In both β-PDOSs states appear which do not exist within the range between $-0.2 - +0.4$ eV in the β-spin channel of the $(FeS_2)_{37}$ model.

If we compare the PDOS graphs in Fig. 5.9 with the results published by Zhang *et al.* [66] we note some similarities between our and their neutral (001)-S surface DOS. For the Fe atoms that are contained in the first slab layer, they identified a surface state (SS2 in that article) right below the Fermi level. Although we do not obtain such states below the Fermi level, we think that the LUMOs might be related to the surface state Zhang *et al.* reported about. They further found a different surface state (SS1) at 1 eV above the Fermi level, which is similar to those states that are equivalent to the α-LUMO+1. Since some quantum confinement is expected also for FeS_2 clusters [61], the cluster's band gaps should be larger than the bulk ones. Therefore, these states are located at roughly 1.5 eV for $(FeS_2)_{13}$.

As can be seen in Table 5.2, upon saturation of the $(FeS_2)_{13}$ pyrite cluster with PTC ligands, the α-band gap remains in the range between 0.18 and 0.25 eV. The α-PDOS of $(FeS_2)_{13}$ and $(FeS_2)_{13}(PTC)_2$ resemble each other in that the α-LUMO is roughly at the same position and also the band structure between −7.5 and 0 eV is similar. Above these LUMOs, in both cases a gap opens up, as just discussed, although the inclusion of the two ligand molecules leads to a decrease of 0.31 eV down to 1.43 eV for $(FeS_2)_{13}(PTC)_2$. Apart from this small deviation, the α-PDOSes at energies higher than 1.5 eV are also similar.

Then, as all the 4-coordinated Fe atoms are saturated with PTC the α-PDOS changes noticeably. First of all, instead of the single band that represents the α-LUMO in the upper two panels in Fig. 5.10, now several states occur for $(FeS_2)_{13}(PTC)_6$ and $(FeS_2)_{13}(PTC)_8$ at energies up to 0.75 eV. For the latter model, more such states show up. Above these bands, similar to the bare and the $(FeS_2)_{13}(PTC)_2$ clusters, larger gaps of 1.49 ($(FeS_2)_{13}(PTC)_6$) and 1.03 eV ($(FeS_2)_{13}(PTC)_8$) occur, compared to 1.74 and 1.43 eV for the bare and two-fold ligated clusters, respectively.

Finally, at an energy of 2.5 eV, some smaller differences occur between the upper and the lower two α-PDOS represented in Fig. 5.10. The $(FeS_2)_{13}$ and

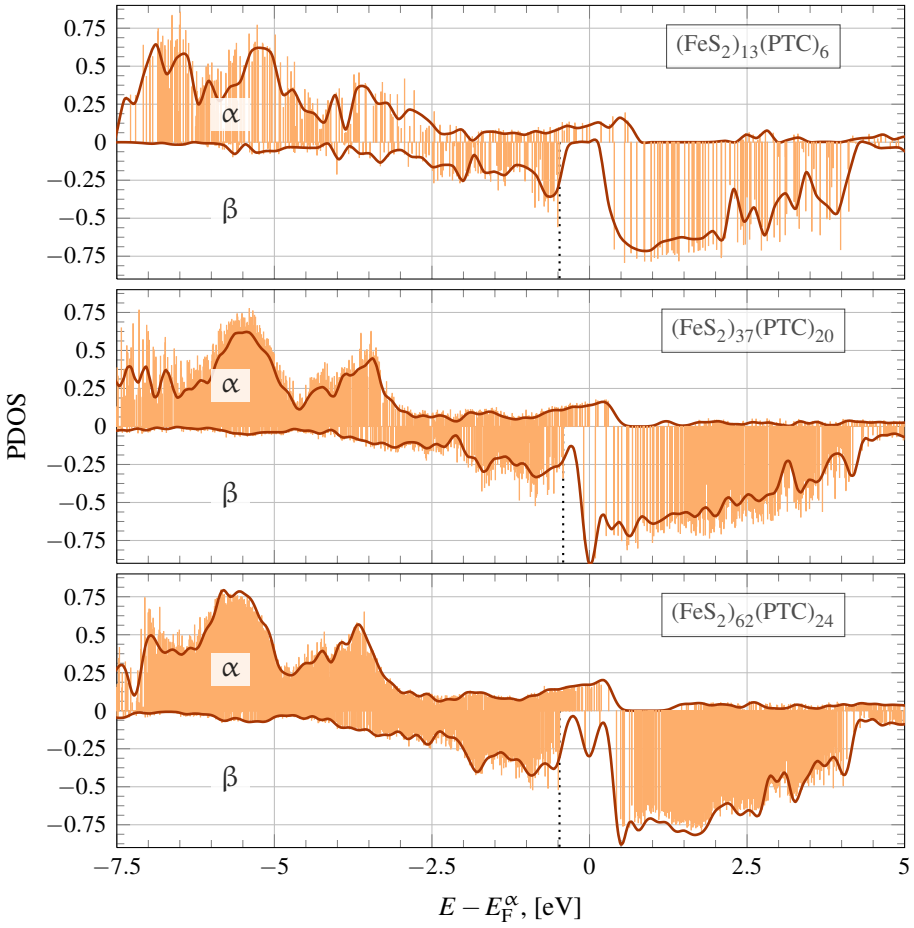

FIG. 5.11 PDOS for the 3 cluster models where all 4-coordinated Fe atoms are saturated with PTC. No 5-coordinated Fe atoms have been ligated here.

$(FeS_2)_{13}(PTC)_2$ models have here states with low intensity starting at an energy of 1.75 eV. Where the cluster's 4-coordinated Fe atoms are passivated, the number of those states decreases. The saturation of all of the 4-coordinated Fe atoms leads to more obvious changes in the electronic structure of FeS_2 cluster as if only 2 of these Fe atoms are saturated. Also, the additional passivation of 5-coordinated Fe atoms does not have an important influence if the 4-coordinated Fe are passivated already.

From Table 5.2, the β-band gap decreases first by about 0.3 eV when two PTC molecules are added, and increases by roughly 0.2 eV when 6 or 8 PTC ligands are added (with respect to the bare cluster), which is also observed in Fig. 5.10. The VBs show differences between the bare and $(FeS_2)_{13}(PTC)_2$ cluster on the one hand and $(FeS_2)_{13}(PTC)_6$ and $(FeS_2)_{13}(PTC)_8$ on the other hand. While in the PDOS of the former this band shows the most intense bands at around −1.5 eV, in the latter the most intense bands are observed close to the β-VB edge. The VB edge is most compact for $(FeS_2)_{13}(PTC)_6$, whereas the other systems show that the MOs are energetically more separated. The CBs are then relatively similar for all systems, except for $(FeS_2)_{13}(PTC)_2$, which has several states that occur between −0.5 and 0.5 eV, where the other cluster models have no MOs in the β-spin channel.

Fig. 5.11 shows the PDOS of the three differently sized FeS_2 clusters that all have the 4-coordinated Fe atoms saturated. These are the $(FeS_2)_{13}(PTC)_6$, $(FeS_2)_{37}(PTC)_{20}$, and $(FeS_2)_{62}(PTC)_{24}$ models. For the α-spin channel, the changes between the bare and saturated clusters are the same as just discussed. While the bare clusters have one band that is equivalent the α-LUMO, the presence of the PTC ligands introduce more bands right above the α-LUMO. E_g^α remains the same regardless if the cluster is passivated or not. Contrarily to this behavior, the β-band gap increases, as can be seen in Table 5.2. Fig. 5.11 further reveals that the states that occur in the β-PDOS of the bare clusters do not disappear as it occurs in the $(FeS_2)_{13}$ cluster. All in all the three PDOS in Fig. 5.11 resemble each other much, especially the 37 and the 62 unit clusters.

In the last part of this section, we present the absorption spectra of a few of the FeS_2 clusters presented above. First, we introduce a spectrum of the low-spin $(FeS_2)_{13}$ cluster that is calculated with the LR-TDDFT method as it is implemented in the GAUSSIAN09 program suite [85]. With it, we get some insight in the nature of the excitations, which otherwise would be unknown. The spectrum is represented in Fig. 5.12. The B3LYP hybrid functional was used, together with the LANL2TZ+ basis set for the Fe, and the LANL2DZdp basis set for S. 400 singlet excitation were included in the calculation. The composition of the most prominent excitations are tabulated in Table 5.3.

The first state with considerable intensity is found at 0.23 eV. It is formed by several excitations that include the highest 5 HOMOs, except the HOMO-

TABLE 5.3 Excitation energies, oscillator strengths, and composition of the excitation of a few excitations that are observed in Fig. 5.12.

E_{exec}, [eV]	f	Excited state composition	
0.23	0.0026	HOMO-5 → LUMO:	-0.21697
		HOMO-3 → LUMO:	0.35431
		HOMO-2 → LUMO:	-0.30711
		HOMO-1 → LUMO:	-0.26284
		HOMO → LUMO:	0.31777
0.31	0.0021	HOMO-29 → LUMO+1:	-0.12215
		HOMO-25 → LUMO+1:	-0.10459
		HOMO-24 → LUMO+1:	-0.12170
		HOMO-18 → LUMO+1:	0.11210
		HOMO-17 → LUMO+1:	0.15286
		HOMO-15 → LUMO+1:	-0.12648
		HOMO-13 → LUMO+1:	-0.12409
		HOMO-10 → LUMO+1:	0.18561
		HOMO-7 → LUMO+1:	-0.12567
		HOMO-5 → LUMO:	0.16267
		HOMO-2 → LUMO:	0.25573
		HOMO-1 → LUMO+1:	-0.19841
0.35	0.0074	HOMO-6 → LUMO:	0.25384
		HOMO-5 → LUMO:	-0.17461
		HOMO-4 → LUMO:	0.17546
		HOMO-3 → LUMO:	0.10186
		HOMO-2 → LUMO:	-0.10974
		HOMO-1 → LUMO:	0.55585
		HOMO → LUMO:	-0.11926
0.41	0.0045	HOMO-8 → LUMO:	-0.22240
		HOMO-5 → LUMO:	0.18704
		HOMO-4 → LUMO:	0.55454
		HOMO-2 → LUMO:	0.15269
0.86	0.0138	HOMO-10 → LUMO:	0.34421
		HOMO-8 → LUMO:	0.43618
		HOMO-7 → LUMO:	-0.20443
		HOMO-4 → LUMO:	0.18758
0.92	0.0126	HOMO-10 → LUMO:	0.58385
		HOMO-8 → LUMO:	-0.29033
		HOMO-4 → LUMO:	-0.15067

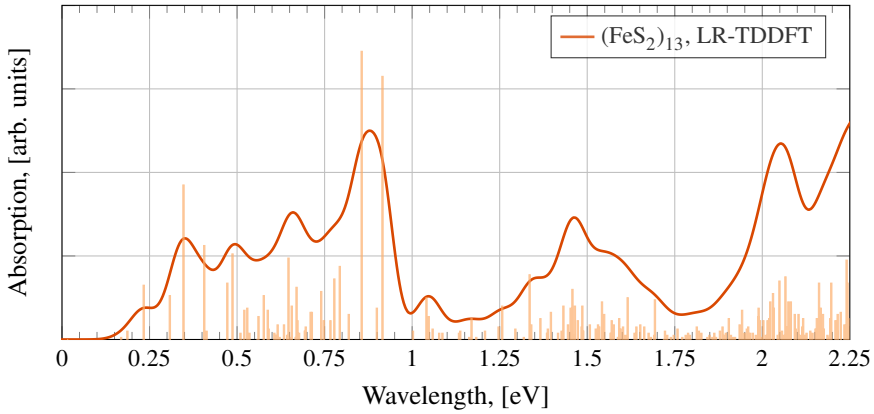

FIG. 5.12 Spectrum of the low-spin $(FeS_2)_{13}$ cluster calculated with the LR-TDDFT method. The half-width at half-height is set to 0.04 eV.

4. All excitations have the LUMO as target MO. The second excitation at 0.31 eV contains transitions mainly into the LUMO+1, only two transitions occur between the HOMO-5 and the HOMO-2 into the LUMO. Some HOMOs are localized quite deep in the VB, the lowest HOMO that contributes to this excitation is identified as the HOMO-29. Right next to this peak is an absorption feature at 0.35 eV, where all the transitions end in the LUMO, starting from the seven highest HOMOs. Again, here is a negative transition found going from the LUMO to the HOMO-1. The excitation itself is the most intense one within the first 0.9 eV. The next absorption peak at 0.41 eV is less intense than the previous one, but still more intense than the first two peaks. It consists only of 4 transitions, however, the HOMOs are relatively far away from the VB edge. Finally, the table lists the two most intense absorption features at 0.86 and 0.92 eV. Both contain transitions from the HOMO-10, HOMO-8, and HOMO-4 into the LUMO. The lower peak at 0.86 eV contains further a transition from the HOMO-7 into the LUMO.

Now, we introduce the spectra of the low- and the high-spin version of the spin-polarized $(FeS_2)_{13}$ cluster system as it is obained with the RT-TDDFT methodology. They are shown in Fig. 5.14. The spectrum of the spin-polarized, low-spin system reproduces well the experimental UV-Vis absorption spectrum of FeS_2 QDs that was just recently published by Gong *et al.* [86] if only the en-

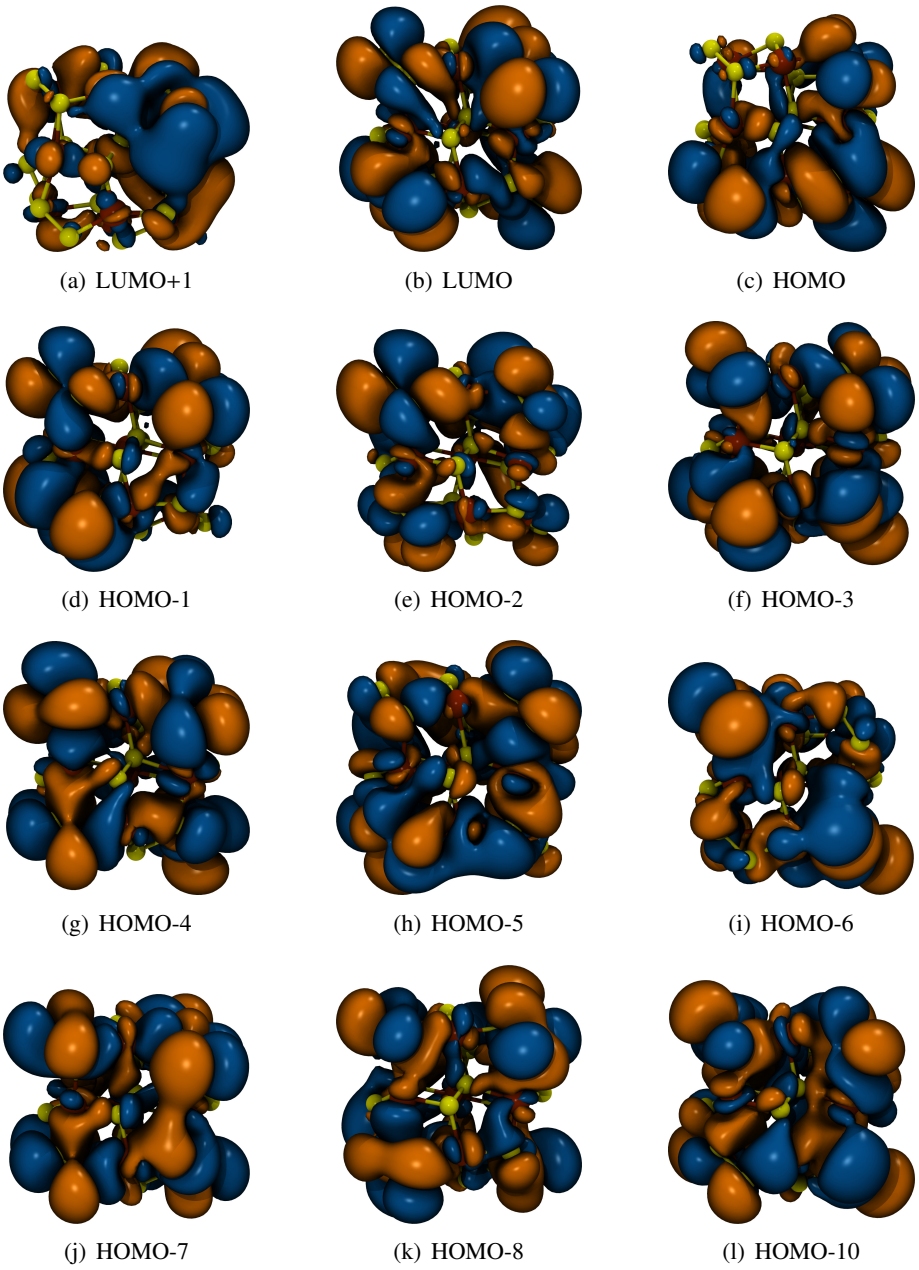

(a) LUMO+1 (b) LUMO (c) HOMO

(d) HOMO-1 (e) HOMO-2 (f) HOMO-3

(g) HOMO-4 (h) HOMO-5 (i) HOMO-6

(j) HOMO-7 (k) HOMO-8 (l) HOMO-10

FIG. 5.13 Molecular orbitals that are included in the excitations tabulated in Table 5.3.

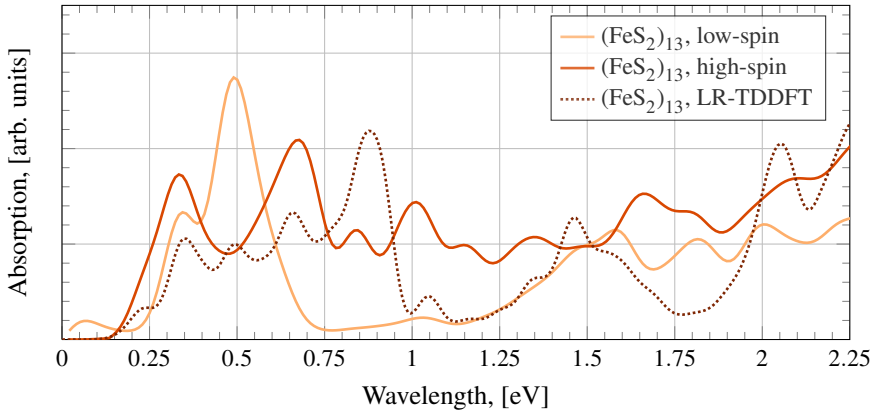

FIG. 5.14 Optical absorption spectra of $(FeS_2)_{13}$ both in low-spin and high-spin state.

ergy range is considered that was presented in this article (300–1600 nm). The low-intensity peak at 1.03 eV (1200 nm) in Fig. 5.14 shows up at 0.89 eV (1400 nm) in the work of Gong *et al.*, and the next most intense peak at 1.58 eV (785 nm) is found at roughly 1.77 eV (700 nm) in the experimental spectrum. This is a red-shift of 0.19 eV compared to literature. In the cited work, the smallest QDs have a size of 23 nm.

However, if we include also the longer wavelength part of the spectrum, absorption features are observed, too. The first absorption peak maximum is located at 0.34 eV for both low- and high-spin systems. This corresponds roughly to E_g and E_g^α, respectively. It is more intense for the high-spin cluster, while the low-spin cluster has the most intense absorption feature lying at 0.49 eV. The second peak of the high-spin system is found at 0.67 eV. Then, the low-spin cluster does not show optical activity up to 1.1 eV, which is somehow similar to what is observed in Fig. 5.12, where after the first most intense peak at 0.35 eV the intensities of the peaks are rather low. However, the two spectra do not have much in common. On the other hand, the high-spin system constantly shows optical absorption at half of the intensity of the peak at 0.67 eV. Above 1.5 eV, the two spectra are similar in the sense that the absorption intensity is continuously increasing.

We now compare all three differently sized high-spin cluster systems. Compared to the smallest cluster, $(FeS_2)_{37}$ has the spectrum that resembles it closest.

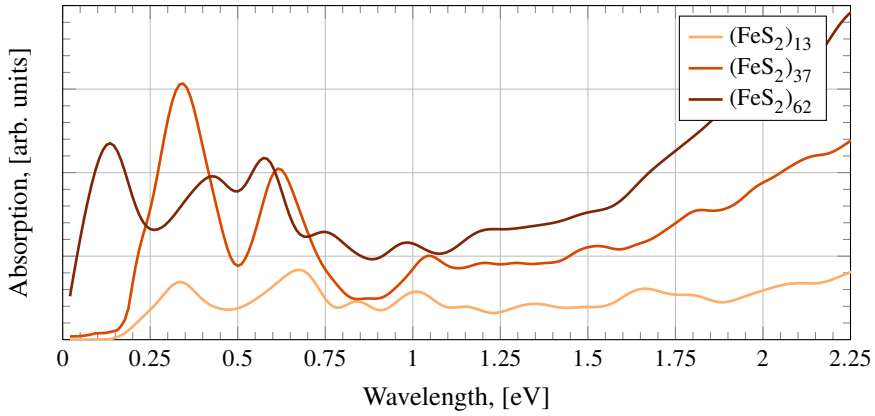

FIG. 5.15 Represented are the spectra of the three bare clusters $(FeS_2)_{13}$, $(FeS_2)_{37}$, and $(FeS_2)_{62}$.

Both have the first absorption peak maximum at 0.34 eV and a second peak right after at 0.62 eV. The first peak of the $(FeS_2)_{37}$ model system is much more intense than the one of the $(FeS_2)_{13}$ cluster. This is not correlated to the different sizes of the clusters, because the ratio between the maximal intensities is about 4.6:1 favoring the medium sized cluster, while the ratio of the number of FeS_2 units is 2.8:1. At energies higher than 1 eV, the ratio of the absorption intensities matches approximately the size ratio. Only the peak at 0.12 eV in the $(FeS_2)_{37}$ spectrum does not occur in the $(FeS_2)_{13}$ spectrum.

In all three spectra, a peak exists around 0.6 eV. For $(FeS_2)_{13}$ it is located at 0.68 eV, the equivalent peak of the $(FeS_2)_{37}$ spectrum is found at 0.62 eV, and the same peak of the $(FeS_2)_{62}$ cluster is observed at 0.58 eV. This indicates a certain size dependency of this peak, and we assume that the type of the transition is the same in all three clusters. Also that the intensity of the peaks is higher the larger the cluster is points support the assumption that it is the same transition in each case.

$(FeS_2)_{62}$ shows the same peak at 0.12 eV as $(FeS_2)_{37}$, which is not observed in the spectrum of the smallest cluster. The largest FeS_2 QD also has a second peak at 0.45 eV, which is not observed in the $(FeS_2)_{13}$ and $(FeS_2)_{37}$ spectra. The origin of the first peak is unclear. As mentioned before, the increased intensity above 1 eV reflects the higher number of FeS_2 units. Therefore, it seems as if

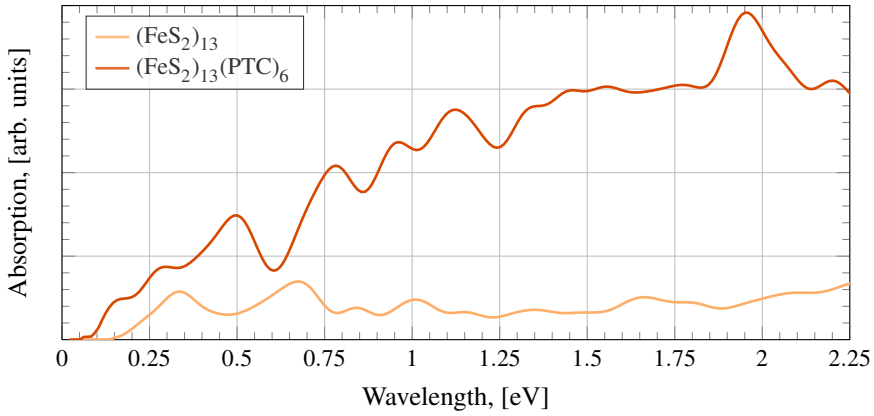

FIG. 5.16 Illustrated are the absorption spectra of the bare $(FeS_2)_{13}$ cluster and $(FeS_2)_{13}(PTC)_6$, as well as of the isolated PTC ligand.

these absorption features below 1 eV are by one way or another related to the FeS_2 cluster's surface.

The last optical spectrum we present is for the $(FeS_2)_{13}$ cluster saturated with 6 PTC ligands. Upon saturation the spectrum does red-shift even more as can be seen in Fig. 5.16, where the spectra of the $(FeS_2)_{13}$ and the $(FeS_2)_{13}(PTC)_6$ cluster are shown. The spectrum of the PTC ligand is also included. The effect of the red-shift is that the spectrum shifts from 0.34 eV (bare) down to 0.17 eV. This might be expected since dithiocarbamates are π-donors with good delocalizing properties. Consequently, the spectrum red-shifts, as it occurs already when DMATP and DMPDA passivated the $(CdSe)_{13}$ cluster (c.f. Fig. 3.16 on page 80). Also, the inclusion of the PTC ligands leads to an overall increase of the optical absorption intensity, most probably due to the just mentioned good delocalization of the photogenerated hole.

What is interesting, though, is that this spectrum reproduces some of the lower lying peaks that occur in the LR-TDDFT spectrum in Fig. 5.12. In particular the peaks at 0.3, 0.5, and 0.8 eV in Fig. 5.16 are very close to those tabulated in Table 5.3. Also the relative intensities between the peaks are similar.

5.4 Discussion

After the successful application of the RT-TDDFT methodology on CdSe and CdSe-TiO_2 systems, we employed a different, more complex system. FeS_2, or iron pyrite, is indeed a model system that was reported already to be difficult in the sense that its promising optical properties, especially when it is employed as a light absorbing material, are hampered by a low V_{oc}. Surface states, Fermi pinning, incorrect bonding environment around the Fe atoms were possible reasons that were held responsible for the bad performance in PV applications.

The low band gap of 0.95 eV makes it necessary to apply the DFT+U method in order to avoid that bulk pyrite will be described as a metal. With this methodology we obtain a band gap of 0.97 eV, and a lattice constant of 5.403 Å, which is very close to experimentally determined values. For the bulk, the optical spectra did not differ much between PBE and PBE+U results. Only when the S terminated (001)-S surface is exposed to the vacuum, the spectrum depends on the computational methodology. The PBE+U spectrum of this surface has optical activity only at 1.3 eV, while the first absorption peak maximum of the PBE spectrum is situated at 0.71 eV.

For the pyrite clusters, we find that they need to be described in a high-spin state, where each Fe has a multiplicity of 5. The energy difference between the low- and high-spin clusters is around 1.9 eV, depending on the cluster system. Furthermore, at least for the smallest FeS_2 cluster, the first absorption peak is not shifting noticeably, however, the spectra do differ in that the low-spin spectrum has no optical activity between 0.7 and 1.2 eV, whereas the high-spin cluster model absorbs in that energy range. At higher energies, the spectra are not very different. However, the higher stability found for the high-spin clusters is partially compromised if the spectrum of the low-spin cluster is compared to the experimental spectrum reported by Gong *et al.* [86]. Both spectra resemble each other, the differences are smaller than 0.2 eV, at least in the energy range that was reported by these authors. Longer wavelengths are not shown in their experimental UV-Vis spectrum, since these wavelengths are already out of the visible range. The LR-TDDFT spectrum calculated by applying the B3LYP hybrid functional, shows that especially the peaks between 0.2 and 0.5 eV consist of several transitions from orbitals that lie deep in the VB. Only the two peaks at 0.86 and 0.92 eV consist only of 4 and 3 transitions, respectively. But also

they excite an electron from the HOMO-10 into the LUMO. The highest lying HOMO is the HOMO-4.

E_g^α of the three cluster models $(FeS_2)_{13}$, $(FeS_2)_{37}$, and $(FeS_2)_{62}$, decreases with increasing size. Also the β-band gap decreases, however, it is almost zero for the $(FeS_2)_{37}$ cluster. Therefore, a strict relationship between this gap and the cluster size cannot be made. The α-PDOS of these systems reveals that each cluster has the LUMO relatively close to the HOMO. Besides that, they also have a wide gap larger than at least 1.1 eV right above the LUMO. Since the temperature of the geometry optimizations is at 0 K, it can be reasoned that at ambient temperatures or above, the small band gaps disappear, and that consequently the gap between the LUMO and the LUMO+1 is the actual α-band gap.

Passivation of the unsaturated Fe atoms has a positive effect mainly on the β-spin channel. When all the 4-coordinated Fe atoms are saturated with a PTC ligand, the E_g^β increases to over 0.8 eV. The same is observed when $(FeS_2)_{37}$ and $(FeS_2)_{62}$ are passivated with PTC, yet the increase is smaller. For $(FeS_2)_{37}$ it results to be 0.31 eV, and for the largest pyrite cluster it is 0.14 eV. For the α-spin channel the inclusion of the ligands leads to more states in the energy region around 0.5 eV, where the α-LUMOs of the bare clusters are typically found. It seems as if saturating ligands complicate the electronic structure of FeS_2, at least this is the case for PTC.

The influence of the PTC ligands on the absorption spectrum is similar to that of DMATP and DMPDA. Due to their good hole delocalization properties the electron excitation is facilitated and, as a consequence, the first absorption features are red-shifted by roughly 0.1 eV. Apart from that, the overall intensity of the spectrum increases drastically, also below the 4.2 eV, where PTC has its first absorption peak maximum. Obviously, this kind of ligand seems to be beneficial to the optical properties of QDs through its ability to delocalize the positive charge in the aromatic π-system. Charge separation is easier performed, and the probability of transferring the photoexcited electron to the semiconductor is higher.

So, is it a fool who put the stakes on the abundant, non-toxic, and cheap iron pyrite, or fool's gold? Steinhagen *et al.* [68] did very critically analyze this material and they concluded that the possibility to be a fool is quite high.

From our data that we just have presented, we cannot conclusively say whether iron pyrite can be applied successfully in PV applications or not. We can say, however, that this system from a theoretical point of view is very complex, and there is still a lot of work to do to better characterize it. It remains an interesting system, again from a theoretical point of view, and one has to consider that intensive investigation of FeS_2 is still going on. There is still a lot to understand about iron pyrite.

Furthermore, new approaches like the one proposed by Yu *et al.* [17] who reported about a tertiary compound that included Si or Ge next to FeS_2. Also doping with O is another approach [71] worth to develop further. Both approaches maintain the excellent optical properties of pyrite, without sabotaging the solar cell efficiency because of the low open circuit current. Additionally, the report by Gong *et al.* showed that the reaction condition can enhance the cristallinity of FeS_2 QDs as well [86]. Such results may lead early enough to promising synthesis routes that produce highly efficient PV cells based on iron pyrite.

5.5 Bibliography

[1] Ennaoui, A.; Tributsch, H., *Sol. Energ. Mater.* **1986**, *14*, 461.

[2] Smestad, G.; Ennaoui, A.; Fiechter, S.; Tributsch, H.; Hofmann, W.; Birkholz, M.; Kautek, W., *Sol. Energ. Mater.* **1990**, *20*, 149.

[3] Altermatt, P. P.; Kiesewetter, T.; Ellmer, K.; Tributsch, H., *Sol. Energy Mater. Sol. Cells* **2002**, *71*, 181.

[4] Wadia, C.; Alivisatos, A. P.; Kammen, D. M., *Environ. Sci. Technol.* **2009**, *43*, 2072.

[5] Ennaoui, A.; Tributsch, H., *Solar Cells* **1984**, *13*, 197.

[6] Antonucci, V.; Arico', A.; Giordano, N.; Antonucci, P.; Russo, U.; Cocke, D.; Crea, F., *Solar Cells* **1991**, *31*, 119.

[7] Ennaoui, A.; Fiechter, S.; Jaegermann, W.; Tributsch, H., *J. Electrochem. Soc.* **1986**, *133*, 97.

[8] Ennaoui, A.; Fiechter, S.; Tributsch, H.; Giersig, M.; Vogel, R.; Weller, H., *J. Electrochem. Soc.* **1992**, *139*, 2514.

[9] Alonso-Vante, N.; Chatzitheodorou, G.; Fiechter, S.; Mgoduka, N.; Poulios, I.;

Tributsch, H., *Sol. Energ. Mater.* **1988**, *18*, 9.

[10] Birkholz, M.; Fiechter, S.; Hartmann, A.; Tributsch, H., *Phys. Rev. B* **1991**, *43*, 11926.

[11] Ennaoui, A.; Fiechter, S.; Pettenkofer, C.; Alonso-Vante, N.; Büker, K.; Bronold, M.; Höpfner, C.; Tributsch, H., *Sol. Energy Mater. Sol. Cells* **1993**, *29*, 289.

[12] Buker, K.; Alonso-Vante, N.; Tributsch, H., *J. Appl. Phys.* **1992**, *72*, 5721.

[13] Bronold, M.; Tomm, Y.; Jaegermann, W., *Surface Science* **1994**, *314*, L931.

[14] Bronold, M.; Pettenkofer, C.; Jaegermann, W., *J. Appl. Phys.* **1994**, *76*, 5800.

[15] Rosso, K. M.; Becker, U.; Hochella, M. F., *Am. Mineral.* **1999**, *84*, 1535.

[16] Murphy, R.; Strongin, D. R., *Surf. Sci. Rep.* **2009**, *64*, 1.

[17] Yu, L.; Lany, S.; Kykyneshi, R.; Jieratum, V.; Ravichandran, R.; Pelatt, B.; Altschul, E.; Platt, H. A. S.; Wager, J. F.; Keszler, D. A.; Zunger, A., *Adv. Energy Mater.* **2011**, *1*, 748.

[18] Li, E.; Johnson, K.; Eastman, D.; Freeouf, J., *Phys. Rev. Lett.* **1974**, *32*, 470.

[19] Mosselmans, J.; Pattrick, R.; van der Laan, G.; Charnock, J.; Vaughan, D.; Henderson, C.; Garner, C., *Phys. Chem. Miner.* **1995**, *22*, 311.

[20] Fujimori, A.; Mamiya, K.; Mizokawa, T.; Miyadai, T.; Sekiguchi, T.; Takahashi, H.; Môri, N.; Suga, S., *Phys. Rev. B* **1996**, *54*, 16329.

[21] Nesbitt, H.; Berlich, A.; Harmer, S.; Uhlig, I.; Bancroft, G.; Szargan, R., *Am. Mineral.* **2004**, *89*, 382.

[22] Prince, K.; Matteucci, M.; Kuepper, K.; Chiuzbaian, S.; Bartkowski, S.; Neumann, M., *Phys. Rev. B* **2005**, *71*, 085102.

[23] Bither, T.; Bouchard, R.; Cloud, W.; Donohue, P.; Siemons, W., *Inorg. Chem.* **1968**, *7*, 2208.

[24] Folkerts, W.; Sawatzky, G.; Haas, C.; De Groot, R.; Hillebrecht, F., *J. Phys. C: Solid State Phys.* **1987**, *20*, 4135.

[25] Raybaud, P.; Hafner, J.; Kresse, G.; H, T., *J. Phys. Condens. Matter* **1997**, *9*, 11107.

[26] Eyert, V.; Höck, K. H.; Fiechter, S.; Tributsch, H., *Phys. Rev. B* **1998**, *57*, 6350.

[27] von Oertzen, G. U.; Skinner, W. M.; Nesbitt, H. W., *Phys. Rev. B* **2005**, *72*, 235427.

[28] Kou, W. W.; Seehra, M. S., *Phys. Rev. B* **1978**, *18*, 7062.

[29] Ferrer, I. J.; Sanchez, C., *J. Appl. Phys.* **1991**, *70*, 2641.

[30] de las Heras, C.; de Vidales, J. L. M.; Ferrer, I. J.; Sánchez, C., *J. Mater. Res.* **1996**, *11*, 211.

[31] Wan, D.; Wang, Y.; Wang, B.; Ma, C.; Sun, H.; Wei, L., *J. Cryst. Growth* **2003**, *253*, 230.

[32] Hamdadou, N.; Khelil, A.; Bernède, J., *Mater. Chem. Phys.* **2003**, *78*, 591.

[33] Pascual, A.; Diaz-Chao, P.; Ferrer, I.; S anchez, C.; Ares, J., *Sol. Energy Mater. Sol. Cells* **2005**, *87*, 575.

[34] de las Heras, C.; Ferrer, I. J.; Sánchez, C., *Appl. Surf. Sci.* **1991**, *50*, 505.

[35] de las Heras, C.; Ferrer, I. J.; Sánchez, C., *J. Phys. Condens. Matter* **1994**, *6*, 10177.

[36] Willeke, G.; Dasbach, R.; Sailer, B.; Bucher, E., *Thin Solid Films* **1992**, *213*, 271.

[37] Birkholz, M.; Lichtenberger, D.; Höpfner, C.; Fiechter, S., *Sol. Energy Mater. Sol. Cells* **1992**, *27*, 243.

[38] Lichtenberger, D.; Ellmer, K.; Schieck, R.; Fiechter, S.; Tributsch, H., *Thin Solid Films* **1994**, *246*, 6.

[39] Susac, D.; Zhu, L.; Teo, M.; Sode, A.; Wong, K. C.; Wong, P. C.; Parsons, R. R.; Bizzotto, D.; Mitchell, K. A. R.; Campbell, S. A., *J. Phys. Chem. C* **2007**, *111*, 18715.

[40] Nakamura, S.; Yamamoto, A., *Sol. Energy Mater. Sol. Cells* **2001**, *65*, 79.

[41] Bronold, M.; Kubala, S.; Pettenkofer, C.; Jaegermann, W., *Thin Solid Films* **1997**, *304*, 178.

[42] Yamamoto, A.; Nakamura, M.; Seki, A.; Li, E.; Hashimoto, A.; Nakamura, S., *Sol. Energy Mater. Sol. Cells* **2003**, *75*, 451.

[43] Chatzitheodorou, G.; Fiechter, S.; Könenkamp, R.; Kunst, M.; Jaegermann, W.; Tributsch, H., *Mater. Res. Bull.* **1986**, *21*, 1481.

[44] Schleich, D.; Chang, H., *J. Cryst. Growth* **1991**, *112*, 737.

[45] Ennaoui, A.; Schroetter, S.; Fiechter, S.; Tributsch, H., *J. Mater. Sci. Lett.* **1992**, *11*, 1131.

[46] Höpfner, C.; Ellmer, K.; Ennaoui, A.; Pettenkofer, C.; Fiechter, S.; Tributsch, H., *J. Cryst. Growth* **1995**, *151*, 325.

[47] Thomas, B.; Höpfner, C.; Ellmer, K.; Fiechter, S.; Tributsch, H., *J. Cryst. Growth* **1995**, *146*, 630.

[48] Thomas, B.; Ellmer, K.; Müller, M.; Höpfner, C.; Fiechter, S.; Tributsch, H., *J. Cryst. Growth* **1997**, *170*, 808.

[49] Thomas, B.; Cibik, T.; Höpfner, C.; Diesner, K.; Ehlers, G.; Fiechter, S.; Ellmer, K., *J. Mater. Sci. Mater. Electron.* **1998**, *9*, 61.

[50] Oertel, J.; Ellmer, K.; Bohne, W.; Röhrich, J.; Tributsch, H., *J. Cryst. Growth* **1999**, *198-199*, 1205.

[51] Reijnen, L.; Meester, B.; Goossens, A.; Schoonman, J., *J. Electrochem. Soc.* **2000**, *147*, 1803.

[52] Meester, B.; Reijnen, L.; Goossens, A.; Schoonman, J., *Chem. Vap. Deposition* **2000**, *6*, 121.

[53] Takahashi, N.; Sawada, T.; Nakamura, T.; Nakamura, T., *J. Mater. Chem.* **2000**, *10*, 2346.

[54] Takahashi, N.; Nakatani, Y.; Yatomi, T.; Nakamura, T., *Chem. Mater.* **2003**, *15*, 1763.

[55] Berry, N.; Cheng, M.; Perkins, C. L.; Limpinsel, M.; Hemminger, J. C.; Law, M., *Adv. Energy Mater.* **2012**, *2*, 1124.

[56] Wang, D.-W.; Wang, Q.-H.; Wang, T.-M., *CrystEngComm* **2010**, *12*, 755.

[57] Wang, D.; Wang, Q.; Wang, T., *CrystEngComm* **2010**, *12*, 3797.

[58] Bi, Y.; Yuan, Y.; Exstrom, C. L.; Darveau, S. A.; Huang, J., *Nano Lett.* **2011**, *11*, 4953.

[59] Li, W.; Doblinger, M.; Vaneski, A.; Rogach, A. L.; Jackel, F.; Feldmann, J., *J. Mater. Chem.* **2011**, *21*, 17946.

[60] Lucas, J. M.; Tuan, C.-C.; Lounis, S. D.; Britt, D. K.; Qiao, R.; Yang, W.; Lanzara, A.; Alivisatos, A. P., *Chem. Mater.* **2013**, *25*, 1615.

[61] Wilcoxon, J. P.; Newcomer, P. P.; Samara, G. A., *Solid State Commun.* **1996**, *98*, 581.

[62] Macpherson, H. A.; Stoldt, C. R., *ACS Nano* **2012**, *6*, 8940.

[63] Gao, M.-R.; Xu, Y.-F.; Jiang, J.; Yu, S.-H., *Chem. Soc. Rev.* **2013**, *42*, 2986.

[64] Alfonso, D. R., *J. Phys. Chem. C* **2010**, *114*, 8971.

[65] Sun, R.; Chan, M. K. Y.; Ceder, G., *Phys. Rev. B* **2011**, *83*, 235311.

[66] Zhang, Y. N.; Hu, J.; Law, M.; Wu, R. Q., *Phys. Rev. B* **2012**, *85*, 085314.

[67] Wadia, C.; Wu, Y.; Gul, S.; Volkman, S. K.; Guo, J.; Alivisatos, A. P., *Chem. Mater.* **2009**, *21*, 2568.

[68] Steinhagen, C.; Harvey, T. B.; Stolle, C. J.; Harris, J.; Korgel, B. A., *J. Phys. Chem. Lett.* **2012**, *3*, 2352.

[69] Ellmer, K.; Höpfner, C., *Philos. Mag. A* **1997**, *75*, 1129.

[70] Sun, R.; Chan, M. K. Y.; Kang, S.; Ceder, G., *Phys. Rev. B* **2011**, *84*, 035212.

[71] Hu, J.; Zhang, Y.; Law, M.; Wu, R., *J. Am. Chem. Soc.* **2012**, *134*, 13216.

[72] Xia, C.; Jia, Y.; Tao, M.; Zhang, Q., *Physics Letters A* **2013**, *377*, 1943.

[73] Hu, J.; Zhang, Y.; Law, M.; Wu, R., *Phys. Rev. B* **2012**, *85*, 085203.

[74] Schlegel, A.; Wachter, P., *J. Phys. C: Solid State Phys.* **1976**, *9*, 3363.

[75] Seehra, M. S.; Seehra, S. S., *Phys. Rev. B* **1979**, *19*, 6620.

[76] Abass, A. K.; Ahmed, Z. A.; Tahir, R. E., *J. Appl. Phys.* **1987**, *61*, 2339.

[77] Karguppikar, A. M.; Vedeshwar, A. G., *Phys. Status Solidi B* **1988**, *109*, 549.

[78] Tsay, M.-Y.; Huang, Y.-S.; Chen, Y.-F., *J. Appl. Phys.* **1993**, *74*, 2786.

[79] Yang, T.-R.; Yu, J.-T.; Huang, J.-K.; Chen, S.-H.; Tsay, M.-Y.; Huang, Y.-S., *J. Appl. Phys.* **1995**, *77*, 1710.

[80] Marinace, J. C., *Phys. Rev.* **1954**, *96*, 593.

[81] Horita, H., *J. Phys. Soc. Jpn.* **1972**, *33*, 1723.

[82] Vadkhiya, L.; Ahuja, B., *J. Alloys Compd.* **2011**, *509*, 3042.

[83] Ferrer, I.; Nevskaia, D.; de las Heras, C.; Sánchez, C., *Solid State Commun.* **1990**, *74*, 913.

[84] Hung, A.; Muscat, J.; Yarovsky, I.; Russo, S. P., *Surf. Sci.* **2002**, *513*, 511.

[85] M. J. Frisch; G. W. Trucks; H. B. Schlegel; G. E. Scuseria; M. A. Robb; J. R. Cheeseman; G. Scalmani; V. Barone; B. Mennucci; G. A. Petersson; H. Nakatsuji; M. Caricato; X. Li; H. P. Hratchian; A. F. Izmaylov; J. Bloino; G. Zheng; J. L. Sonnenberg; M. Hada; M. Ehara; K. Toyota; R. Fukuda; J. Hasegawa; M. Ishida; T. Nakajima; Y. Honda; O. Kitao; H. Nakai; T. Vreven; J. A. Montgomery; J. E. Peralta; F. Ogliaro; M. Bearpark; J. J. Heyd; E. Brothers; K. N. Kudin; V. N. Staroverov; R. Kobayashi; J. Normand; K. Raghavachari; A. Rendell; J. C. Burant; S. S. Iyengar; J. Tomasi; M. Cossi; N. Rega; J. M. Millam; M. Klene; J. E. Knox; J. B. Cross; V. Bakken; C. Adamo; J. Jaramillo; R. Gomperts; R. E. Stratmann; O. Yazyev; A. J. Austin; R. Cammi; C. Pomelli; J. W. Ochterski; R. L. Martin; K. Morokuma; V. G. Zakrzewski; G. A. Voth; P. Salvador; J. J. Dannenberg; S. Dapprich; A. D. Daniels; Ö. Farkas; J. B. Foresman; J. V. Ortiz; J. Cioslowski; D. J. Fox, *Gaussian 09 Revision A.1* **2009**, Gaussian Inc. Wallingford CT.

[86] Gong, M.; Kirkeminde, A.; Ren, S., *Sci. Rep.* **2013**, *3*, .

6

Discussion

In this work we give an ample overview of CdSe and FeS_2 quantum dots. CdSe, which is a widely employed semiconductor in QD synthesis, serves well to perform initial tests on it. From the four functionals we tested (PBE, PBE0, BLYP, and B3LYP), B3LYP in conjunction with the LANL2DZ basis set gives the best results when the optical properties of CdSe are of interest. However, the B3LYP functional is prohibitively expensive if it comes to calculate systems with several hundred of atoms or large box sizes. Since in each direction at least 14 Å need to be included in isolated systems, the total system size can become huge. In the end PBE offers the best compromise between costs and accuracy.

We find further that the basis sets and pseudopotentials, which are included in the CP2K program suite, have a good performance related both to structural as well as to optical properties. Geometries are usually very close to those that are obtained with large basis sets, while the optical absorption spectra are reproduced well.

For FeS_2 we find that the standard PBE functional, together with the standard basis sets and pseudopotentials in CP2K, does not perform well because of iron pyrite's small band gap, which almost disappears when this combination of functional and basis sets/pseudopotentials is employed. To avoid the usage of costly computational methods, we applied the DFT+U methodology. Our optimized U_{eff} reproduces the band gap and the lattice constant of FeS_2 very close

to experimental results. This reduction of computational costs is even more important since the pyrite cluster models need to be calculated in high-spin state with four unpaired electrons per Fe atom.

One of the biggest advantage of QDs is the dependence of the first absorption peak maximum on the diameter of the QD: the larger the diameter, the longer is the wavelength at which a cluster adsorbs light. We reproduce this behavior successfully for the CdSe QDs. For FeS_2, the dependence exists, too. $(FeS_2)_{13}$ and $(FeS_2)_{37}$ have E_{abs} at the same energy (0.34 eV), whereas the first absorption peak maximum of $(FeS_2)_{62}$ shifts to lower energies, as expected. For the FeS_2 clusters, the size dependence becomes most obvious when the gap between the LUMO and the LUMO+1 is considered. In that case, the gap in the α-channel decreases from 1.74 eV ($(FeS_2)_{13}$) to 1.54 eV for the $(FeS_2)_{62}$ cluster.

Also the impact of ligands that passivate unsaturated surface bonds is substantially. When added to CdSe clusters, simple ligands like methylamine, shift the spectrum to lower wavelengths. Other ligands like thiols or phosphine oxides change the spectrum the same way. The differences between the absorption peak maxima is only about 0.1 eV when methylamine and methylthiol ligands are compared, or if the short carbohydrate chain of trimethylphosphine oxide is exchanged for a longer butyl chain.

All these ligands are aliphatic. However, as soon as aromatic ligands are employed, the situation changes drastically. Within the aniline type ligands the difference between the lowest and highest lying first absorption peak maxima is 0.4 eV. The ligand that shifted the spectrum the most to the red is DMPDA, and it carries a dimethylamine group, which is bound at the *para*-position to the amine group. Dimethylamine is a good electron donor, and as such it has a high affinity to stabilize the photogenerated hole. This is the reason for the strong red-shift. Contrarily, if the substituent is a good electron acceptor, the spectrum is blue-shifted. We find that this is true in principle, but the extent of the blue-shift cannot be correlated with the ability as an electron-acceptor. In general, if the spectrum should be altered for a given cluster size, such aromatic ligands offer an alternative path to the size tuning of the spectrum.

The 4-coordinated Fe atoms of all the three FeS_2 clusters were also passivated with the PTC ligand, a dithiocarbamate type molecule. If 5-coordinated Fe atoms of $(FeS_2)_{13}$ are saturated with PTC, the PDOS does not change substan-

tially. The effect of the ligand absorption on the electronic structure is different for the two spin channels. The β-band gap, for instance increases compared to the bare clusters. For the α-channel more states occur at the energy where the LUMO of the bare cluster is located. These observations are true for all the FeS_2 clusters that are employed here.

$(FeS_2)_{13}(PTC)_6$ is the only FeS_2-PTC system for which the absorption spectrum is calculated. It also shows a red-shift of the first absorption peak maximum, similar to the effect that the saturation of CdSe clusters with DMATP or DMPDA has, though the shift was not as large as compared to the influence that the aromatic ligands have on the CdSe QDs.

Considering TiO_2 sensitized with CdSe QDs, we find that the VB edge is composed of atomic orbitals localized on CdSe, while the CB edge is formed of atomic orbitals from the TiO_2 part of the system. The band gaps of the these system is very small, sometimes it is even zero. The band gaps of the separated CdSe and TiO_2 parts, however, still exist. This is why the first absorption peak maximum is still the same when CdSe adsorbs on different TiO_2 structures.

The energy at which the lowest lying optical transition occurs, does not change when the cluster is adsorbed on TiO_2 via the MPA linker. If the dopamine linker is employed, the spectrum changes at energies below the first absorption peak maximum of the QD. This is related to the aromaticity of the molecule. Even though the spectrum does change, it must not mean that the electron transfer efficiency of the overall system is bad, because the aromatic system of DA could actually facilitate the transfer. However, we are not in the position to argue about such assumptions. Similarly, if the QD is adsorbed directly on the TiO_2 model, the intensity of the first absorption peak maximum decreases and low-intensity peaks occur at lower energies. These absorption features, however, are by no means as strong as if the QD is linked with DA.